



HAL
open science

Towards flexible and low-power wireless smart sensors : reconfigurable analog-to-feature converter for healthcare applications

Mikhail Manokhin

► **To cite this version:**

Mikhail Manokhin. Towards flexible and low-power wireless smart sensors : reconfigurable analog-to-feature converter for healthcare applications. Optics / Photonics. Institut Polytechnique de Paris, 2024. English. NNT : 2024IPPAT049 . tel-04910169

HAL Id: tel-04910169

<https://theses.hal.science/tel-04910169v1>

Submitted on 24 Jan 2025

HAL is a multi-disciplinary open access archive for the deposit and dissemination of scientific research documents, whether they are published or not. The documents may come from teaching and research institutions in France or abroad, or from public or private research centers.

L'archive ouverte pluridisciplinaire **HAL**, est destinée au dépôt et à la diffusion de documents scientifiques de niveau recherche, publiés ou non, émanant des établissements d'enseignement et de recherche français ou étrangers, des laboratoires publics ou privés.



INSTITUT
POLYTECHNIQUE
DE PARIS

NNT : 2024IPPAT049

Thèse de doctorat

TELECOM
Paris



INSTITUT POLYTECHNIQUE
DE PARIS IP PARIS

Towards flexible and low-power wireless smart sensors: reconfigurable analog-to-feature converter for healthcare applications

Thèse de doctorat de l'Institut Polytechnique de Paris
préparée à Télécom Paris

École doctorale n°626 École doctorale de l'Institut Polytechnique de Paris (ED IP Paris)
Spécialité de doctorat : Électronique et Optoélectronique

Thèse présentée et soutenue à Palaiseau, le 13 décembre 2024, par

MIKHAIL MANOKHIN

Composition du Jury :

Rachid Bouchakour Professeur, Aix-Marseille Université	Président / Examineur
Hervé Barthélémy Professeur, Université de Toulon	Rapporteur
Philippe Bénabès Professeur, CentraleSupélec	Rapporteur
Caroline Lelandais-Perrault Maîtresse de conférences, CentraleSupélec	Examinatrice
Michael Pelissier Ingénieur de recherche, Université Grenoble-Alpes (CEA-Leti)	Examineur
Patricia Desgreys Professeure, Télécom Paris (LTCl)	Directrice de thèse
Paul Chollet Maître de conférences, Télécom Paris (LTCl)	Co-encadrant

Abstract

Current human population growth and aging inevitably raise the rate of chronic diseases, the leading global cause of death. Wireless Body Area Networks (WBANs) composed of smart wearable or implantable sensors are the primary solution for proactive healthcare systems to reduce the burden of these diseases. However, such networks are severely restricted regarding energy usage and data throughput, especially in the case of biopotential and inertial sensors requiring continuous signal acquisition. Reducing the amount of collected and sent data, thus improving sensors' autonomy, is possible in classification applications. For this purpose, this thesis aims to design a reconfigurable Analog-to-Feature (A2F) converter that extracts only relevant features for a given task in the analog domain within the sensor node and classifies further at the sensor or aggregator level. Based on Non-Uniform Wavelet Sampling (NUWS), our converter leverages a generic architecture to suit different low-frequency signals and enable WBANs with multimodal sensors. To prove the converter's universality, we address two applications: anomaly detection in electrocardiogram (ECG) signals and human activity recognition (HAR) in inertial signals. After training the neural network classifiers for each application, we defined the relevant features and hardware specifications required for the complete circuit design. Thanks to the circuit level simulation of the converter, we can show that the estimated energy consumption is divided by 20 for ECG and 5 for HAR compared to the Nyquist approach. This fact highlights the potential of A2F conversion with NUWS in achieving flexible, reliable, and low-power sensor systems for healthcare and beyond.

Keywords: Analog-to-Feature converter, Wireless Body Area Networks, Smart sensors, Non-Uniform Wavelet Sampling, Arrhythmia detection, Human activity recognition.

Résumé

Cette thèse aborde les défis actuels liés au vieillissement de la population mondiale et à l'augmentation des maladies chroniques, qui représentent la principale cause de décès à l'échelle mondiale. Ces maladies non-transmissibles, comme les maladies cardiovasculaires et le diabète, sont exacerbées par des modes de vie sédentaires, une urbanisation rapide et des habitudes alimentaires déséquilibrées. Le besoin d'un système de santé proactif et économique, capable de détecter ces maladies précocement et de surveiller les patients en continu, est impératif, en particulier dans les régions où les ressources médicales sont limitées.

Les réseaux corporels sans fil (WBANs), composés de capteurs portables ou implantables, se présentent comme une solution prometteuse pour répondre à ces besoins. Cependant, les WBANs sont confrontés à des contraintes strictes en matière de consommation énergétique et de débit de données, en particulier dans les applications nécessitant une acquisition continue des signaux. Cette thèse propose une approche novatrice pour améliorer l'autonomie des capteurs en réduisant les données collectées et transmises grâce à un convertisseur analogique-paramètre (A2F) reconfigurable.

Basé sur l'échantillonnage non-uniforme en ondelettes (NUWS), ce convertisseur extrait uniquement les caractéristiques pertinentes des signaux analogiques directement au sein du nœud capteur, permettant une classification des données soit au niveau du capteur, soit à celui de l'agrégateur. L'objectif principal de cette recherche est de concevoir un convertisseur générique capable de traiter divers signaux basse fréquence (moins de quelques centaines de kilohertz), tout en répondant aux exigences spécifiques de deux applications étudiées : la détection d'anomalies dans les signaux d'électrocardiogramme (ECG) et la reconnaissance des activités humaines (HAR) à partir de signaux inertiels (accéléromètres et gyroscopes).

Contributions clés :

- Conception d'un convertisseur A2F générique et reconfigurable

Le convertisseur utilise une architecture innovante reposant sur le NUWS, qui permet d'obtenir des informations temporelles et fréquentielles des signaux d'entrée. Cette méthode, adaptée à divers types de signaux, assure la flexibilité et la fiabilité nécessaires pour les applications de santé.

- Étude de deux applications cibles

Pour l’ECG, l’objectif est de détecter les arythmies cardiaques grâce à une extraction efficace des caractéristiques pertinentes et une classification binaire.

Pour la HAR, la reconnaissance des activités humaines se concentre sur des tâches de classification multi-classes et binaires, démontrant la polyvalence du convertisseur.

- Sélection des caractéristiques et classification

Les simulations réalisées comprennent l’entraînement et l’évaluation de classificateurs de réseaux neuronaux construits pour chaque application. Les résultats correspondants ont permis de définir les paramètres pertinents et les spécifications matérielles requises pour la conception du circuit complet.

- Conception matérielle et simulations circuit du convertisseur

Le cœur de cette thèse réside également dans la conception matérielle du convertisseur A2F. Un intégrateur G_m -C, élément critique du système, a été simulé au niveau schématique pour garantir une fréquence de coupure suffisamment basse pour les deux applications. Ces simulations montrent que le système peut s’adapter aux contraintes de conception des circuits analogiques tout en maintenant une performance élevée.

- Efficacité énergétique

Les estimations de consommation énergétique indiquent que le convertisseur A2F permet de réduire de manière significative la consommation par rapport aux approches traditionnelles basées sur l’échantillonnage à la Nyquist. En effet, les simulations montrent une réduction par un facteur de 20 pour l’ECG et de 5 pour la HAR.

Perspectives et implications :

Les résultats de cette thèse démontrent le potentiel du convertisseur A2F à révolutionner les systèmes de capteurs de santé. En intégrant l’extraction et la classification des caractéristiques directement dans le capteur, cette approche offre une solution économe en énergie et adaptable pour les WBANs. Les futures recherches pourraient explorer des optimisations supplémentaires, l’intégration de nouvelles applications, et le développement de prototypes pour des tests en conditions réelles.

En conclusion, cette thèse constitue une contribution significative au domaine des capteurs intelligents sans fil et ouvre la voie à des systèmes de santé plus flexibles, fiables et à faible consommation énergétique, capables de répondre aux besoins croissants de la surveillance médicale proactive.

Mots-clés : Convertisseur analogique-paramètre, Réseaux corporels sans fil, Capteurs intelligents, Échantillonnage non-uniforme en ondelettes, Détection d’arythmie, Reconnaissance des activités humaines.

Acknowledgments

First and foremost, I express my deepest gratitude to my thesis director, Patricia DESGREYS, and my supervisor, Paul CHOLLET. Your unwavering support, invaluable advice, and guidance over the past three years were indispensable for my success. Our discussions on diverse topics, especially in challenging moments, provided immense learning and comfort.

I am thankful to Antoine, who previously worked on the same subject. It was a privilege to build upon your bright ideas and develop them within the scope of my thesis. By the way, thank you for introducing me to the art of drawing plots and circuit diagrams with \LaTeX .

I am profoundly grateful to the jury members – reviewers Hervé BARTHÉLÉMY and Philippe BÉNABÈS, and examiners Rachid BOUCHAKOUR, Caroline LELANDAIS-PERRAULT, and Michael PELISSIER – for accepting their roles. Your remarks on the manuscript and insightful questions and comments during the defense significantly enriched my work.

Chadi, Germain, Yves, Tarik, Lirida, and other members of the COMELEC department, thank you for your assistance with technical and software tools, and administrative procedures.

To former and current PhD students and postdocs whose paths have crossed mine – Lyliya, Zülal, Evelyn, Haoyang, Ahmed, Thuy, Zhu, Dina, Albert, Ecem, Awais, Neelam, Akram, Nicolas, Zhengyi, André, Martina, Thomas, Tayeb – you made this journey unforgettable. Your humor maintained positive vibes and a friendly atmosphere, while our lunches at Crous and post-meal conversations were a source of immense joy.

Special thanks to everyone who joined our short but memorable trip to Marseille. I am grateful to Zülal for being a kind, generous friend since our master’s program. Nicolas, your remarkable creativity and gorgeous, hilarious drawings never failed to make me smile. Zhengyi, thank you for organizing an astonishing local barbershop with free haircuts and capturing the best moments of our summer trip with your outstanding photography. Ahmed and Dina, your regular distractions taught me the art of maintaining focus while staying cheerful. Awais, our table tennis sessions were a delight, and I hope we play again soon.

Lastly, but most importantly, I owe everything to my parents, relatives, and my wife, Evgeniya. None of this would have been possible without your support, love, and belief in me. To everyone who played a role in this journey – thank you from the depths of my heart.

Contents

Abstract	I
Résumé	III
Acknowledgments	V
Table of contents	VI
List of Figures	XI
List of Tables	XV
List of abbreviations	XIX
Publications and communications	XXIII
Introduction	1
1 Biosignals processing for wireless healthcare sensors	5
1.1 Global health crisis: aging and chronic diseases	5
1.2 Wireless Body Area Networks (WBANs): primary solution for new healthcare systems	6
1.2.1 Communication architecture	7
1.2.2 Medical and non-medical applications	7
1.2.3 Sensor nodes	8
1.2.3.1 Classification of sensors	9
1.2.3.2 Analog-to-digital converter (ADC) architectures	10
1.2.3.3 Wireless transmitters	12
1.2.4 Major constraints and challenges in WBANs	13
1.2.5 Energy-efficient approach for applications employing classification . . .	14
1.2.6 Conclusion on WBANs	15
1.3 Classification applied to biopotential and inertial signals	16
1.3.1 Introduction to classification with Machine Learning (ML)	16

1.3.1.1	Supervised classification workflow	16
1.3.1.2	Performance evaluation metrics	17
1.3.2	Arrhythmia diagnosis in electrocardiogram (ECG) signals	20
1.3.2.1	Introduction to ECG recordings	21
1.3.2.2	Data collection	22
1.3.2.3	Preprocessing	22
1.3.2.4	Feature engineering	24
1.3.2.5	Classification	25
1.3.3	Human activity recognition in inertial signals	28
1.3.3.1	Data collection	28
1.3.3.2	Preprocessing	28
1.3.3.3	Feature engineering	29
1.3.3.4	Classification	29
1.3.4	Conclusion on classification in biopotential and inertial signals	32
1.4	Alternative acquisition techniques	32
1.4.1	Analog-to-Information (A2I) conversion: compressive sampling (CS) acquisition	33
1.4.1.1	The principle of CS	33
1.4.1.2	A2I converter architectures	35
1.4.1.3	Reconstruction algorithms	37
1.4.2	Analog-to-Feature (A2F) conversion: combining acquisition and feature extraction	38
1.4.3	Conclusion on alternative acquisition techniques	40
1.5	Conclusion	40
2	Reconfigurable generic Analog-to-Feature converter	43
2.1	A2F converter based on Non-Uniform Wavelet Sampling (NUWS)	44
2.1.1	Reconfigurable A2F architecture	44
2.1.2	NUWS-based feature extraction	45
2.1.2.1	Continuous Wavelet Transform (CWT) and NUWS	45
2.1.2.2	The architecture of feature extractor	46
2.1.3	Conclusion on the proposed A2F converter	47
2.2	Data preparation	48
2.2.1	Description of datasets' signals	48
2.2.1.1	ECG recordings	48
2.2.1.2	Inertial measurements	49
2.2.2	Shaping datasets' signals	49
2.2.2.1	Arrhythmia detection	49
2.2.2.2	Human activity recognition	50
2.2.3	Conclusion on data preparation	50

2.3	Feature extraction	51
2.3.1	Choice of wavelet families	51
2.3.1.1	Haar wavelets	51
2.3.1.2	Gabor wavelets	52
2.3.2	Generation of wavelet dictionaries	53
2.3.3	Conclusion on feature extraction	54
2.4	Feature selection	56
2.4.1	Filter methods	56
2.4.1.1	Fisher Score (FS)	56
2.4.1.2	Information Gain (IG)	57
2.4.2	Wrapper methods	57
2.4.2.1	Basic Sequential Forward Search (SFS)	58
2.4.2.2	Adapted SFS	59
2.4.2.3	Optimized SFS	60
2.4.3	Discussion on feature selection	61
2.5	Classification algorithms	61
2.5.1	Random Forest (RF)	61
2.5.2	Support Vector Machine (SVM)	62
2.5.3	Artificial Neural Network (NN)	64
2.5.4	Conclusion on classification algorithms	65
2.6	Conclusion	67
3	Simulation results for healthcare applications	69
3.1	Arrhythmia detection in ECG signals	70
3.1.1	Comparison of different filter methods and classification models	70
3.1.2	Impact of the basic SFS algorithm	71
3.1.3	Classification with improved SFS algorithms	72
3.1.3.1	Adapted SFS to limit the number of extractors	73
3.1.3.2	Optimized SFS to limit the consumption	74
3.1.4	Discussion on arrhythmia detection	75
3.2	Human activity recognition in inertial signals	76
3.2.1	Performance of classifiers with initial settings	76
3.2.1.1	Multi-class classification	77
3.2.1.2	One-vs-all binary classification	78
3.2.2	Improved performance of multi-class classifiers with the basic SFS	80
3.2.2.1	Adjustments in wavelet dictionaries and NN initialization	80
3.2.2.2	Choice of NN structure and wavelet family	82
3.2.3	Adapted SFS to limit the number of extractors	83
3.2.3.1	Multi-class classification	83
3.2.3.2	One-vs-all binary classification	84

3.2.3.3	Comparison of binary and multi-class classifiers	86
3.2.4	Discussion on human activity recognition	87
3.3	Conclusion	88
4	Hardware design of the Analog-to-Feature converter	91
4.1	Required specifications	92
4.1.1	Overall architecture of the acquisition system	92
4.1.2	Feature extraction	94
4.1.3	Digitization	95
4.2	Review of existing hardware solutions	97
4.2.1	Amplification stage	97
4.2.2	Wavelet generator	98
4.2.3	ADC	98
4.2.4	Integrator	98
4.3	G_m -C integrator design	99
4.3.1	Architecture and its functioning principle	99
4.3.2	Direct current (DC) simulations	101
4.3.3	Alternating current (AC) simulations	101
4.3.4	Input common-mode voltage	102
4.3.5	Biasing voltages	103
4.4	Classification with non-ideal integration coefficients	104
4.5	Evaluation of energetic efficiency	106
4.5.1	Energetic cost of feature extraction and digitization	107
4.5.2	Consumption estimations	107
4.5.2.1	Classification at aggregator	107
4.5.2.2	Classification within sensor	109
4.5.2.3	Comparison to existing embedded designs	111
4.6	Conclusion	112
	Conclusions and Perspectives	115
	Bibliography	119

List of Figures

1.1	WBAN's communication architecture	7
1.2	Two approaches in wireless sensor networks with classification: feature extraction at aggregator or within sensor	14
1.3	Workflow of a supervised classification	16
1.4	Binary confusion matrix	17
1.5	Binary classification metrics relative to (a) true and (b) predicted classes . . .	18
1.6	ECG waveform with indicated PQRST complex, intervals, and segments	22
1.7	Main steps of Compressive Sampling	33
1.8	Example of compressible signal sparse in frequency	34
1.9	Architecture of Non-Uniform Sampling	35
1.10	Architecture of Random Demodulator	35
1.11	Architecture of Modulated Wideband Converter	36
1.12	Architecture of Non-Uniform Wavelet Sampling	37
1.13	Two approaches in A2F conversion: classification at aggregator or in sensor . .	39
2.1	Acquisition system architecture with reconfigurable A2F converter	45
2.2	Architecture of NUWS-based feature extractor	47
2.3	Examples of non-overlapping and overlapping wavelet supports	47
2.4	Distribution of data between six classes in (a) train and (b) test sets for HAR .	50
2.5	Position of data preparation step in the implementation workflow of the generic A2F converter	51
2.6	Examples of first eight basic Haar wavelets	52
2.7	Example of real and imaginary parts of Gabor wavelet	53
2.8	Example of first 26 Haar wavelets used in simulations	54
2.9	Position of feature extraction step in the implementation workflow of the generic A2F converter	55
2.10	Example of two non-overlapping Haar wavelets producing the NUWS-based features that can be extracted by the same extractor	59
2.11	Simplified Random Forest algorithm	62
2.12	Support Vector Machine's operating principle in two-dimensional feature space with linearly separable data	63

2.13	Single artificial neuron's structure	65
2.14	An example of a feedforward Neural Network	66
2.15	Position of feature selection and classification step in the implementation workflow of the generic A2F converter	67
2.16	Detailed implementation workflow of the generic A2F converter	68
3.1	Accuracy of binary arrhythmia detection performed by different classifiers built using Scikit-Learn and based on input features sorted directly by filter methods	70
3.2	Accuracy of binary arrhythmia detection performed by NN classifiers built using Scikit-Learn and TensorFlow and based on input features sorted directly by IG criterion	71
3.3	Impact of basic SFS algorithm on binary arrhythmia detection performed by NN classifiers: (a) feature selection only with IG; (b) feature selection with IG + basic SFS	72
3.4	Metrics of binary arrhythmia detection performed by NN classifiers with IG + adapted SFS feature selection	73
3.5	Metrics of binary arrhythmia detection performed by NN classifiers with IG + optimized SFS feature selection	75
3.6	Accuracy of the multi-class HAR performed by NN classifiers with initial settings and different wavelet families and feature selection procedures	77
3.7	Confusion matrices of two preferred NN classifiers performing the multi-class HAR with different wavelet families and IG + basic SFS feature selection	78
3.8	<i>MCC</i> of one-vs-all binary HAR performed by NN classifiers with IG + basic SFS feature selection and different wavelet families: (a) Haar wavelets; (b) Gabor wavelets	79
3.9	ROC curves of one-vs-all binary HAR performed by NN classifiers with IG + basic SFS feature selection and different wavelet families: (a) Haar; (b) Gabor	79
3.10	Impact of improved dictionaries and NN initialization on the multi-class HAR performed by NN classifiers with Haar wavelets and IG + basic SFS feature selection	81
3.11	Confusion matrices of two improved NN classifiers with 15 input features performing the multi-class HAR with IG + basic SFS feature selection	82
3.12	Accuracy of the multi-class HAR performed by NN classifiers of different structure with different wavelet families and IG + basic SFS feature selection	82
3.13	Confusion matrices of NN classifiers using different wavelet families and performing the multi-class HAR with IG + basic SFS feature selection in the features/accuracy trade-off points	83
3.14	Accuracy of the multi-class HAR performed by NN classifiers with Haar wavelets and IG + adapted SFS feature selection	84

3.15	Accuracy of the multi-class HAR performed by NN classifiers with Haar wavelets, features extracted from acceleration signals, and IG + adapted SFS feature selection	85
3.16	<i>MCC</i> of one-vs-all binary HAR performed by NN classifiers with Haar wavelets and IG + adapted SFS feature selection	85
4.1	Hardware implementation of the acquisition system with the A2F converter satisfying the two studied applications	92
4.2	Impact of the quantification level on the accuracy of the multi-class HAR performed by NN classifiers with Haar wavelets and IG + adapted SFS feature selection limited to eight extractors	96
4.3	Transistor-level schematic of the G_m -C integrator proposed in [155]	100
4.4	Results of DC simulations in the open-loop configuration to determine control voltages (a) V_{t1} and (b) V_c	101
4.5	Results of AC simulations in the integrator configuration with $V_{CM} = 0.9$ V to determine control voltages V_{t2} and V_{gc} : (a) cut-off frequency F_c ; (b) DC gain error GE_{DC}	102
4.6	Impact of common-mode voltage V_{CM} values on (a) v_{in} - V_{out} characteristic and (b) cut-off frequency F_c and DC gain error GE_{DC}	103
4.7	Impact of biasing voltages on the integrator's performance characteristics . . .	104
4.8	Energy to process ten seconds of ECG signal with three wireless approaches . .	109
4.9	Energy to process ten seconds of inertial signals with two wireless approaches .	109
4.10	Energy to process ten seconds of ECG signal with two A2F approaches	110
4.11	Energy to process ten seconds of inertial signals with two A2F approaches . . .	111

List of Tables

1.1	Applications of WBANs [8, 10, 25]	8
1.2	Common biosensors in WBANs and their characteristics [8, 10, 24, 26]	9
1.3	Characteristics of ADCs	11
1.4	Characteristics of wireless transmitters	12
1.5	Heartbeat classification as per the ANSI/AAMI EC57 standard	21
1.6	Input ECG data and preprocessing methods in studies performing arrhythmia diagnosis in ECG recordings from the MITDB	23
1.7	Hand-crafted features extracted in studies performing arrhythmia diagnosis in ECG recordings from the MITDB	25
1.8	Classification methods and performances in studies performing arrhythmia diagnosis in ECG recordings from the MITDB	26
1.9	Features extracted from signals in the UCI-HAR dataset	29
1.10	Classification methods and performances in studies performing HAR in inertial signals from the UCI-HAR dataset	30
1.11	Complexity and minimum number of required measurements in several well-known sparse recovery algorithms [130, 131]	38
2.1	Comparison of original sample counts in the utilized datasets to initial wavelet dictionary sizes	55
2.2	Comparison of supervised ML algorithms for classification	66
3.1	Comparison of MCC values obtained by multi-class and binary HAR classifiers	86
3.2	Performance summary of multi-class and binary HAR classifiers	86
3.3	Comparison of different classification models performing multi-class HAR on the UCI-HAR dataset	87
4.1	Features selected for extraction in the multi-class HAR from $acc_{x,y} + gyr_z$ signals	93
4.2	Features selected for extraction in the binary arrhythmia detection	94
4.3	Summary of required specifications for hardware implementation of the feature extraction and digitization chain	97
4.4	Performances of amplification stages from state-of-the-art front-end designs . .	97

4.5	Performances of first-order LPFs with a sub-Hertz cut-off frequency	99
4.6	Best V_{t2} , V_{gc} pairs with the lowest cut-off frequencies F_c from AC simulations with $V_{CM} = 0.9\text{ V}$	102
4.7	Best V_{t2} , V_{gc} pairs with the lowest cut-off frequencies F_c from AC simulations with $V_{CM} = 0.6\text{ V}$	103
4.8	Integrator's biasing, control voltages and performance summary	104
4.9	Re-evaluation of NN classifiers using non-ideal integrator's outputs	105
4.10	Estimated energy consumption to extract and transmit features from ten seconds of studied signals using A2F conversion with classification at aggregator .	108

List of abbreviations

A2F	Analog-to-Feature
A2I	Analog-to-Information
AAMI	Association for the Advancement of Medical Instrumentation
AC	Alternating current
ADC	Analog-to-digital converter
ADL	Activity of Daily Living
AFE	Analog front-end
ANSI	American National Standards Institute
ASIC	Application-specific integrated circuit
BFSK	Binary Frequency Shift Keying
BiLSTM	Bidirectional Long Short-Term Memory
BLE	Bluetooth Low Energy
CAE	Convolutional Auto-Encoder
CMOS	Complementary Metal-Oxide-Semiconductor
CNN	Convolutional Neural Network
CS	Compressive sampling
CVD	Cardiovascular disease
CWT	Continuous Wavelet Transform
DC	Direct current

DL	Deep Learning
DL-CCANet	Dual-lead canonical correlation analysis network
DOWN	Walking downstairs
DR	Dynamic range
DT	Decision Tree
DWT	Discrete Wavelet Transform
ECG	Electrocardiogram
EEG	Electroencephalogram
EMD	Empirical Mode Decomposition
EMG	Electromyogram
ENOB	Effective number of bits
FFT	Fast Fourier Transform
FN	False negative
FoM	Figure of merit
FP	False positive
FPGA	Field Programmable Gate Array
FPR	False positive rate
FS	Fisher Score
GA	Genetic algorithm
GPU	Graphics processing unit
GRU	Gated Recurrent Unit
HAR	Human activity recognition
HBC	Human Body Communication
ICA	Independent Component Analysis
IG	Information Gain

IMF	Intrinsic Mode Function
IoT	Internet of Things
KNN	K-Nearest Neighbours
LAY	Laying
LDA	Linear Discriminant Analysis
LNA	Low Noise Amplifier
LPF	Low-pass filter
LSTM	Long Short-Term Memory
MCC	Matthews correlation coefficient
MITDB	MIT-BIH Arrhythmia Database
ML	Machine Learning
MLP	Multi-layer perceptron
NB	Narrowband
NCD	Non-communicable disease
NN	Neural Network
NPV	Negative predictive value
NUS	Non-Uniform Sampling
NUWS	Non-Uniform Wavelet Sampling
OTA	Operational transconductance amplifier
PCA	Principal Component Analysis
PD	Personal device
PGA	Programmable Gain Amplifier
PN	Predicted negative
PP	Predicted positive
PPV	Positive predictive value

RBF	Radial Basis Function
RD	Random Demodulator
RF	Random Forest
RMPI	Random Modulator Pre-Integrator
ROC	Receiver operating characteristic
S&H	Sample-and-hold
SAR	Successive-approximation register
SD	Standard deviation
SFFS	Sequential Floating Forward Search
SFS	Sequential Forward Search
SIT	Sitting
SMOTE	Synthetic minority oversampling technique
STD	Standing
SVM	Support Vector Machine
TN	True negative
TNR	True negative rate
TP	True positive
TPR	True positive rate
UP	Walking upstairs
UWB	Ultra Wideband
WALK	Walking
WBAN	Wireless Body Area Network
WHO	World Health Organization
WSN	Wireless Sensor Network
ZeroR	Zero Rule

Publications and communications

Journals

[Sensors24] Mikhail MANOKHIN, Paul CHOLLET and Patricia DESGREYS.
Towards Flexible and Low-Power Wireless Smart Sensors: Reconfigurable Analog-to-Feature Conversion for Healthcare Applications.
In *Sensors (MDPI)*

International conferences

[NEWCAS23] Mikhail MANOKHIN, Paul CHOLLET and Patricia DESGREYS.
Flexible Analog-to-Feature Converter for Wireless Smart Healthcare Sensors.
In *21st IEEE International New Circuits and Systems Conference (NEWCAS)*, June 2023, Edinburgh, Scotland.

National conferences

[GDR-SoC2-22] Mikhail MANOKHIN, Paul CHOLLET and Patricia DESGREYS.
Design optimization of flexible analog-to-feature converter for smart sensors.
In *Colloque du GDR SOC2* June 2022, Strasbourg, France.

Introduction

According to the United Nations projections [1], the global population is set to grow from 8.2 to 9.7 billion people by 2050, with life expectancy increasing from 73.3 to around 77 years. This growth, along with declining birth rates, leads to an aging population, with those over 65 showing the quickest growth rate among all age groups. Elderly people face a higher risk of chronic diseases (NCDs), which account for 74% of global deaths [2]. Cardiovascular diseases are the leading cause of deaths caused by NCDs. Multiple factors, including unhealthy lifestyles, rapid unplanned urbanization, and air pollution, increase the risk of developing the NCDs. The World Health Organization (WHO) warns that these diseases could be responsible for 86% of deaths by 2050 if their current rise persists [3]. Early detection of NCDs can effectively prevent them and decrease the cost of medical care [4–7]. However, conventional healthcare systems rely on reactive treatment and rarely detect NCDs early enough.

Recent progress in microelectronics and other fields has led to the emergence of Wireless Sensor Networks (WSNs) in healthcare. These networks, called Wireless Body Area Networks (WBANs) and composed of wearable or implantable sensors, represent a primary solution for building the required cost-effective and proactive healthcare systems [8]. Since WBAN sensors are heavily limited in available energy [9, 10], improving their energetic efficiency is crucial. In anomaly detection or event classification applications, sensors that capture their signals continuously, e.g., biopotential and inertial, can significantly benefit from reducing transmitted data amounts and related consumption by extracting features and sending them instead of conventional Nyquist-rate samples. Hence, our research focuses on these sensors.

Following the study in [11], this thesis aims to design a reconfigurable generic Analog-to-Feature (A2F) converter suitable for various types of low-frequency (below hundreds of kilohertz) signals and lay the foundation for its hardware implementation. For this purpose, we address two applications: binary arrhythmia detection in electrocardiogram (ECG) signals and human activity recognition (HAR) in accelerometer and gyroscope signals. The developed converter leverages the feature extraction based on the Non-Uniform Wavelet Sampling (NUWS) technique, which is adaptable to different types of signals.

In Chapter 1, we first review state-of-the-art feature extraction and classification techniques applied to arrhythmia diagnosis in ECG signals and HAR in inertial sensors. Computationally and energy-wise costly and application-specific, these methods are often unsuitable for in-sensor implementation and non-extensible to other applications. Second, by studying

the alternative acquisition techniques that capture less data from the analog domain, we spot the A2F conversion as a potentially effective approach for transmitted data amount and respective consumption reduction. It allows extracting only features relevant for classification from the analog signal directly within the sensor [12]. The NUWS technique [13], proposed as the Analog-to-Information (A2I) conversion architecture to extract useful wavelet coefficients from the radio-frequency signals, allows obtaining temporal and frequency information about the input signal at once. Due to its multiple degrees of freedom, it is adaptable to different types of signals and thus is a good candidate for feature extraction in the A2F converter.

Chapter 2 describes the chosen A2F converter’s architecture, details the NUWS technique, and outlines the implementation workflow applied throughout the thesis. The workflow comprises the application-specific steps – data preparation, feature extraction, feature selection, and classification – and the definition of hardware specifications for the multi-application suitability. Data preparation performs manipulations on the signals issued from the datasets. Feature extraction produces NUWS-based features from the prepared data. The joint feature selection and classification step first preselects the 100 best features according to the Fisher Score (FS) or Information Gain (IG). Then, it iteratively constructs classifiers using the Sequential Forward Search (SFS) algorithm, which chooses the features for the classifier’s inputs that improve its prediction performance.

In Chapter 3, we train and evaluate classifiers for both studied applications: binary arrhythmia detection in ECG signals and multi-class and one-vs-all binary HAR in accelerometer and gyroscope signals. To build the classifiers, we employ three supervised Machine Learning (ML) models: Random Forest (RF), Support Vector Machine (SVM), and feedforward Neural Network (NN). From the results, we choose the classifiers providing the best trade-off between the obtained classification performance and the required number of input NUWS-based features. Hence, we identify the features that are relevant to each application’s classification and that are to be extracted in advance by the A2F converter.

In Chapter 4, we lay the foundation for the hardware implementation of the A2F converter. For this purpose, we first derive the specifications based on features considered relevant in the preferred classifiers built in Chapter 3. Next, we review the recent hardware solutions available for the principal converter’s components. We perform the schematic-level simulations of the G_m -C integrator, a critical component, based on the design found in the literature. Aiming to achieve its cut-off frequency low enough for our applications, we determine its control and biasing voltages and evaluate its performance. Next, we evaluate the NN classifiers with more realistic non-ideal integration coefficients produced by the simulated G_m -C integrator to evidence the A2F converters’ ability to mitigate design constraints imposed on such analog circuits as integrators. Finally, based on the integrator’s revised power consumption and the values borrowed from the state-of-the-art designs for other components, we estimate the energetic efficiency of our communication chain comprising the A2F converter to show its potential in achieving flexible, low-power WBAN sensors in healthcare and beyond.

The final Chapter wraps up the research presented in this thesis and highlights future research directions, including possible challenges and potential improvements.

In summary, the contributions of this thesis include:

- re-implementation of feature extraction, feature selection, and classification in more advanced software to enhance the efficiency of the ML algorithms, particularly NNs, and speed up calculations using graphics processing units (GPUs) & re-production of the simulation results obtained in [11] for binary arrhythmia detection in ECG signals with a slight improvement in classification performance;
- comprehensive study on a newly proposed application in the form of HAR in inertial signals with a focus on multi-class classification to prove the genericity of the developed A2F converter;
- circuit-level design of a critical converter's component, G_m -C integrator, that provides a significantly low sub-Hz cut-off frequency to suit both explored applications;
- evaluation of the NN classifiers with more realistic non-ideal integration coefficients to show the ability of the NUWS-based A2F converter to mitigate design constraints imposed on such analog circuits as integrators;
- estimation of the energetic efficiency of the communication chain with the A2F conversion and its comparison to recent embedded designs with in-sensor classification.

Chapter 1

Biosignals processing for wireless healthcare sensors

1.1 Global health crisis: aging and chronic diseases

According to the recent projections published by the United Nations in 2024 [1], the human population continues to grow rapidly. By 2050, it will reach 9.7 billion, which is 18% higher than the current count of 8.2 billion. At the same time, the global life expectancy at birth should continue to rise from 73.3 years in 2024 to around 77 in 2050. The fact that people are living longer now, combined with the continuing decline in fertility at the global scale, leads to the aging of the world's population. Indeed, elderly people (over 65) already show the quickest growth rate among all age groups. Moreover, we expect them to overtake the number of people under 18 before the second half of the 2070s.

Elderly people are more at risk of developing health issues and are also more prone to suffer from chronic or so-called non-communicable diseases (NCDs). Such diseases are the most dominant cause of human deaths globally and account for 74% of them, according to the World Health Organization (WHO) [2]. In 2021, seven of ten leading causes of death at a global level were NCDs [14,15], despite COVID-19 rapidly rising to second place two years after its emergence. Cardiovascular diseases (such as heart attacks and stroke) are responsible for 44% of NCD deaths and thus account for one-third of all human deaths in the world. Cancers, chronic respiratory diseases (such as chronic obstructive pulmonary disease and asthma), and diabetes (including kidney disease caused by diabetes) follow with 23%, 10%, and 5% of NCD deaths, respectively. These diseases are driven not simply by population aging but also by rapid unplanned urbanization and the spread of unhealthy lifestyles. There are three groups of factors that increase the risk of NCDs. Modifiable behavioral risk factors include smoking, harmful alcohol use, physical inactivity, and inappropriate eating habits. A sedentary lifestyle, lack of physical activity, and unhealthy diets may contribute to metabolic risk factors, such

as elevated blood pressure, high blood glucose levels, overweight, and obesity. The last group comprises environmental risk factors, with air pollution being the most significant contributor.

According to WHO, despite the overall recent progress in health, if the number of NCDs continues to rise with the current trend, they could account for 86% of all annual human deaths by around 2050 [3]. Therefore, it is critical to invest in better management of NCDs, encompassing permanent control of risk factors and early diagnosis, constant screening, and timely treatment of diseases. Indeed, as demonstrated in multiple studies [4–7], detecting NCDs by the visible symptoms at early stages can not only effectively prevent these diseases but also decrease the overall healthcare cost by avoiding potentially much more expensive treatment. Such investments will be economically profitable, significantly reduce the burden of NCDs, and improve the quality of life. However, conventional healthcare systems often fail to detect these diseases early enough and rely on reactive treatment models. Hence, humanity needs new, cost-effective, real-time, ubiquitous healthcare monitoring systems that enable proactive and affordable disease prevention and management. Such systems would be especially helpful for resource-constrained regions lacking conventionally trained healthcare staff and infrastructure and for elderly people or patients already suffering from chronic illnesses, as they would receive continuous healthcare while remaining home.

1.2 Wireless Body Area Networks (WBANs): primary solution for new healthcare systems

The modern world is witnessing a growing scientific interest in Wireless Sensor Networks (WSNs): networks consisting of multiple spatially dispersed, independent sensors that monitor environmental and physical data and collectively transmit it to a central station serving as an aggregator [16]. The fast progress obtained in such networks, along with the rapid advancement of the Internet of Things (IoT), has led to the development of context-aware smart sensors deployed across numerous fields, such as precision agriculture [17], industry [18], transportation [19], security [20], education services [21], and healthcare [22].

Recent advances in microelectronics and intelligent micro- and nanotechnologies have made it possible to collect physical, physiological, psychological, and behavioral human data and have driven the integration of WSNs into healthcare. Such networks take the form of Wireless Body Area Networks (WBANs) composed of wearable or implantable sensors, providing ubiquitous health monitoring and early detection. Therefore, WBANs are the primary solution for building cost-effective and proactive healthcare systems [8]. IEEE 802.15.6 standard defines WBANs as real-time, wireless, short-range communication systems consisting of extremely low-power, intelligent, compact sensors and actuators communicating in, on, or around the human body for diverse medical and non-medical applications [23].

1.2.1 Communication architecture

The communication architecture of WBANs is segmented into three levels, as illustrated in Figure 1.1. Tier-1 implements an intra-WBAN communication and consists of on-body, wearable, or implantable sensor nodes that capture and process crucial physiological and environmental signals, measure additional contextual information such as location, interconnect each other if applicable, and provide timely data to the personal device (PD) [9]. Sometimes, sensors are connected to the PD via cables to avoid a wireless network in the first tier. Otherwise, sensor data is communicated wirelessly to the PD directly in single-hop WBANs for a lower delay or through an intermediate coordinator (aggregator) over ultra-short distances in multi-hop WBANs for a lower power [24]. Smartphones, personal computers, or other rechargeable electronic devices with greater computing capabilities than sensors can serve as PDs that gather and process the collected data. Tier-2, i.e., inter-WBAN communication, is realized between the PD and one or more access points (hub, base station) through such wireless transmission technologies as Wi-Fi, Bluetooth, ZigBee, and LoRa, depending on range, consumption, and data rate requirements. Tier-3, i.e., beyond-WBAN communication, defines the interaction between an access point and a remote server (medical center, hospital, emergency, family members, database, etc.) via the Internet or cellular network.

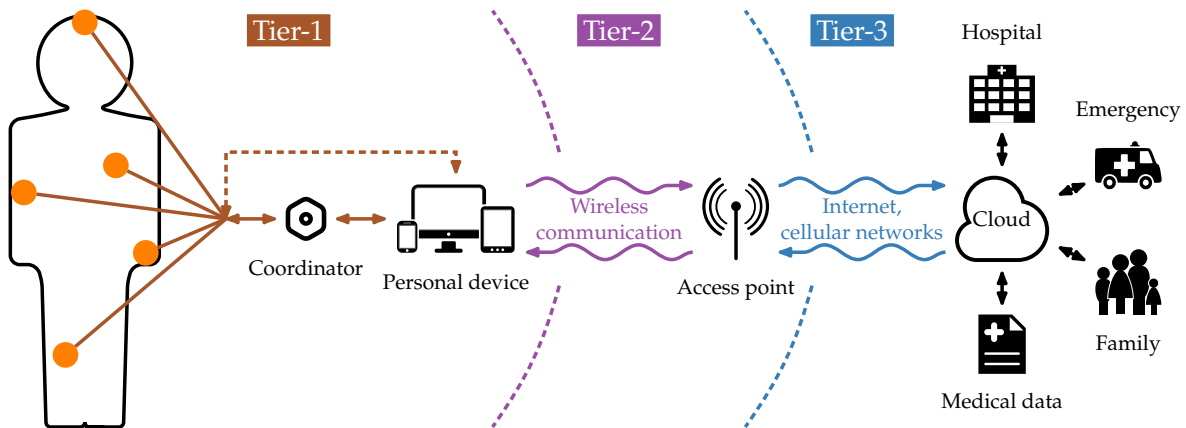


FIGURE 1.1 – WBAN’s communication architecture

1.2.2 Medical and non-medical applications

In general, WBANs have various current and potential future applications in human-related fields, such as healthcare, sports, entertainment, and the military, as illustrated in Table 1.1. Medical applications of WBANs, usually classified into subcategories of wearable and implantable WBANs, span from ubiquitous health and vital signs monitoring, telemedicine systems, disease prevention, and fall detection to ambient assisted living, aiding in sports training and behavioral studies. In a non-medical context, WBANs are widely used for real-

TABLE 1.1 – Applications of WBANs [8, 10, 25]

Category	Subcategory	Application
Medical	Wearable WBAN	<ul style="list-style-type: none"> • patient monitoring • asthma monitoring • telemedicine systems • fall detection & activity recognition • ambient assisted living • aiding in sport training • assessing soldier fatigue & battle readiness
	Implantable WBAN	<ul style="list-style-type: none"> • wearable health monitoring • sleep monitoring • behavioral studies • cardiovascular diseases • diabetes control • cancer detection • artificial retina
Non-medical	Real-time streaming	<ul style="list-style-type: none"> • video streaming • data file transfer • sports
	Emergency	<ul style="list-style-type: none"> • life-threatening conditions monitoring
	Entertainment & interactive learning	<ul style="list-style-type: none"> • social networking • education • gaming

time streaming, entertainment, interactive learning, and providing emergency warnings caused by life-threatening environmental conditions.

In this thesis, we focus on the medical field of WBANs' applications, which promise the most significant impact on human well-being. Effectively, the remote servers in the third tier of WBANs can store the received data and analyze it by medical specialists or smart algorithms. The obtained results serve for continuous remote monitoring of vital signs, identification of physiological symptoms, early diagnosis of diseases, quick response and alarm initiation in case of emergency, real-time feedback, and appropriate prescriptions to avoid complications. Hence, WBANs will ensure ubiquitous distant health monitoring, alleviating the need for patients to stay permanently at home or close to medical services. Moreover, WBANs will lower treatment and hospital costs, reduce the negative effect of inevitable demographic growth and population aging on the expansion of chronic diseases and shortage of healthcare facilities, and merely save people's lives.

1.2.3 Sensor nodes

Wireless sensor nodes are critical components in WBANs since they measure and transform physical parameters into signals, process necessary data, and communicate it wirelessly. Generally, these nodes consist of a sensor, a conditioning system, an analog-to-digital converter (ADC), a digital circuitry, and a wireless transmission system. A sensor usually converts the measured physical quantity into an electrical signal and provides an analog or digital signal at its output. Provided that, in most cases, the raw analog signal does not meet the ADC's input requirements, it undergoes amplification and filtering in the conditioning system to increase the amplitude and eliminate noise and parasitic components. ADC converts the conditioned signal into a digital form. Digital circuitry then ensures that the digital signal is processed,

optimized, and formatted for efficient and secure wireless transmission while managing power consumption and network requirements.

1.2.3.1 Classification of sensors

WBANs are usually heterogeneous, meaning they consist of sensors of different types [25]. Table 1.2 lists a few commonly used biosensors in WBANs and their crucial characteristics, such as produced signal type, required sampling frequency, and resulting communication data rate. Depending on their functions, we can classify biosensors into three groups: physiological, biokinetic, and ambient [10].

Physiological sensors provide real-time inspection of critical vital signs and body functions, enabling continuous monitoring, detection of health issues in early stages, and personalized healthcare in WBANs. Blood pressure sensors can continuously track systolic and diastolic arterial pressure, essential for patients with hypertension and cardiovascular diseases. Blood sugar sensors are crucial for managing diabetes and other metabolic conditions since they monitor glucose concentration in the blood and provide alerts for hypo- or hyperglycemia. Oximetry sensors indicate oxygen saturation levels in the bloodstream, which is especially important in high-altitude environments, fitness, and for patients with respiratory or cardiovascular diseases. Body temperature sensors can detect fever, hypothermia, or overheating. Electrocardiogram (ECG), electroencephalogram (EEG), and electromyogram (EMG) are intended to measure the electrical activity of the heart, brain, and muscles, respectively. ECG sensors provide data on heart rhythm and the functionality of the heart chambers, which are necessary to detect irregular heartbeats or other cardiac events. EEG sensors enable neurological monitoring, cognitive state tracking, and potential seizure activity detection in patients with epilepsy. EMG sensors provide indispensable data for rehabilitation and sports science about muscle contractions and relaxations during physical therapy or exercise.

TABLE 1.2 – Common biosensors in WBANs and their characteristics [8, 10, 24, 26]

Biosensor	Functional category	Type	Signal type	Sampling frequency	Data rate
Blood pressure		wearable		0.1–10 Hz	low
Blood sugar		wear./impl.	discrete	0.1–100 Hz	low/medium
Oximeter (SpO ₂)	physiolog.			0.1–10 Hz	low
Body T°		wearable		0.01–1 Hz	very low
ECG, EEG, EMG			continuous	0.1–1 kHz	high
Accelerometer, gyroscope	biokinetic	wearable	continuous	0.01–1 kHz	high
Humidity	ambient	wearable	discrete	0.01–1 Hz	very low

Accelerometers and gyroscopes, which belong to inertial measurement units (IMUs) or simply inertial sensors, are the most prominent examples of biokinetic sensors. Accelerometers measure linear acceleration and gravitational force upon the object, while gyroscopes measure angular velocity and orientation based on angular momentum. Plenty of other sensors, such as magnetometers, inclinometers, and goniometers, complement accelerometers and gyroscopes in health monitoring, sports, activity recognition, and rehabilitation by providing more precise and diverse data on human movement, posture, and physical activity. Magnetometers measure the strength and direction of the magnetic field for more accurate heading or direction determination. Inclinometers help in posture monitoring and fall detection by measuring the tilt angle or inclination of specific body parts with respect to gravity. Goniometers track the range of joint motion in athletes and assess mobility in elderly patients and those who recover from joint injuries.

Ambient sensors enhance WBANs' applications in healthcare, smart homes, and safety systems by monitoring the surrounding environmental factors that can affect human health, comfort, and safety. Humidity sensors measure the amount of water vapor in the air to optimize humidity levels for patients with respiratory conditions and ensure correct functioning of other wearables and electronic devices. Temperature sensors help to adjust performance in smart wearables or track body response based on ambient temperature. Light sensors measure the intensity of light in the environment to adjust the screen brightness on wearable devices, ensure optimal conditions for reading, or track light exposure, which is essential for sleep and well-being in health-monitoring systems. Gas sensors can detect harmful gas leaks and poor indoor air quality in smart homes.

1.2.3.2 Analog-to-digital converter (ADC) architectures

With the help of an ADC, the acquisition process transforms an analog signal, which is continuous in both time and amplitude, into a series of regularly sampled (at sampling period T_s), usually binary encoded, quantized values, i.e., a digital signal, which is discrete in both time and amplitude. The three main performance aspects of any ADC are speed, resolution, and power efficiency.

The ADC's speed is defined by its sampling frequency $F_s = 1/T_s$. The Shannon-Nyquist theorem states that F_s should be at least twice the highest frequency component F_{max} present in the signal to avoid aliasing, i.e., frequency components overlapping, and enable an accurate signal reconstruction. In specific type ADC architectures, such as sigma-delta ($\Sigma\Delta$), the signal is oversampled with the oversampling ratio (OSR). However, the highest allowed signal frequency is still defined by $F_{max} = F_{s,Nyq}/2$, where $F_{s,Nyq} = F_s/OSR$ represents the Nyquist sampling rate of an ADC.

The resolution of an ADC, n , expressed in bits, specifies the number of discrete digital levels 2^n that it can use to represent the input analog value. However, in addition to quantization error, the real circuit introduces noise and distortion while performing the conversion.

This reduces the effective resolution, which is called the effective number of bits (ENOB) and is expressed as follows:

$$ENOB = \frac{SNDR_{dB} - 1.76}{6.02} \quad \text{with } SNDR_{dB} = 10 \log_{10} \frac{P_S}{P_{N+D}}, \quad (1.1)$$

where SNDR stands for the Signal-to-Noise-and-Distortion Ratio, i.e., the ratio of the input signal power P_S to the power of all unwanted spectral components P_{N+D} , including the quantization noise, random noise, and distortion.

The Walden figure of merit (FoM_W) is often used to compare different ADCs in terms of power efficiency. This method relates the ADC's power consumption P to its speed and resolution performances, represented by the Nyquist sampling rate $F_{s,Nyq}$ and effective conversion error amplitude 2^{ENOB} :

$$FoM_W = \frac{P}{F_{s,Nyq} \cdot 2^{ENOB}} \quad (1.2)$$

When choosing an ADC, the characteristics of the acquired signal define the acceptable speed and resolution, while the application's energetic constraints define the acceptable power consumption. Hence, one or another ADC architecture is more suitable for a given application depending on these three performance aspects. Four principal architectures are successive-approximation register (SAR), pipeline, sigma-delta, and flash. Table 1.3 shows the most energy-efficient ADCs (those with the lowest Walden FoM values, i.e., the least energy per conversion), with one example per each of the four main architectures and some of their hybrids. The examples have been taken from B. Murmann's study [37], which regroups more than 700 publications on ADC design issued between 1997 and 2024. SAR ADCs are generally the most energy-efficient architecture. These ADCs are the most suitable for

TABLE 1.3 – Characteristics of ADCs

ADC architecture	Tech. (nm)	Area (mm ²)	Power (μW)	F _{s,Nyq} (MHz)	ENOB (bits)	FoM _W (fJ/c.)
SAR [27]	65	0.04	0.038	0.2	9.1	0.35
TDC-assisted SAR [28]	65	0.053	82	20	11.5	1.4
Pipelined-SAR [29]	22	0.037	360	50	12.5	1.8
SAR-assisted digital slope [30]	28	0.005	350	100	10.4	2.6
Pipeline [31]	7	0.024	7550	1800	9.7	5.0
SAR-assisted pipeline [32]	28	0.027	1260	50	12.2	5.5
Sigma-delta [33]	28	0.025	3200	80	12.6	6.5
Subranging (flash+pipel.) [34]	28	0.018	3000	2700	7.3	6.9
SAR-flash [35]	28	0.002	2550	1000	7.3	16.6
Flash [36]	32	0.02	8500	5000	4.8	59.3

WBANs, particularly their healthcare applications that require low conversion speed, medium resolution, and low power consumption.

1.2.3.3 Wireless transmitters

WBANs can employ various technologies and protocols for wireless intra- (sensor node \leftrightarrow coordinator/PD; coordinator \leftrightarrow PD) and inter-WBAN (PD \leftrightarrow access point) communications depending on range, latency, power consumption, and data rate requirements. Table 1.4 summarizes the performances of some transmitters implementing short- (up to 100 m) and ultra-short-range (less than 10 m) low-power wireless communication technologies fitting for these needs. Bluetooth Low Energy (BLE) and IEEE 802.15.6 standards are especially suitable for WBANs with healthcare and fitness applications.

Independent of classic Bluetooth [49], BLE is intended to operate with considerably reduced power consumption and cost but over similar distances (less than 100 m in line-of-sight conditions). It uses the same 2.402–2.480 GHz unlicensed industrial, scientific, and medical (ISM) frequency band but another set of channels (40 2-MHz wide channels) and a simpler modulation system. BLE supports point-to-point (star), broadcast, and mesh network

TABLE 1.4 – Characteristics of wireless transmitters

Wireless technology	Ref.	Tech. (nm)	Freq. (GHz)	Data rate (Mbit/s)	FoM (pJ/bit)	TX power (dBm)
BLE*	[38]	28			3700	0
	[39]	40	2.4	1	1550	-3
	[40]	40			490	-19
	[41]	65			1100	-10
	[42]	65			610	-8.4
802.15.4 (ZigBee)*	[42]	180	2.4	0.25	93000	-3
802.15.4z/4a (UWB)*	[43]	28	3-10	6.8	720	-2.5/-0.7
802.15.4a (UWB)*				27.24	16	
BFSK, wideband*	[44]	180	0.3	12.5	526	2.5
			1		1051	2.9
BFSK*	[45]	130	0.48	1	170	-20
				10	18	
802.15.6 (NB) [†]	[46]	130	2.4	0.971	1520	-9.5
802.15.6 (HBC) [†]	[47]	65	0.02227	1	20.6	not applic.
NB HBC [†]				10	2.24	
				[48]	0.020	

* Short-range † Ultra-short-range

topologies and allows 125 kbit/s, 500 kbit/s, 1 Mbit/s, and 2 Mbit/s data rates. According to Table 1.4, the most energy-efficient BLE transmitter [39] we found in the literature consumes 490 pJ per transmitted bit, though at a very low output power of -19 dBm (12.6 μ W).

The IEEE 802.15.6 standard is designed specifically for WBANs and primarily targets healthcare, facilitating even shorter range (less than 2 m) and lower power communication between wearables or implants and external devices. Generally, it uses a simple one-hop star network topology, establishing a direct link between sensor nodes and coordinator/PD. This standard supports three different configurations: Narrowband (NB), Ultra Wideband (UWB), and Human Body Communication (HBC).

NB comprises seven frequency bands: 402–405 MHz, 420–450 MHz, 863–870 MHz, 902–928 MHz, 950–958 MHz, 2360–2400 MHz, and 2400–2483.5 MHz. Depending on the modulation scheme, achievable data rates in NB configuration vary from 57.5 kbit/s to 971.4 kbit/s. UWB operating frequencies are divided into three and eight adjacent 499.2-MHz wide channels in low (3.245–4.742 GHz) and high (6.240–10.234 GHz) bands, respectively. This configuration enables data rates from 487 kbit/s to 15.6 Mbit/s. HBC relies on electric field communication technology, which uses the human body as a communication channel between transmitter and receiver by means of its dielectric properties. The devices in this configuration must transmit in the 21 MHz frequency band with data rates in the 164–1312.5 kbit/s range. In Table 1.4, the most energy-efficient IEEE 802.15.6 standard-compliant transmitter [47] belongs to the HBC category and requires 20.6 pJ/bit. To the best of our knowledge, the HBC transmitter with the lowest achieved FoM value (2.24 pJ/bit) was designed in the same publication. However, due to a high data rate (10 Mbit/s), this circuit does not comply with the standard.

1.2.4 Major constraints and challenges in WBANs

Depending on the application, sensor nodes composing WSNs should meet specific requirements, such as high reliability, compactness, affordability, and longevity. In contrast to other wireless networks, WBANs have more rigorous technical limits related to the deployment, mobility, and lifetime of sensor nodes, data storage, security, privacy, and quality of service [10]. The most crucial factors defining the WBANs' success are the system's lifespan and network throughput [9]. The sensor nodes' energetic efficiency and limited battery lifetime define the former. Effectively, the life duration of the entire WBAN shrinks if one of the nodes runs out of energy. At the same time, battery replacement and maintenance can be impossible or complicated, especially in implantable devices. The network throughput is also related to the power consumption since the high required data rate and, thus, throughput induce an increased energy usage due to transmission between sensor nodes and PDs. Hence, reducing the energy consumption of sensors and thus improving their autonomy in WBANs is one of the most critical and necessary tasks.

From Table 1.2, we notice that among all the listed biosensors, only two groups collect the corresponding time-varying signals continuously and require elevated sampling frequen-

cies and, consequently, data transmission rates: biopotential (ECG, EEG, and EMG) and inertial (accelerometers and gyroscopes) sensors from physiological and biokinetic categories, respectively. Since these sensors must perform frequent measurements and send large amounts of data, they tend to have power-hungry acquisition and transmission processes. Therefore, for the continuous functioning of WBANs employing biopotential and inertial sensors, it is important to optimize the energy usage in these sensors if possible. For this purpose, we could change how the corresponding signals are acquired and what data is transmitted afterward. However, not all applications involving biopotential and inertial sensors allow such modifications in the acquisition and transmission stages.

1.2.5 Energy-efficient approach for applications employing classification

In some applications, where anomalies or events are detected or classified, the processing is performed on the captured analog or digital signal to extract characteristic information from it, i.e., "features", which can then be used by classification or regression algorithms. The conventional wireless sensor approach implies that both feature extraction and classification are performed after receiving the samples sent from sensors at the aggregator level, as shown in the top half of Figure 1.2. In WBANs, a coordinator, a PD, or another device located further in the communication chain can serve as an aggregator. This approach with feature extraction at the aggregator implies that signals are acquired following the Shannon-Nyquist theorem, ensuring their complete information is preserved after converting into digital form. Hence, the ADC's sampling frequency must be at least two times higher than the maximum frequency component in the signal to obtain perfect signal reconstruction.

Due to a relatively high Nyquist rate, the transmission of all samples constitutes a significant part of the sensor's total consumption budget [50]. Effectively, even the most efficient wireless transmitter from Table 1.4 (narrowband HBC transmitter [47] with FoM = 2.24 pJ/bit) consumes almost 38 times more per one bit of sent information than the worst ADC in terms of energetic efficiency from Table 1.3 (flash ADC [36] with FoM = 59.3 fJ/conv)

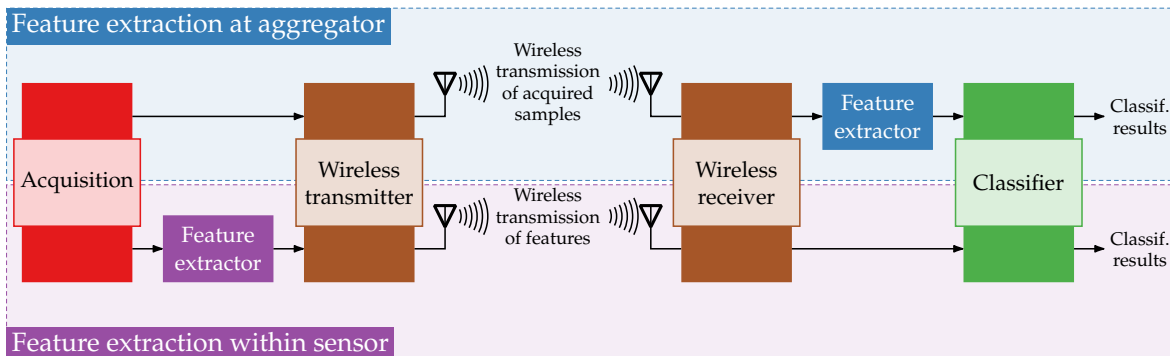


FIGURE 1.2 – Two approaches in wireless sensor networks with classification: feature extraction at aggregator or within sensor

performing a single step of analog-to-digital conversion. When only certain specific information contained in the signal is helpful for the classification task, this approach is energetically inefficient. Hence, in such cases, decreasing the consumption induced by the transmission process is possible by minimizing the volume of data transmitted from the sensor to the aggregator. One way to achieve this is to extract features directly within the sensor node (before or after digitization), as demonstrated in the bottom half of Figure 1.2. However, additional energy usage by feature extraction circuitry within the sensor must also be considered. Moreover, we can even carry out the classification on the sensor's side to further reduce transmission-related consumption.

1.2.6 Conclusion on WBANs

We have thus seen that WBANs are the primary solution for building new healthcare systems essential for reducing the effect of the inevitably rising rate of chronic diseases, the leading cause of human deaths, induced by population aging. The principal constraints imposed on these networks are their sensor nodes' limited battery lifetime and wireless network throughput. Diminishing the amount of acquired information and, thus, of transmitted data will decrease the energy usage and the required data rate. This point is especially relevant for two groups of biosensors, which capture their signals continuously: biopotential and inertial sensors. In the applications employing classification for anomalies or event detection based on the captured signals, the desired data volume reduction can be achieved through feature extraction performed right within the sensor node.

Moreover, WBANs are generally heterogeneous systems consisting of sensors of various types. Multimodal sensors or multi-sensor nodes, which measure different signals simultaneously or intermittently, can also be used in these networks. In some cases, multi-domain data infers more comprehensive information for classification purposes [51]. For example, physiological and ambient data is known to enhance the accuracy of human activity recognition (HAR) [52], which is traditionally accomplished using motion data from inertial sensors. Hence, of particular interest is developing a universal, generic solution that will provide less data for wireless transmission and be suitable for signals of different natures. In single-hop WBANs, such a solution would be helpful in the direct wireless communication between multimodal sensor nodes and PDs. In multi-hop WBANs, this solution would facilitate communication between multi-sensors and coordinator or between coordinator and PD, depending on the stage at which the feature extraction procedure is carried out.

In the next section, we conduct a comprehensive review of the literature on feature extraction and classification methods applied to biopotential and inertial sensor data, where this approach can bring significant benefit to WBANs in terms of energetic efficiency improvement due to the continuous nature of captured signals by reducing the volume of data that needs to be processed and transmitted. Specifically, we explore two applications: arrhythmia diagnosis in ECG signals and HAR in accelerometer and gyroscope signals.

1.3 Classification applied to biopotential and inertial signals

1.3.1 Introduction to classification with Machine Learning (ML)

The classification for anomalies or event detection is typically implemented by Machine Learning (ML) algorithms that take raw signals or features extracted from them as inputs. ML is a branch of Artificial Intelligence (AI) and computer science that enables machines to imitate intelligent human behavior and the way they learn and solve problems [53]. It applies statistical learning techniques and algorithms that identify patterns in data and improve automatically through experience [54] to make highly accurate predictions. In ML terms, a classification task consists of categorizing data points by attributing the same class or label to a group of observations with specific common characteristics. Among all types of ML models, supervised or unsupervised learning usually implements the classification process. Most datasets used in the literature for classification purposes based on biopotential and inertial signals provide the labeled data. Therefore, we study the workflow of supervised classification and the metrics for its performance evaluation.

1.3.1.1 Supervised classification workflow

Supervised classification is currently the most widely employed technique. As shown in Figure 1.3, its prediction models are configured and trained with labeled datasets in the form of (x_{train}, y_{train}) pairs, i.e., based on training observations x_{train} with known classes y_{train} . In contrast, unsupervised learning identifies patterns and relationships within unlabeled data. Owing to the lack of predefined classes and thus ground truth, it is challenging to measure the performance of unsupervised classifiers.

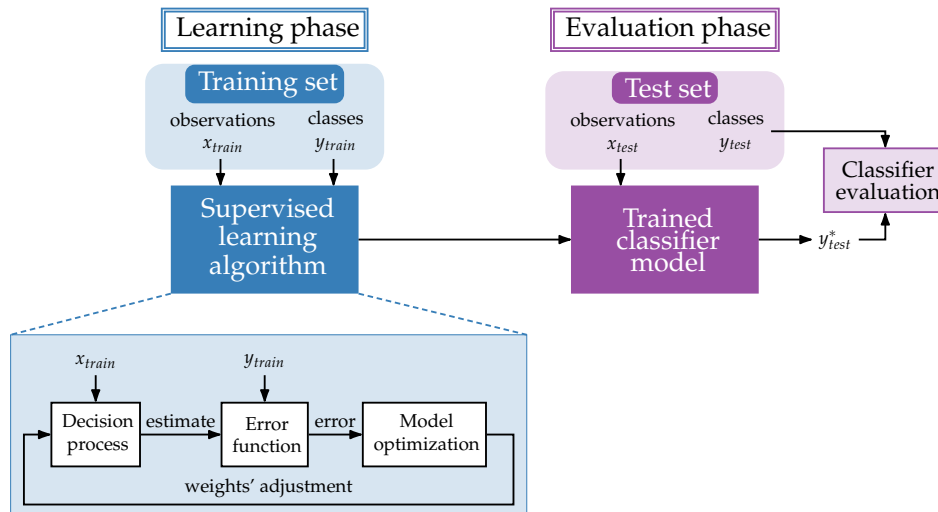


FIGURE 1.3 – Workflow of a supervised classification

The typical supervised learning algorithm comprises three main steps repeated iteratively [55]. First, a decision process produces an estimate about a pattern in the data. Then, an error function compares the model predictions to the known training classes y_{train} . Finally, a model optimization adjusts the weights to reduce the error between the estimates and training classes. The goal of a trained classifier is to predict the classes y_{test}^* of the test observations x_{test} . To evaluate the resulting classifier, we compare its predictions y_{test}^* to the true test classes y_{test} . The training and test sets need to be independent since the test set is used to determine if the classifier properly generalizes the training data.

1.3.1.2 Performance evaluation metrics

To evaluate the performance of the trained classifier on the test set, we use several different metrics depending on the type of classification – binary or multi-class. In particular, Figure 1.4 illustrates the confusion matrix of binary classification, where each classification result belongs to either of four possible outcomes: true positive (TP), false negative (FN), false positive (FP), and true negative (TN). TP , also called a hit, and TN , also called a correct rejection, define the correct predictions, i.e., those correctly indicating the presence or absence of a searched characteristic in the tested sample, respectively. Conversely, FN , also called a miss, and FP , also called a false alarm, represent wrong classification outcomes – false absence or presence of a given condition.

True class	Positive (P)	True Positive (TP)	False Negative (FN)
	Negative (N)	False Positive (FP)	True Negative (TN)
		Predicted Positive (PP)	Predicted Negative (PN)
		Predicted class	

FIGURE 1.4 – Binary confusion matrix

Based on these four notions, we can construct a multitude of different performance metrics. The most utilized are the following:

- Accuracy, which is calculated as the proportion of correctly classified instances among the total number of model predictions:

$$Accuracy^{binary} = \frac{TP + TN}{TP + TN + FP + FN} = \frac{TP + TN}{P + N} \quad (1.3)$$

- Sensitivity (recall), or a so-called true positive rate (TPR), which measures the classifier's ability to identify true positives. Mathematically, it corresponds to the proportion

of correctly classified positive instances to the total number of positive observations (P):

$$Sensitivity^{binary} = \frac{TP}{P} = \frac{TP}{TP + FN} \quad (1.4)$$

- Specificity (selectivity), or a so-called true negative rate (TNR), which shows how well the classifier identifies true negatives. It is thus calculated as the proportion of correctly classified negative instances to the total number of negative observations (N):

$$Specificity^{binary} = \frac{TN}{N} = \frac{TN}{TN + FP} \quad (1.5)$$

As demonstrated in Figure 1.5a, in addition to sensitivity (TPR) and specificity (TNR), we can derive two more metrics relative to true class (condition), namely, false negative rate (FNR , type II error) and false positive rate (FPR , type I error). Moreover, in a similar way, by relating the four possible classification outcomes to the classes predicted positive ($PP = TP + FP$) and predicted negative ($PN = TN + FN$), we obtain such supplementary metrics shown in Figure 1.5b as positive predictive value (PPV , precision), false omission rate (FOR), false discovery rate (FDR), and negative predictive value (NPV).

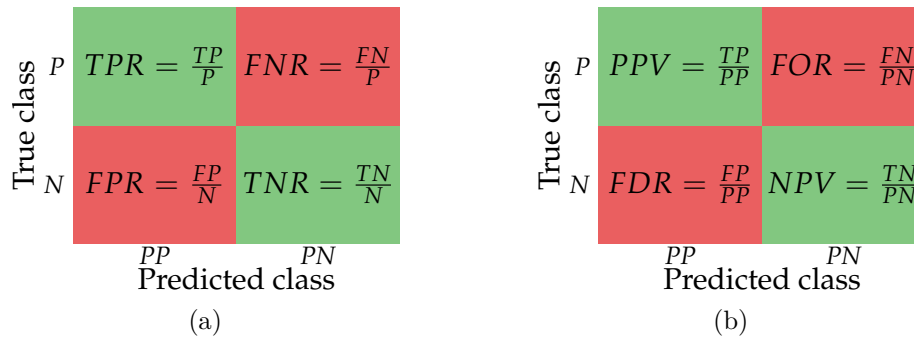


FIGURE 1.5 – Binary classification metrics relative to (a) true and (b) predicted classes

Despite its straightforward interpretation, accuracy is not an ideal metric for all binary classification problems. It estimates the overall performance of the classification model, disregarding the class balance. Since some class might be more prevalent ($P \gg N$ or $P \ll N$), the classifier might categorize the instances belonging to this class much easier. The high accuracy value produced in this case might be misleading as it does not reveal the classifier's ability to identify minority class observations. Hence, it is practical to supplement accuracy with sensitivity and specificity for a more detailed evaluation in classification problems with a predominant class. Alternatively, we can resort to using the Matthews correlation coefficient (MCC), a metric first introduced in biochemistry [56]. Although it also estimates the overall classifier performance, the MCC is more informative than accuracy in evaluating binary classification problems with imbalanced datasets [57] since it accounts more thoroughly for the

size of all four categories in the confusion matrix:

$$MCC^{binary} = \frac{TP \cdot TN - FP \cdot FN}{\sqrt{(TP + FN)(TN + FP)(TP + FP)(TN + FN)}} \quad (1.6)$$

The MCC takes values in $[-1; +1]$ interval: $MCC = -1$ corresponds to the case of totally wrong predictions, $MCC = 0$ means that predictions are random or uncorrelated with the true classes, and it becomes $+1$ when the model perfectly classifies all instances. An alternative way to express the MCC shows that its high score always corresponds to having high values of all four basic binary confusion matrix metrics, i.e., TPR , TNR , PPV , and NPV [58, 59]:

$$MCC^{binary} = \sqrt{TPR \cdot TNR \cdot PPV \cdot NPV} - \sqrt{FPR \cdot FNR \cdot FDR \cdot FOR} \quad (1.7)$$

In multi-class classification, each instance belongs to a single class from more than two (N_C) predefined classes. Thus, there are no notions of positive and negative observations. Nevertheless, we can extend the definition of several metrics mentioned above for binary classification to the multi-class case:

- Accuracy, which measures the ratio between the number of correct predictions $N_{pred}^{correct}$ and their total number $N_{pred}^{correct} + N_{pred}^{false}$ in a similar manner to binary classification. For a given class i , we can treat this class as positive and all others as a single negative. Hence, $N_{pred}^{correct}$ can be expressed as the sum of true positives and N_{pred}^{false} as the sum of false positives or negatives:

$$Accuracy^{multi} = \frac{N_{pred}^{correct}}{N_{pred}^{correct} + N_{pred}^{false}} = \frac{\sum_{i=1}^{N_C} TP_i}{\sum_{i=1}^{N_C} (TP_i + FN_i)} = \frac{\sum_{i=1}^{N_C} TP_i}{\sum_{i=1}^{N_C} (TP_i + FP_i)} \quad (1.8)$$

- Recall and precision, measured for each class individually. To calculate them, again, we treat the specific class i as positive and all others as a single negative class:

$$Recall_i^{multi} = \frac{TP_i}{TP_i + FN_i} \quad (1.9a)$$

$$Precision_i^{multi} = \frac{TP_i}{TP_i + FP_i} \quad (1.9b)$$

- Macro-averaged recall and precision, which attribute equal weight to each class. Such metrics are calculated by taking the arithmetic mean across the corresponding individual metrics of all N_C classes:

$$Recall_{macro}^{multi} = \frac{\sum_{i=1}^{N_C} Recall_i}{N_C} \quad (1.10a)$$

$$Precision_{macro}^{multi} = \frac{\sum_{i=1}^{N_C} Precision_i}{N_C} \quad (1.10b)$$

- Micro-averaged recall and precision, which attribute equal weight to each instance. To calculate these metrics, we use the sums of TPs , FNs , and FPs across all classes. Since total FNs and FPs are equal and represent the total number of false predictions in multi-class classification, such calculations result in the same value for two metrics, which are also nothing other than accuracy:

$$Recall_{micro}^{multi} = \frac{\sum_{i=1}^{N_C} TP_i}{\sum_{i=1}^{N_C} (TP_i + FN_i)} = Accuracy^{multi} \quad (1.11a)$$

$$Precision_{micro}^{multi} = \frac{\sum_{i=1}^{N_C} TP_i}{\sum_{i=1}^{N_C} (TP_i + FP_i)} = Accuracy^{multi} \quad (1.11b)$$

For a large number of classes, macro- and micro-averaging provide a more concise overall performance summary in multi-class classification. Macro-averaged recall and precision treat each class as equally important and show average performance across classes. In contrast, accuracy (micro-averaging) gives equal weight to every observation and provides average performance across all predictions. However, just as in the binary case, it disregards class balance and, thus, recall and precision by class can provide more detailed information for each class.

1.3.2 Arrhythmia diagnosis in electrocardiogram (ECG) signals

As mentioned in Section 1.1, cardiovascular diseases (CVDs) are responsible for almost half of human deaths caused by NCDs and for one-third of them in total. In particular, arrhythmias, also known as cardiac arrhythmias or irregular heartbeats, are one of the most common types of CVDs [60]. It is a group of heartbeat deviations from a normal sinus rhythm when the heart beats irregularly or at an abnormal pace due to disturbances in its electrical conduction system [61]. While most arrhythmia types are not severe for well-being, some of them, if not treated in time, can irreversibly damage the heart and other organs, lead to life-threatening complications such as stroke and heart failure, or even result in sudden death because of cardiac arrest [62]. Hence, it is of utmost importance to develop real-time, automatic systems for abnormal heartbeat detection, which will save people's lives and improve healthcare efficiency.

The guideline of the ANSI/AAMI (American National Standards Institute/Association for the Advancement of Medical Instrumentation) EC57 standard [63] defined five categories and 15 classes of heartbeats, as shown in Table 1.5. Some studies differentiate heartbeats according to their main category as recommended by the ANSI/AAMI EC57 standard to classify arrhythmia. In contrast, others address per-class classification to identify the exact type of corresponding beat.

TABLE 1.5 – Heartbeat classification as per the ANSI/AAMI EC57 standard

Category	Class (annotation)
N	• Normal (N) • Left and right bundle branch blocks (L and R) • Atrial escape (e) • Nodal (junctional) escape (j)
S	• Atrial premature (A) • Aberrant atrial premature (a) • Nodal (junctional) premature (J) • Supraventricular premature (S)
V	• Premature ventricular contraction (V) • Ventricular escape (E)
F	• Fusion of ventricular and normal (F)
Q	• Paced (/) • Fusion of paced and normal (f) • Unclassifiable (Q)

1.3.2.1 Introduction to ECG recordings

The most widespread test that helps to diagnose abnormal/arrhythmic heartbeats is an ECG, which measures the electrical activity responsible for the heart's contractions and relaxations by placing several electrodes on the skin's surface. In conventional healthcare clinical practice, cardiac activity data is usually collected in either of two formats: a short-term recording by a standard 12-lead ECG or a long-term recording up to several hours by a 5-7-lead Holter ECG [64]. However, a medical professional needs to examine the results obtained this way, which can be too late or even impossible in urgent cases.

Therefore, lightweight, low-power, wearable ECG sensing and processing systems implemented in the frame of WBANs could facilitate autonomous, fast anomaly detection. Such wireless ECG body sensors, like, e.g., the one developed in [65] and intended for long-term use, perform single-lead monitoring, allow a broader range of applications than CVD diagnostics, and are often multi-functional devices owing to additional functions aboard. Nevertheless, to remain energy-efficient and low-cost, these devices must overcome the challenges in data collection, processing, and analysis. In particular, continuous recording creates a large amount of data, which has to be acquired and transmitted more effectively or analyzed immediately within the sensor node with the help of efficient computational algorithms.

As shown in Figure 1.6, five specific waves named by letter constitute a PQRST complex and compose one heartbeat or cardiac cycle. Certain waves' onset, offset, and peak locations represent fiducial points. They can serve for measuring such important aspects in ECG signals for anomaly detection or arrhythmia diagnosis as the R-R interval (cardiac rhythm), QRS complex duration, P-R, S-T, and Q-T intervals, as well as PR and ST segments.

Usually, the process of arrhythmia diagnosis in ECG signals consists of four main consecutive steps: data collection, preprocessing, feature engineering (extraction and selection), and heartbeat classification [66, 67].

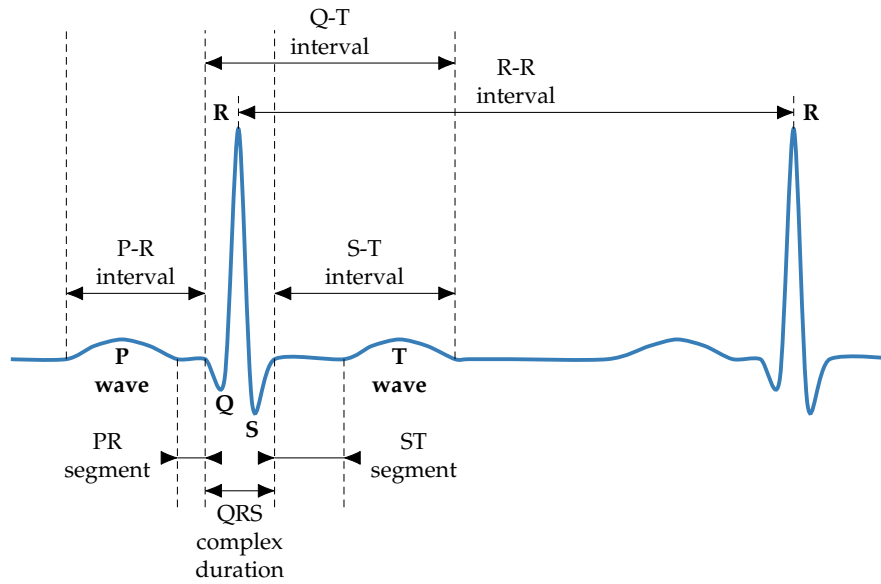


FIGURE 1.6 – ECG waveform with indicated PQRST complex, intervals, and segments

1.3.2.2 Data collection

There are plenty of publicly available datasets containing ECG recordings collected from multiple patients and supplied with beat and non-beat annotations marking different cardiac events used in literature to detect CVDs. The overwhelming majority of studies exploit the Massachusetts Institute of Technology-Boston’s Beth Israel Hospital (MIT-BIH) Arrhythmia Database (MITDB) [68] from the PhysioNet repository to prove the validity of their models performing arrhythmia diagnosis. Hence, in the following sections, we review the literature on the preprocessing techniques, the types of extracted features (if any), classification methods, and obtained performances when applied to this dataset.

1.3.2.3 Preprocessing

Table 1.6 summarizes the preprocessing methods used in recent studies performing arrhythmia diagnosis. These include denoising, segmentation, normalization, data augmentation, dimensionality reduction, and detection and marking of fiducial points and aspects.

The ECG recording process is susceptible to various kinds of noise. Conventional noise removal methods apply bandpass filters and maintain only the frequency range of interest [66]. However, predominant noises and artifacts, such as baseline wander, power-line interference, and muscle artifacts, manifest inside this frequency range. They may look similar to inherent aspects of ECG or aspects specific to CVDs [89] and thus hinder their correct detection.

Baseline wander represents a low-frequency (0.05–1 Hz) artifact with a wide range of possible amplitudes and durations, mainly caused by body movements, respiration, and poor electrode contact. Power-line interference is a narrowband noise centered at 50/60 Hz with up to half of peak-to-peak ECG signal amplitude due to inductive and capacitive couplings

TABLE 1.6 – Input ECG data and preprocessing methods in studies performing arrhythmia diagnosis in ECG recordings from the MITDB

		not reported [69–79]	
Input ECG data (number of leads)		one (MLII* in most records) [80–85]	
		two (MLII*, V1 [†] in most records) [86–88]	
Preproc. methods	Noise removal	[70–76, 78, 84, 88]	
	Segmentation	[69, 70, 72–80, 82–85, 87]	
	Normalization	[70, 81, 82, 85, 87, 88]	
	Data augmentation	[78, 88]	
	Dimensionality reduction	PCA [86]	
	Detection and marking		R-peak (Pan-Tompkins algorithm) [74, 75, 78]
			peaks (Pan-Tompkins algorithm) [84]
		QRS (Pan-Tompkins algorithm) [73, 85]	

* Modified limb lead II † Modified lead V1

of power lines. Muscle artifacts or EMG noise originate from the electrical activity of muscles near the head due to intended or sudden body movements, lasting around 50 ms, and characterized by high frequencies (> 20 Hz) and amplitudes around 10% of peak-to-peak ECG signal amplitude. Besides bandpass filters, traditional denoising employs low-pass and notch filters, assuming that useful signal and noise occupy separable frequency bands. Despite their more straightforward implementation, traditional filter-based methods may be inefficient in removing predominant noises and thus are more often replaced by wavelet-based methods or combined with them [90]. Nevertheless, we omit the discussion of denoising techniques in detail since this topic is beyond the scope of this thesis.

Segmentation divides the ECG recording into analysis windows for further processing. Most of the studies retrieved separate heartbeats to perform beat-by-beat classification. Some studies applied sliding window techniques to the entire ECG signal, possibly leading to different numbers of heartbeats in windows [91]. Segmentation usually centers the windows around the detected R-peaks or QRS complexes, but it can also rely on the detection of T-T intervals, as in [84]. The Pan-Tompkins algorithm is widely used to detect QRS complexes and different peaks with high accuracy, albeit faster and simpler algorithms can provide comparable detection results [64]. Data normalization, mainly implemented as min-max or Z-score normalization, performs signal rescaling to standardize the amplitude and may even speed up the convergence rate in the learning process [67]. To improve the learning performance, some papers use data augmentation techniques, which help to deal better with imbalanced datasets, including MITDB, that have much more normal heartbeats than those with anomalies [90]. Perturbation-based data augmentation methods add extra samples by adjusting or perturbing the original dataset’s samples. In contrast, synthetic-based methods gener-

ate new synthetic data through a linear combination of original samples or imitation of real ECG signals. For example, the synthetic minority oversampling technique (SMOTE) [92] is frequently used for the extension of minority categories or classes [93]. Additionally, the dimensionality reduction techniques, such as Principal Component Analysis (PCA) applied in [86], can reduce the space dimensions of features after their extraction.

1.3.2.4 Feature engineering

Feature engineering involves the extraction and selection of specific features from ECG waveforms. However, due to the increasing popularity of Deep Learning (DL) methods, many recent studies fed raw signals in the form of digital samples from the MITDB recordings to the classification model's input. Thus, they implemented an end-to-end structure that performs extraction, selection of features, and classification in a single stage. Other studies relied on independent from other learning stages extraction of diverse hand-crafted features that are related to space, frequency, time, or time-frequency domains or are non-linear. Table 1.7 summarizes the hand-crafted extraction methods and derived features in recent studies performing arrhythmia diagnosis.

The most widely employed technique from traditional signal processing proposed for feature extraction is Discrete Wavelet Transform (DWT) and its variations. It can be used separately as in [86], or in combination with PCA [73, 75, 83], with PCA and Linear Discriminant Analysis (LDA) [71], or with Independent Component Analysis (ICA) [72] to obtain features in frequency or time-frequency domains. Authors in [86] also extracted phase angle and power spectrum from the Fast Fourier Transform (FFT). The combination of Higher-Order Spectra (HOS) and ICA allowed obtaining 16 additional non-linear cumulants in [73]. After signal optimization through PCA to reduce ECG data dimensions, Kernel-Independent Component Analysis (KICA) with Radial Basis Function (RBF) kernel derived 20 non-linear features in [71].

Authors in [74] performed a sparse decomposition of ECG signals into stationary and non-stationary atoms using a composite dictionary composed of multiple analytical functions. The set of features extracted from these atoms consisted of R-R intervals, energy, standard deviation (SD), kurtosis, and permutation entropy. In [76], the Empirical Mode Decomposition (EMD) algorithm decomposed segmented heartbeats into Intrinsic Mode Functions (IMFs), which are amplitude- and frequency-modulated functions. Four non-linear features, i.e., sample entropy, coefficient of variation, singular values, and band power, were calculated from each of the first five IMFs.

Two studies employed personalized DL techniques of feature extraction. In [80], a 16-layer deep Convolutional Auto-Encoder (CAE) compressed original 260 samples long input signals into feature vectors of size 32 with minimum loss, ensuring feasible reconstruction. To benefit from the correlation of multi-lead ECGs, authors in [87] extracted abstract discriminating features from two leads simultaneously through a dual-lead canonical correlation analysis

TABLE 1.7 – Hand-crafted features extracted in studies performing arrhythmia diagnosis in ECG recordings from the MITDB

Ref.	Input data/ extract. approach	Feature domain	Extracted features
[86]	R-R interval, DWT, FFT	space	amplitudes: • avg., • variance, • R-wave; voltage values: • lowest, • highest
		frequency	DWT: • frequency; FFT: • phase angle, • power spectrum
[74]	sparse decomposition	time	R-R intervals: • skewness, • kurtosis • R-R intervals; • energy; • kurtosis; • SD;
		non-linear	• permutation entropy
[72]	R-R interval	time	intervals: • R-R, • local R-R, • avg. R-R
	Teager energy operator		• energy
[75]	DWT+ICA		
[75]	DWT+PCA		
[83]	biorthogonal 6.8 wavelet multires. analysis+PCA	time-freq.	12 coefficients
[73]	DWT+PCA		
[73]	HOS cumulants+ICA		16 cumulants
[76]	IMFs decomposition with EMD	non-linear	• sample entropy, • coefficient of variation, • singular values, • band power
[71]	PCA+KICA		20 independent base signals
[71]	DWT+PCA+LDA	frequency	wavelet coeff.: • mean, • min, • max, • SD
[80]	raw signal		deep-coded by CAE
[87]			extracted by DL-CCANet

network (DL-CCANet). CCANet represents a combination of canonical correlation analysis and cascaded convolution network and extracts features with high dimensionality and sparsity.

Feature extraction plays a crucial role in enhancing the interpretability of ML models by allowing a clear definition of their features. On the other hand, embedding feature extraction directly within DL models helps save resources and time during the learning process.

1.3.2.5 Classification

The last stage in the arrhythmia diagnosis pipeline is ECG heartbeat classification. Authors in [73, 75, 77, 78, 84] classified the heartbeats based on their category (N, S, V, F, or Q) following the ANSI/AAMI EC57 standard’s recommendations for arrhythmia classification. In [85], the category Q with the least number of examples present in the MITDB has been excluded from training and test sets. However, the majority of studies in literature performed per-class heartbeat classification between multiple classes that occur the most in the MITDB, with N, L, R, A, and V being the most frequently used classes for this purpose. Table 1.8

summarizes the applied classification methods and achieved performances in recent works on arrhythmia diagnosis. Almost all examples used macro-averaging for their accuracy, sensitivity, and specificity metrics to show average performance across classes, thus treating all available classes as equally important.

Two DL techniques, Convolutional Neural Network (CNN) and Long Short-Term Memory (LSTM), are the leading classification methods applied in this field. Both spatial and temporal features are essential in arrhythmia diagnosis. CNNs are excellent at capturing local, spatial features by applying convolutional filters to detect characteristic patterns crucial for arrhythmia identification, such as peaks, waves, and amplitude changes. LSTMs are designed to model long-term dependencies in sequential data, retain historical information over long sequences, and learn temporal patterns. Since ECG recordings represent time-series data, LSTMs are effective in arrhythmia diagnosis, which often depends on the timing and relationships between successive heartbeats. Hybrid models combine CNN and LSTM architectures and leverage the strengths of both techniques.

TABLE 1.8 – Classification methods and performances in studies performing arrhythmia diagnosis in ECG recordings from the MITDB

Categories/ classes	Ref.	Classifier/ prediction method	Average performance metrics (%)		
			Accuracy	Sensitivity	Specificity
Categories: N,S,V,F,Q	[84]	CNN (intra-patient)	99.81	88.82	99.54
		CNN (inter-patient)	96.36	70.60	96.16
	[75]	KNN-SVM	99.78	92.56	99.53
	[78]	ResNet-BiLSTM-Attention	99.4	98.4	99.3
	[77]	CNN-LSTM	99.3	99.33	—
	[73]	SVM	98.91	98.91	97.85
		Feedforward NN	98.90	98.90	98.90
Ctg.: N,S,V,F	[85]	Transformer-based CNN	99.49	92.51	99.84
18 classes	[72]	Feedforward NN	99.75	98.7	99.9
16 classes	[74]	ABC-DAG-LSTSVM	99.21	99.21	—
15 classes	[87]	SVM	99.4	94.6	99.6
13 classes	[81]	1-D CNN	95.2	93.52	99.61
N,L,R,e,j,A,a,J	[70]	LSTM with focal loss	99.26	99.26	99.14
N,L,R,A,V,E,v*,/	[85]	Transformer-based CNN	99.12	97.53	99.83
N,L,R,A,V,/	[83]	One-vs-one SVM	99.70	99.82	99.82
	[86]	Cascaded: RF-MLP	99.3	99.3	—
N,L,R,A,V	[88]	CNN-LSTM	99.35	98.37	99.59
	[80]	LSTM	99.23	99.0	—
	[76]	SMO-SVM	99.2	98.01	99.49
	[71]	SVM-GA	98.8	98.50	99.69
	[82]	CNN-LSTM w/o dropout	98.42	98.07	98.76
N,L,R,V,/	[69]	DBLSTM-WS	99.39	100	—
N,V	[79]	CNN-improved BiGRU	97.9	98	97.8

* Ventricular flutter wave

CNN was used separately in [81, 84, 85] and in combination with LSTM in [77, 82, 88]. Authors in [79] embedded an improved bidirectional Gated Recurrent Unit (BiGRU) model alleviating the information redundancy issue into a CNN architecture for premature ventricular contraction (class V, see Table 1.5) detection. In [80], LSTM carried out the classification based on previously extracted features deeply coded with the CAE network. While LSTM automatically extracted timing features, the focal loss mitigated the imbalanced class distribution to distinguish the heartbeats belonging to eight classes in [70]. The approach proposed in [69] used a deep bidirectional LSTM network with wavelet sequences (DBLSTM-WS), where ECG signals decomposed into frequency sub-bands in a wavelet-based layer served as inputs for the LSTM network. An effective fusion of spatial and temporal information from residual convolutional blocks (ResNet) and bidirectional LSTM (BiLSTM) with feature enhancement through the Attention mechanism was demonstrated in [78].

However, DL methods usually require intensive computational resources for high classification performance. In the absence of such resources, Support Vector Machines (SVMs) can be a good alternative for arrhythmia diagnosis in ECG signals if provided with relevant hand-crafted features by the preceding extraction stage, which can be a lengthy process. In [83], a one-vs-one SVM was implemented using RBF with the Gaussian kernel and used a majority voting for a multi-class classification. Linear SVM classified heartbeats into 15 classes based on features with high dimensionality and sparsity extracted by DL-CCANet in [87]. Authors in [74] employed a least square twin SVM (LSTSVM) classifier with a directed acyclic graph (DAG) recognition scheme and artificial bee colony (ABC) technique for the classifier's parameters' tuning. In [71], an SVM classifier was optimized with a genetic algorithm (GA). The features obtained from the EMD decomposition in [76] were independently fed to the sequential minimal optimization-SVM (SMO-SVM) for classification between five classes. SMO-SVM represents an improved SVM algorithm whose advantage lies in handling large training data sets analytically in a shorter time.

Authors in [75] employed a hybrid model composed of the K-Nearest Neighbours (KNN) and SVM classifiers. SVM and feedforward NN classifiers with the same input feature set obtained similar performances in [73]. The NN contained an input layer of 28 nodes (12 time-frequency domain and 16 non-linear features), a hidden layer of 40 neurons, and an output layer of five neurons to distinguish five heartbeat categories. In [72], a feedforward NN with ten hidden layers was used to classify between 18 classes. Authors in [86] utilized a cascaded classifier based on a Random Forest (RF) and a multi-layer perceptron (MLP, a particular case of a feedforward NN with fully connected layers) with five hidden layers.

All considered ML and DL classifiers achieve average accuracy values of more than 95%, though often requiring numerous input features or significant computational resources, making them complex or impossible to embed in WBANs.

1.3.3 Human activity recognition in inertial signals

HAR aims to identify various human activities by analyzing raw sensor data, images, or video sequences that capture the human body's movements and poses [94]. Typical recognized activities are the so-called body-level activities. They are mainly caused by the torso's movement and include such basic body movements as sitting, standing, walking, jogging, going up or down stairs, falling, etc. The evolution of IoT has recently enabled the deployment of numerous ubiquitous mobile and wearable devices with built-in sensors and embedded computing capabilities. The rapid progress of wearable technologies and advancements in ML and DL algorithms have spurred the growth of sensor-based HAR, which emerged as a highly explored research topic. Inertial sensors, which provide researchers with collections of unprocessed biokinetic signals suitable for analyzing human activities, remain the most frequently adopted type of sensors for this purpose [95]. Driven by the growing demand for diverse human-centric applications, HAR can significantly contribute to continuous remote healthcare, sports tracking, and smart home systems [96]. In particular, HAR is a promising technology for assisting elderly people in daily life through physical and mental health monitoring, detecting and preventing falls in real-time and in a non-intrusive way [97].

Similarly to arrhythmia diagnosis in ECG signals, inertial sensors-based HAR systems perform four principal consecutive steps: data collection, preprocessing, feature engineering (extraction and selection), and classification. However, one may require an additional preprocessing operation that separates the body and gravitational acceleration [98].

1.3.3.1 Data collection

Among multiple publicly available datasets for HAR applications that adopt motion sensors, the UCI-HAR dataset [99] is the most exploited. It provides the sensor data corresponding to six daily activities collected from three-axial accelerometers and gyroscopes embedded in a smartphone. Hence, in the following sections, we briefly review the literature on the preprocessing techniques, the types of extracted features, classification methods, and obtained performances when applied to this dataset.

1.3.3.2 Preprocessing

Since inertial-sensor-based signals are times-series data like ECG signals, specific preprocessing methods discussed in Section 1.3.2.3 for arrhythmia diagnosis are relevant for HAR.

Denosing mitigates the noise in sensor data caused, e.g., by sensor hardware imperfections, power supply and temperature variations, mechanical vibrations, and environmental magnetic interference. The UCI-HAR dataset's signals already underwent preprocessing with a median filter and a third-order Butterworth low-pass filter. Nevertheless, other types of filters, wavelet-based methods, PCA, and ICA, were applied in the literature for noise removal in inertial sensor-based datasets [100].

The UCI-HAR dataset provides recordings initially segmented into fixed-size sliding analysis windows with a 50% overlap between adjacent segments. Besides the sliding window technique, studies utilizing other datasets employ peak and valley point detection, thresholding, and crossing correlations for data segmentation [100]. Data normalization for signal rescaling and amplitude standardization is also a crucial preprocessing step, especially for ML-based classification methods. Even though all six classes in the UCI-HAR dataset are relatively balanced, some papers apply data augmentation techniques such as the SMOTE and its variations to increase the number of samples in minority classes [94].

1.3.3.3 Feature engineering

The three primary feature extraction and selection approaches are classical hand-crafted features, automatic feature generation through DL methods, and their hybrid.

The UCI-HAR dataset provides its own hand-crafted features alongside the inertial signals captured from the smartphone-embedded accelerometer and gyroscope. First, besides these denoised signals, it contains body acceleration signals produced from the original ones using another Butterworth LPF. Moreover, two additional three-dimensional jerk signals were obtained from the time derivative of three-axial body linear acceleration and angular velocity signals. Then, the magnitude signals were calculated from all five three-axial signals via the Euclidean norm, and the FFT was applied to some of these signals and their magnitudes. Finally, the resulting signals – ten in time and 17 in the frequency domain – served to extract a vector of 561 features within each data segment, i.e., the analysis window. Studies employing traditional ML algorithms for HAR based on this or other datasets often train their classifiers on features that are already available in the UCI-HAR dataset or are similar to them. Table 1.9 lists these features applied to time- and frequency-domain signals.

TABLE 1.9 – Features extracted from signals in the UCI-HAR dataset

Signal domain	Extracted features
Time	<ul style="list-style-type: none"> • autoregression coefficients • angle between two vectors • correlation coefficient between two signals
Frequency	<ul style="list-style-type: none"> • index of the frequency component with the largest magnitude • frequency components' weighted average to obtain a mean frequency • skewness • kurtosis • energy within a given frequency band
Time or frequency	<ul style="list-style-type: none"> • mean value • standard deviation • median absolute deviation • maximum value • minimum value • signal magnitude area • energy (mean of squares) • interquartile range • signal entropy

1.3.3.4 Classification

Table 1.10 outlines the applied classification methods and achieved prediction accuracies in recent HAR studies that evaluated their classifiers with the UCI-HAR dataset. Most of

the examined works utilized both types of inertial signals, i.e., linear acceleration and angular velocity, for feature extraction and model training. Nonetheless, authors in [101,102] managed to obtain state-of-the-art classification performances using exclusively recordings from the accelerometer. In [101], a shallow CNN performing unsupervised local feature extraction was augmented with statistical features that preserved important information about the global form of time-series acceleration signals. These statistical features included mean, variance, sum of the absolute values, and the histogram for each signal’s axis.

Some studies trained their classifiers on features initially calculated in the UCI-HAR dataset. In [94], the entire set of 561 features served as input for the DL classification model. Meanwhile, the most performant traditional ML classifier of [94] used 100 features chosen by the Truncated singular value decomposition (TSVD), the dimensionality reduction mechanism similar to PCA. Authors in [105] reduced the number of features fed to the classification al-

TABLE 1.10 – Classification methods and performances in studies performing HAR in inertial signals from the UCI-HAR dataset

Used signals	Ref.	Input data/ extracted features	Classifier/ prediction method	Accuracy (%)
A*	[101]	raw signals + statistical features	CNN	97.63
	[102]	raw signals	CNN with SK convolution	97.21
	[94]	561 [‡] features	1-D CNN	100
		100 selected by TSVD	LGBM	
	[103]	CWT → Attention-CNN → GA	KNN	99.45
	[104]	raw signals	4-layer CNN-LSTM	99.39
	[105]	66 features out of 561 [‡] after FFDRT selection	RF	98.72
			KNN	98.45
	[106]	spectra from WT	binarized NN	98.2
	[107]	raw signals	CNN-RF	98.2
CNN-LSTM			97	
CNN-GRU			96.7	
[108]	signals + FFT → HGD and FD	SVM	97.12	
A*, G [†]	[109]	raw signals	CNN with local loss	96.98
	[110]		CNN with C3	96.98
	[111]	561 [‡] features + FFT	Cascade ensemble learning	96.88
	[112]	raw signals + 561 [‡] features	Ensemble learning	96.7
	[113]		CNN-GRU	96.67
	[114]		CNN-BiLSTM	96.37
	[115]		CNN-GRU	96.2
	[116]		8-layer LSTM-CNN	95.78
	[117]	raw signals	3-head CNN with Attention	95.38
			iSPLInception	95.09
[118]		CNN-LSTM	94.48	
		BiLSTM	93.91	
[119]		Deep Residual BiLSTM	93.6	

* Accelerometer † Gyroscope ‡ calculated in the UCI-HAR dataset

gorithms to 66 through a so-called fast feature dimensionality reduction technique (FFDRT). In [111], the complete feature set was supplemented with the input signals' FFT components. The classification model in [112] received at its input all raw signals and features available in the UCI-HAR dataset.

Three reviewed studies extracted other hand-crafted features. Authors in [103] first encoded the raw sensor time-series data into an image form using a one-dimensional Continuous Wavelet Transform (CWT), then extracted high-dimensional features by an Attention-aided CNN and applied a modified version of the GA to maintain only relevant features. The time-frequency spectra produced by the CWT from each axis of both inertial sensors were superimposed and fed to the input of the classification model in [106]. In [108], a histogram of gradient and the Fourier descriptor (HGD, FD) performed the feature extraction from eight time-domain signals – both three-axial acceleration and angular velocity with their magnitude signals – and their FFT's magnitude signals. In the remaining studies from Table 1.10, raw time-series data from the accelerometer and gyroscope served as input for trained classifiers.

Even though traditional ML methods have already achieved significant success in HAR, the DL techniques, which obviate the need for hand-crafted feature extraction, have taken the lead in this research field. Indeed, given that inertial sensors provide time-series data similar to ECG recordings, the same conclusion as for arrhythmia diagnosis applies here – both CNN and LSTM are effective tools for the HAR, while hybrid models combine their strengths.

Apart from the previously discussed work [101], several variations of a separate use of CNN can be found in the literature. Thus, in [102], the Attention mechanism assists a multi-branch CNN to perform a selective kernel (SK) convolution. CNN and Light Gradient Boosting Machine (LGBM) models reported in [94] showed the best classification performances on the UCI-HAR dataset among all DL and traditional ML algorithms, respectively. Authors in [109] proposed a more stable and memory-efficient layer-wise CNN training process with a local loss. In [110], cross-channel communication (C3) in the same layer helps remove redundant information accumulated among channels and capture more discriminative features. The Attention mechanism assigns higher weights to more relevant features for a three-head CNN described in [117]. CNN and LSTM (uni- and bidirectional) networks were used combined in [104, 107, 114, 116, 118]. Authors in [112] proposed an Ensemble learning algorithm, which effectively combines a GRU (Gated Recurrent Unit), a CNN stacked on the GRU, and a deep NN. A hybrid CNN-GRU classifier was also implemented in [107, 113, 115]. Meanwhile, a separate BiLSTM [118] or a residual BiLSTM [119], whose residual connections between stacked cells help prevent the gradient disappearing issue, do not offer state-of-the-art performance. The intelligent signal processing lab Inception (iSPLInception) model [118], inspired by the DL Inception-ResNet architecture from Google, achieved higher classification accuracy than BiLSTM and CNN-LSTM models demonstrated in the same study.

When provided with highly relevant hand-crafted features, traditional ML methods can obtain leading-edge performance levels and be an excellent alternative solution to DL algorithms

in the absence of high-end computing power typically required for their implementation. The recent examples are KNN and RF presented in [103, 105]. Authors in [106] built a binarized NN enabling low-latency and low-memory HAR for real-time applications. In [108], an SVM was demonstrated that still outperforms many recent DL classifiers. Authors in [111] showed a hybrid Cascade Ensemble Learning model with each layer comprising Extremely Gradient Boosting Trees, RF, Extremely Randomized Trees, and Softmax regression.

1.3.4 Conclusion on classification in biopotential and inertial signals

All the reviewed studies on both applications involve signal acquisition at the Nyquist rate and then either subsequent extraction of necessary hand-crafted features in the digital domain followed by classification or end-to-end feature extraction, selection, and application-specific classification in a single stage with the help of DL algorithms in the digital domain as well. Hence, both approaches imply the digitization of captured continuous signals by an ADC. Next, digital samples are sent wirelessly to an aggregator for further processing or fed to feature engineering/classification implemented within the sensor node.

As said before, sensor nodes in WBANs are heavily constrained in available energy. Leaving all the processing on the digital signal to the aggregator side brings no benefit to these sensors from the energetic point of view since their consumption attributed to the transmission process remains unchanged. On the other hand, implementing the DL methods within WBAN sensors for an end-to-end process of feature extraction and selection and task-specific event classification seems unfeasible or extremely resource-consuming in terms of processing, memory, and energy.

Meanwhile, hand-crafted feature extraction within the sensor node with or without subsequent classification may be more energetically efficient. Nevertheless, such extraction methods derive application-specific features, generally intended for a fixed application, and, thus, do not ensure multi-application suitability. Moreover, the number of features extracted this way remains significant. Thus, performing the classification within the sensor requires implementing rather complex and power-hungry classification models. Alternatively, sending the features from the sensor node to the aggregator for further classification at its level entails a severe energetic cost due to the wireless transmission process.

Therefore, it is crucial to explore alternative acquisition techniques that can tackle the issue of data amount reduction in the analog domain before signal digitization within sensor nodes. This analysis is essential to minimize the number of transmitted samples or features and lower the associated power consumption.

1.4 Alternative acquisition techniques

In this section, we study two alternative acquisition techniques that capture less data from the analog domain and, thus, allow transmitting less information from the sensor to the

aggregator and reduce the power consumption induced by this process: Analog-to-Information (A2I) conversion and Analog-to-Feature (A2F) conversion.

1.4.1 Analog-to-Information (A2I) conversion: compressive sampling (CS) acquisition

The first alternative acquisition technique we studied is compressive sampling (CS), which allows for sub-Nyquist sampling. This concept, introduced by E. Candes in the 2000s [120], enabled the creation of Analog-to-Information (A2I) converters. These converters are designed to leverage the fact that many natural signals are sparse or compressible, meaning they have concise representations when expressed in a proper basis. In other words, the actual information rate of such signals is significantly less than its physical bandwidth.

1.4.1.1 The principle of CS

The main idea of CS is to perform the number of measures M less than N produced by uniform Nyquist-rate sampling but enough to reconstruct the signal on the basis of certain signal properties. The vector \mathbf{y} composed of M compressed measurements can be, therefore, expressed as follows:

$$\mathbf{y} = \Phi \mathbf{x} + \mathbf{z} \quad (1.12)$$

where \mathbf{x} stands for the input signal of size N , Φ represents the measurement matrix of size $M \times N$ and \mathbf{z} is noise. The vector of measurements \mathbf{y} is then passed to the last – very resource-intensive – CS reconstruction step, which recovers the sparse signal $\hat{\mathbf{s}}$ through a specific sparse recovery algorithm. Hence, as illustrated in Figure 1.7, the CS can be summarized into three main processes: sparse representation, CS acquisition (measurement), and CS reconstruction (sparse recovery) [120, 121].

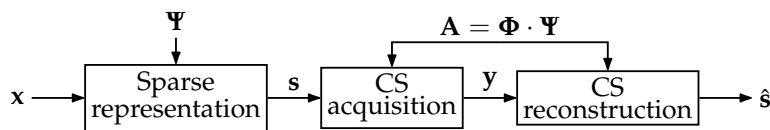


FIGURE 1.7 – Main steps of Compressive Sampling

Compressed signals' reconstruction algorithms are based on the notion of sparsity and on verification of the restricted isometry property [122]. A signal is said to be K -sparse in a basis or a dictionary if $K \ll M \ll N$ non-zero values can describe it in this basis or this dictionary. We can, therefore, express the input signal vector \mathbf{x} of N samples as:

$$\mathbf{x} = \Psi \mathbf{s} \quad (1.13)$$

where Ψ stands for the basis transform matrix and, e.g., in the case of the Fourier domain, corresponds to the inverse Fourier transform matrix, while \mathbf{s} represents the signal \mathbf{x} in the

sparse basis with the number of non-zero elements less or equal to K . Substituting for \mathbf{x} from (1.13) in (1.12), we obtain:

$$\mathbf{y} = \mathbf{\Phi}\mathbf{\Psi}\mathbf{s} + \mathbf{z} \quad (1.14)$$

Since, in practice, very few signals are perfectly sparse due to the presence of noise, we perform a compression step. Its objective is to retain only the significant coefficients in the chosen sparse basis and neglect those close to zero, below the compression threshold, as in the example depicted in Figure 1.8, which shows a signal sparse in frequency. Mathematically, a signal is considered compressible if the magnitudes of these coefficients sorted in descending order follow the power law decay [123]. The task comes down to finding among the possible solutions of the equation $\mathbf{y} = \mathbf{\Phi} \cdot \mathbf{\Psi} \cdot \mathbf{s}$ a K -sparse solution that satisfies the criteria of uniqueness and stability while allowing good reconstruction of the input signal. To achieve this, the sensing matrix $\mathbf{A} = \mathbf{\Phi} \cdot \mathbf{\Psi}$ must obey the restricted isometry property, which is challenging to prove in practice as it is an NP-hard problem.

To tackle this issue, we can adopt an alternative method based on the coherence between the measurement matrix $\mathbf{\Phi}$ and the basis transform matrix $\mathbf{\Psi}$ [124], expressed as follows:

$$\mu(\mathbf{\Phi}, \mathbf{\Psi}) = \sqrt{N} \max_{1 \leq u, j \leq N} |\langle \phi_u, \psi_j \rangle| \quad \text{with } 1 \leq \mu(\mathbf{\Phi}, \mathbf{\Psi}) \leq \sqrt{N}, \quad (1.15)$$

where $\langle \phi_u, \psi_j \rangle$ represents a scalar product of a row ϕ_u from $\mathbf{\Phi}$ and a column ψ_j from $\mathbf{\Psi}$. The lower the coherence, the fewer measurements M required for reconstruction, and the higher the compression factor N/M . Moreover, to ensure an accurate reconstruction of a K -sparse signal, the minimum number of measurements M should satisfy the following condition:

$$M \geq C \cdot \mu^2(\mathbf{\Phi}, \mathbf{\Psi}) \cdot K \cdot \log(N) \quad (1.16)$$

where C is a known constant whose value depends on the measurement matrix $\mathbf{\Phi}$ [120].

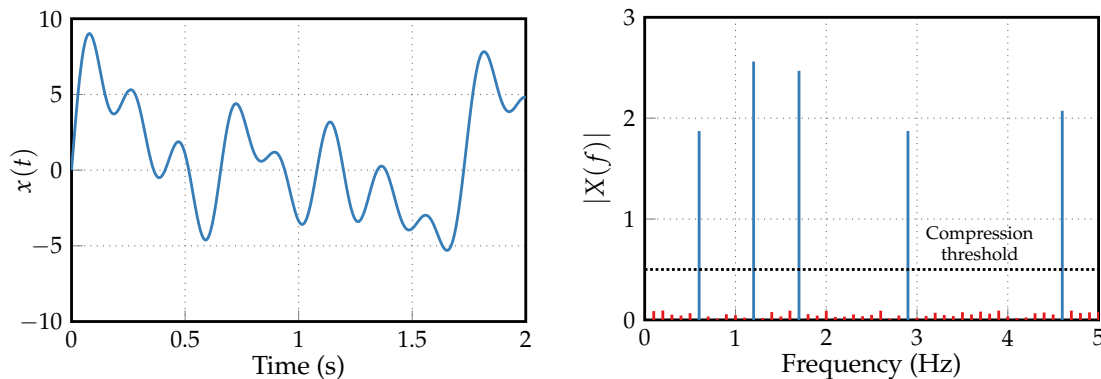


FIGURE 1.8 – Example of compressible signal sparse in frequency

1.4.1.2 A2I converter architectures

A2I converters implementing CS in hardware are composed of two main elements. First, an encoder performs the compression by multiplying the signal \mathbf{x} by the measurement matrix Φ . Next, an ADC transforms the compressed analog values into digital data. We briefly review the main A2I converter architectures for implementing CS.

Non-Uniform Sampling

As described in [13, 125], Non-Uniform Sampling (NUS) entails the sampling of a signal at non-uniform time intervals and selecting a subset of the samples acquired at the Nyquist rate using a pseudo-random clock. The architecture of NUS is illustrated in Figure 1.9 and comprises a sample-and-hold (S&H) block and an ADC driven by a pseudo-random clock.

This A2I converter architecture is the most straightforward for CS implementation, but it still operates at the Nyquist rate and is only suitable for signals that are sparse in the frequency domain.

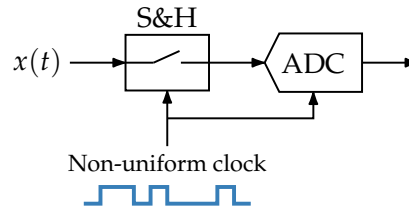


FIGURE 1.9 – Architecture of Non-Uniform Sampling

Random Demodulator

The principle of the Random Demodulator (RD), shown in Figure 1.10, is to multiply the input signal $x(t)$ by a pseudo-random sequence $p_c(t)$, taking values -1 or 1 and oscillating at or faster than the Nyquist frequency of $x(t)$. This demodulation step aims to "smear" the content of $x(t)$ all over the spectrum so that the following integrator does not destroy it. The signal is then sampled at a frequency well below the Nyquist frequency [126]. The integrator is reset to zero at each period T_s .

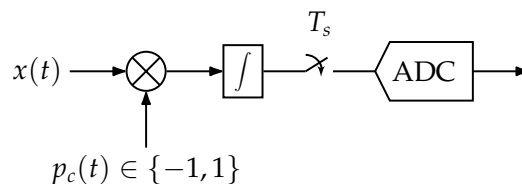


FIGURE 1.10 – Architecture of Random Demodulator

Compared with NUS, RD benefits from reducing ADC constraints regarding sampling frequency. However, it requires a random sequence generator that can operate at the Nyquist or an even higher rate.

Built upon the RD architecture operating with a single branch, the Random Modulator Pre-Integrator (RMPI) employs $N_c \leq M < N$ parallel random demodulators. This configuration allows simultaneous calculation of multiple coefficients $y_m(t)$ and increased integration time for any of them without extending the duration required to obtain all coefficients of the measurement vector \mathbf{y} [127].

Modulated Wideband Converter

Modulating a signal with a pseudo-random sequence for compression is only suitable for very specific signals [128]. In contrast, a Modulated Wideband Converter (MWC) made up of M branches first multiplies the input signal $x(t)$ with bandwidth B by a signal $p_i(t)$ within each branch, as seen in Figure 1.11. Here, the signals $p_i(t)$ with period $T_p = 1/f_p$ and decomposable into a Fourier series are periodic repetitions of pseudo-random sequences. After the modulation, the signal is filtered using a low-pass filter with cut-off frequency $f_c = 1/(2T_s)$ and then sampled at frequency F_s , where $2B \geq F_s \geq f_p \geq B$. Similar to RD and RMPI, this architecture, though, employs a low-pass filter (LPF) with a different impulse response [129].

MWC is an A2I converter architecture suitable for multi-band signals. It reduces the constraints imposed on S&H and ADC by allowing them to operate at frequencies below the Nyquist rate. However, its drawback lies in the necessity to allocate resources for storage and generation of the Nyquist-rate random signal sequence $p_i(t)$.

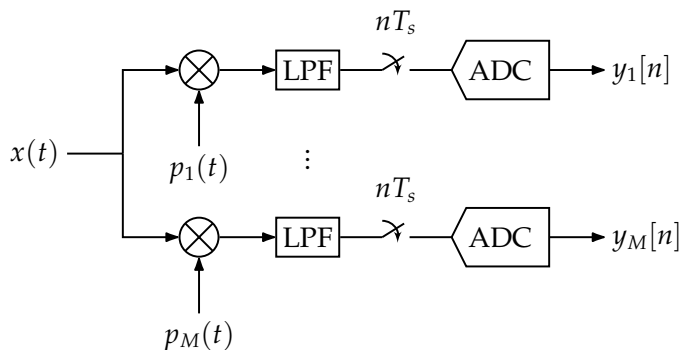


FIGURE 1.11 – Architecture of Modulated Wideband Converter

Non-Uniform Wavelet Sampling

The principle of Non-Uniform Wavelet Sampling (NUWS) involves the non-uniform sampling of wavelet transform coefficients of the observed signal. As opposed to a simple NUS technique, it includes conducting a continuous wavelet transform of the input signal $x(t)$ before non-uniform sampling (Figure 1.12). The continuous wavelet transform $\mathcal{W}x$ is performed by

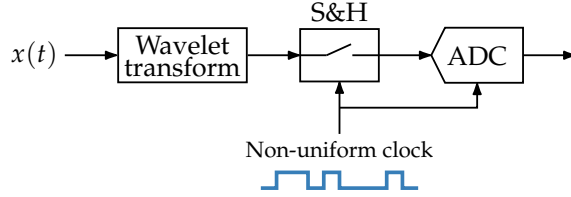


FIGURE 1.12 – Architecture of Non-Uniform Wavelet Sampling

multiplying the input signal by a wavelet and integrating the result over the wavelet support duration, as described below:

$$\mathcal{W}x(a, b) = \int_{\mathbb{R}} x(t) \cdot \xi_{a,b}^*(t) dt \quad \text{with } \xi_{a,b}(t) = \frac{1}{\sqrt{a}} \cdot \xi\left(\frac{t-b}{a}\right), \quad (1.17)$$

where $\xi_{a,b}^*(t)$ denotes the conjugate of $\xi_{a,b}(t)$, ξ is a mother wavelet (Haar, Gabor, Morlet, etc.), $a > 0$ is a scale factor providing the size of the wavelet support, and $b \in \mathbb{R}$ defines the temporal position of wavelet.

One of the primary advantages of the NUWS is that its continuous wavelet transform enables obtaining temporal and frequency information of the input signal at once. Moreover, wavelets offer multiple degrees of freedom: wavelet family (Haar, Gabor, Morlet, etc.), oscillation frequency, support size (if made uncorrelated from oscillation frequency, unlike the definition in (1.17)), and temporal position (time shift). At first glance, it provides greater flexibility and the ability to adapt to different types of signals. On the other hand, this leads to an extremely substantial total number L of possible wavelets in \mathcal{W} dictionary. Therefore, one needs not only to generate wavelets but also choose a subset of size $M \ll N \ll L$, allowing a significant reduction of required sampling frequency and ensuring good signal reconstruction.

1.4.1.3 Reconstruction algorithms

As seen previously, a reconstruction algorithm, i.e., a sparse recovery algorithm, aims to achieve a faithful representation of the original signal. For this purpose, it seeks a solution \mathbf{s} of equation (1.14) based on an undersampled set of measurements \mathbf{y} and the matrix $\mathbf{A} = \Phi \cdot \Psi$. However, since this is an underdetermined system of $M \ll N$ equations with N unknowns, the problem boils down to finding a sparse solution with the smallest possible number of non-zero elements K , which is a solution to the CS equation.

Sparse recovery algorithms include three main categories: convex relaxations, non-convex optimization techniques, and greedy algorithms. Those of the first group result in convex optimization problems that can be efficiently solved but at the cost of applying complex and slow advanced techniques, such as projected gradient methods and iterative thresholding. The non-convex optimization algorithms can recover the signal by relying on previous knowledge of its distribution. Greedy algorithms are the so-called sparse decomposition algorithms that aim to recover the signal iteratively. At each iteration, they perform a local optimal selection

to find the global optimum solution at the end of the algorithm. Although they are faster and easier to implement than convex optimization algorithms, they do not guarantee the best solution to the problem.

Table 1.11 presents the complexity and the minimum required number of measurements in several of the many existing sparsity recovery algorithms: Basis Pursuit De-Noising (BPDN), Compressive Sampling Matching Pursuit (CoSaMP), Iterative Hard Thresholding (IHT), Orthogonal Matching Pursuit (OMP), Regularized Orthogonal Matching Pursuit (ROMP), Subspace Pursuit (SP), Stagewise Orthogonal Matching Pursuit (StOMP), and Chaining Pursuit (CP). It reveals that the reconstruction algorithms exhibit a constrained compression ratio and entail severe energy and time costs to rebuild a sparse signal from an undersampled set of measurements. In addition to these principal drawbacks of sparse recovery algorithms and, thus, A2I converters in general, a complete or even approximative reconstruction of the original signal remains superfluous and needless for specific applications focused on detecting anomalies or events where only specific information is extracted from the signal.

TABLE 1.11 – Complexity and minimum number of required measurements in several well-known sparse recovery algorithms [130, 131]

Algorithm	Category	Complexity	Min. number of measurements (M)
BPDN	Convex	$O(N^3)$	$O(K \log N)$
CoSaMP		$O(MN)$	$O(K \log N)$
IHT		$O(MN)$	$O(K \log(N/K))$
OMP		$O(KMN)$	$O(K \log N)$
ROMP	Greedy	$O(KMN)$	$O(K \log^2 N)$
SP		$O(KMN)$	$O(K \log(N/K))$
StOMP		$O(N \log N)$	$O(N \log N)$
CP		$O(K \log^2 K \log^2 N)$	$O(K \log^2 N)$

1.4.2 Analog-to-Feature (A2F) conversion: combining acquisition and feature extraction

The Analog-to-Feature (A2F) conversion aims to extract only useful information in the form of features relevant to the specific task from the analog signal [12] directly within the sensor. Hence, it goes further than A2I conversion in diminishing the amount of transmitted data for applications dealing with event classification or anomaly detection in continuous signals. Rather than acquiring all the information about the signal at the Nyquist rate and extracting only necessary features in the digital domain, the A2F conversion combines the acquisition and extraction steps and, hence, appears more energetically efficient. These features are then digitized to serve as inputs for ML algorithms, where classification or regression is performed.

After the extraction and digitization of features, the A2F conversion can follow one of two approaches, as illustrated in Figure 1.13: either feature values are transmitted to a remote aggregator for the classification at its end or used to carry out the classification directly within the sensor. The second method allows for more efficient frugal communication by sending only the classification results and, thus, reduces the consumption due to wireless data transmission. Nevertheless, implementing the classifier at the sensor level will increase its power consumption unrelated to transmission.

To successfully implement an A2F converter, one needs to identify the relevant features for a given classification task through specific feature selection methods and how to extract them. Besides, since the A2F converter extracts analog domain features from signals, it cannot use the features discussed in Section 1.3. Therefore, it is necessary to find new types of features for extraction within the A2F converter.

The A2F converter in the acoustic sensing front-end of [132] decomposes the input signal into a set of 16 features. The on-chip Decision Tree (DT) classifier uses a subset of eight features and distinguishes between speech and background noise based on trained thresholds. The power consumption of feature extraction and classification is reduced by around eight times compared to the design in [133], which extracts digital features with comparable classification accuracy but lower latency.

Relying on the NUWS technique, the A2F converter in [134] extracts 16 spectral features from the audio signal. Then, an NN with two hidden layers of 200 neurons each classifies up to ten audio events, outperforming CS-based NUS and RD methods for A2I conversion. Compared to the traditional processing with the Nyquist rate sampling, the proposed design requires 16 times fewer measurements to obtain the same performance level.

One of the drawbacks of currently existing A2F converter solutions, such as presented designs performing voice activity detection [132] and audio-event classification [134], is that they extract very application-specific features and are designed for specific applications. Hence, these designs are not suitable for multi-application use cases.

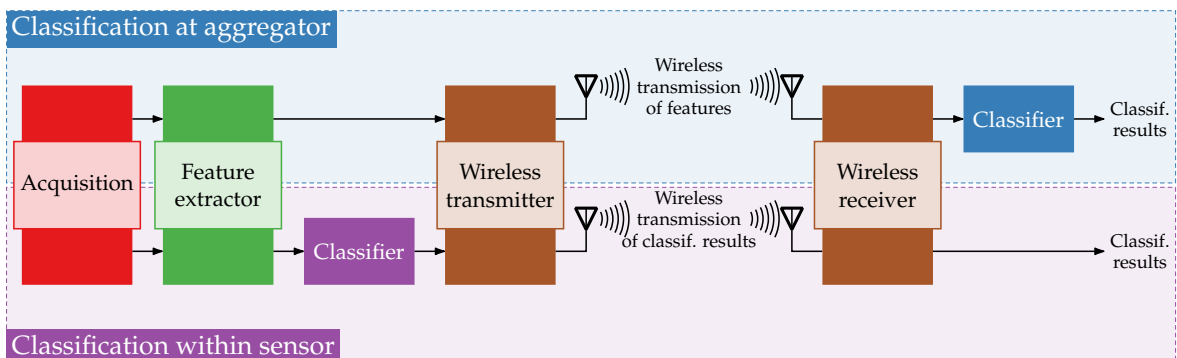


FIGURE 1.13 – Two approaches in A2F conversion: classification at aggregator or in sensor

1.4.3 Conclusion on alternative acquisition techniques

Since the emergence of the CS concept, various architectures of A2I conversion have been proposed for its implementation in hardware. This concept has been applied to acquire such types of signals as RF [13,125], astrophysical [135], and biological [136,137] with the purpose of reducing the volume of data transmitted from the sensor to the aggregator. Effectively, relying on the fact that certain real signals can be considered sparse and compressible after transformation into some domain, the CS allows the original signal to be recovered from the compressed data with much fewer measurements than in traditional methods. Nonetheless, it provides a limited compression ratio and performs a resource-intensive signal reconstruction, a useless, time- and energy-wise wasteful operation for applications dealing with event classification or anomaly detection. A limited compression ratio remains the principal drawback of the A2I conversion from the perspective of WBAN sensors because it limits the achievable reduction in the amount of wirelessly transmitted data from them. Moreover, most A2I converters implementing CS in hardware lack flexibility or adaptability since their system parameters are typically fixed during the design stage.

Nevertheless, the NUWS stands out among the A2I converter architectures studied above for its ability to simultaneously obtain the input signal's temporal and frequency information. Furthermore, it offers multiple degrees of freedom while constructing wavelet dictionaries and provides greater flexibility and adaptability to different types of signals. These facts make this technique a good candidate for feature extraction in event classification or anomaly detection applications. In particular, as already shown in [134], it can be used to extract features within an A2F converter, which achieves an even higher reduction of data quantity for wireless transmission from the sensor to the aggregator than A2I converters by combining the acquisition and feature extraction procedures in the analog domain. Hence, employing these two techniques in combination could facilitate the deployment of low-power biopotential and inertial sensors in WBANs for healthcare and beyond and relieve the respective communication chains regarding the amount of sent data and required throughput.

1.5 Conclusion

This Chapter presents existing strategies for improving the energetic efficiency of wireless sensors to address upcoming challenges in modern healthcare. One of these crucial challenges is an inevitable rise in the rate of chronic diseases due to current population growth and aging, as well as rapid unplanned urbanization and unhealthy lifestyles. In their turn, chronic diseases represent the leading cause of human deaths in the world [2]. Reducing the burden of such diseases on public healthcare is possible through their better management by early detection and ubiquitous health monitoring to avoid potentially much more expensive treatment [4–7]. However, conventional healthcare systems, relying on reactive treatment methods, often cannot detect these diseases early enough, thus entailing costly medical care.

Recent advances in microelectronics and IoT enabled the emergence of WBANs, considered a primary solution for building urgently needed proactive healthcare systems [8]. However, the wireless sensors that compose these networks are strongly limited regarding available energy and the allowed data transmission rates [9, 10]. Such constraints are especially relevant for biopotential and inertial sensors that capture their signals continuously. Reducing the amount of acquired and transmitted data from these sensors is possible in applications performing anomaly detection or event classification based on characteristic features extracted from signals. The conventional wireless sensor approach implies the ineffective Nyquist-rate acquisition, preserving the signal's complete information, which is then sent to the aggregator for subsequent feature extraction and classification.

Extracting features directly within the sensor would reduce the amount of transmitted data and respective power consumption. Hence, in this Chapter, we first examine existing feature extraction and classification methods for two applications: arrhythmia diagnosis in ECG signals and HAR in inertial signals. However, these methods are often too computationally expensive or application-specific, making them unfeasible for in-sensor implementation or non-extensible to other applications. Second, we review two alternative acquisition techniques capturing less information intended for digitization from the analog domain. The A2I converters implementing the CS concept [120] acquire fewer samples than the Nyquist approach. However, they offer a limited compression ratio and perform a resource-intensive recovery of the original signal [131], which is excessive for applications with classification, where only particular information is useful. In contrast, the A2F conversion extracts only features relevant for classification from the analog signal within the sensor node [12]. Then, ML algorithms take these features as inputs and perform the required classification. The NUWS technique, proposed in the A2I conversion [13] and adaptable to different types of signals thanks to its multiple degrees of freedom, can be used for feature extraction in the A2F converter to provide its multi-application suitability. Hence, in the next Chapter, we propose a generic A2F converter based on NUWS and show its implementation workflow for two applications: binary arrhythmia detection in ECG signals and HAR in accelerometer and gyroscope signals.

Chapter 2

Reconfigurable generic Analog-to-Feature converter

Chapter 1 highlighted the necessity for energy-efficient acquisition methods for sensors that constitute the WBANs, essential for modern healthcare. A significant improvement in data reduction and sensor autonomy can be achieved in applications involving anomaly detection or event classification, particularly with sensors that continuously capture signals. In particular, biopotential and inertial sensors belong to such categories and are power-hungry in signal acquisition and wireless transmission processes. The A2F conversion suggests extracting only features useful for the classification task from the analog-domain signals directly within the sensor. One drawback of current A2F converter solutions is that they are made for specific applications, meaning their feature extraction methods may not be suitable for other applications. However, the aim of this thesis, following the work carried out in [11], is to design the acquisition system incorporating a reconfigurable generic A2F converter suitable for processing several types of signals with low frequencies (below hundreds of kilohertz), such as ECG, EEG, voice, inertial signals, etc.

This Chapter first describes the developed A2F converter's architecture that leverages the NUWS technique for feature extraction. Then, we outline the workflow adopted throughout the remainder of the thesis to implement the A2F conversion for two studied applications: binary anomaly detection (loosely called arrhythmia detection further) in ECG signals and HAR in accelerometer and gyroscope signals. Specifically, we describe the methodology of the following workflow steps: data preparation, feature extraction, two-step feature selection, and classification.

2.1 A2F converter based on Non-Uniform Wavelet Sampling (NUWS)

We propose to design the acquisition system incorporating the A2F converter based on NUWS and having the following properties owing to the combination of both techniques:

- A2F architecture converter’s adaptability and reconfigurability;
- multi-application suitability;
- frugal extraction of a small number of abstract NUWS-based features from the respective analog signals;
- robustness to imprecisions in analog processing circuitry.

In this section, we introduce a reconfigurable A2F converter’s architecture and describe the NUWS-based technique employed by the converter to extract relevant features for the classification task.

2.1.1 Reconfigurable A2F architecture

To satisfy our needs, we have chosen to develop an architecture of an intelligent acquisition system presented in Figure 2.1. It contains a generic, adaptable A2F converter inspired by the feature-extracting ADC described in [138]. In summary, our acquisition system performs the operations listed below:

- extraction of analog-domain features with the help of several parallel reconfigurable feature extractors;
- direction of extracted features through a multiplexer to the inputs of an ADC;
- analog to digital conversion of extracted features’ values;
- application-specific binary or multi-class classification;
- context detection, which activates the necessary feature extractors and adjusts their internal wavelet generators according to the nature of the input processed signal, as well as the type and desired accuracy of classification.

Besides, classification algorithms will probably offer a notable benefit in A2F converters – mitigating design constraints on analog circuits. This advantage will be possible if classification algorithms can learn and accommodate eventual non-linearities introduced by analog circuits, such as amplifiers and filters, without compromising the classification process. In contrast, traditional processing methods assume linearity across all components.

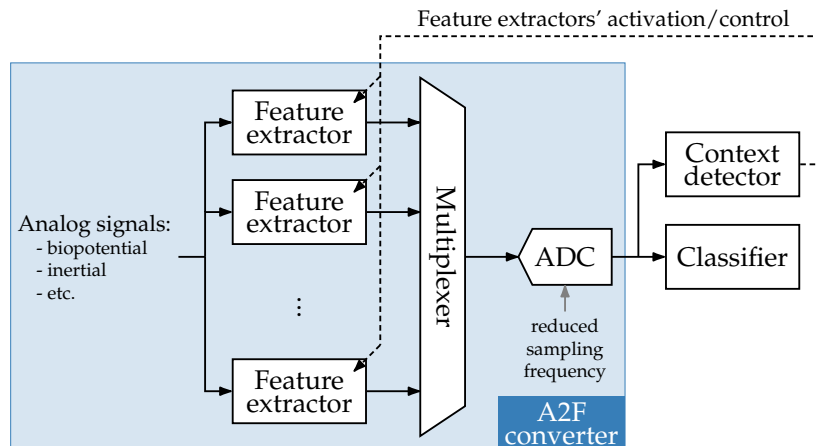


FIGURE 2.1 – Acquisition system architecture with reconfigurable A2F converter

2.1.2 NUWS-based feature extraction

Unlike the interpretable statistical features, generally derived from the signal in space, frequency, time, or time-frequency domains, we extract the features meaningless for humans but relevant for the classification procedure.

The NUWS technique, first proposed as a CS method for acquiring radio-frequency signals [13] and briefly described in Section 1.4.1.2, was chosen for feature extraction. As explained earlier, it is a good fit for feature extraction in event classification or anomaly detection applications thanks to its advantages, such as simultaneous temporal and frequency information extraction and multiple degrees of freedom in wavelet dictionary construction.

The overall flexibility of the NUWS technique, coupled with the possibility of reconfiguring the feature extractors within the A2F converter (Figure 2.1), will allow the envisioned system to acquire different types of signals and perform a profound analysis of the same signal if needed as well by first detecting the presence of anomalies and then performing its precise classification with extracting specific distinct features at both steps.

2.1.2.1 Continuous Wavelet Transform (CWT) and NUWS

Since their first mention in the appendix to the thesis of Haar in 1909 [139], wavelet functions are commonly used in communication, signal and image processing, data compression, and many other applications [140]. By definition, a wavelet ξ is a continuous, oscillating, centered around zero waveform. It is also time-limited, meaning it has a finite, bounded support with nonzero values. Wavelets are zero-mean and square-integrable functions as well:

$$\int_{-\infty}^{+\infty} \xi(t) dt = 0 \quad (2.1a)$$

$$\int^{\mathbb{R}} |\xi(t)|^2 dt < +\infty \quad (2.1b)$$

NUWS involves conducting a CWT of the input signal followed by non-uniform sampling. To perform the CWT, $\mathcal{W}x$, we multiply the input signal $x(t)$ by a wavelet and then integrate the obtained result over the wavelet support duration:

$$\mathcal{W}x(a, b) = \int_{\mathbb{R}} x(t) \cdot \xi_{a,b}^*(t) dt \quad \text{with } \xi_{a,b}(t) = \frac{1}{\sqrt{a}} \cdot \xi\left(\frac{t-b}{a}\right), \quad a \in \mathbb{R}^+, b \in \mathbb{R} \quad (2.2)$$

where $\xi_{a,b}^*(t)$ stands for the conjugate of $\xi_{a,b}(t)$ – wavelet obtained by scaling and shifting in time of the mother wavelet ξ (Haar, Gabor, Morlet, etc.) with the help of scale factor a and time shift b , respectively. Hence, a defines the size of the wavelet support, while b controls the wavelet’s temporal position.

From the perspective of electronic circuitry, NUWS-based feature extraction corresponds to mixing the analog signal with tunable wavelets and subsequently integrating them within the analysis window. One of the primary advantages of the NUWS is that its CWT obtains both temporal and frequency information of the input signal at once. However, according to the Heisenberg uncertainty theorem, the simultaneous resolution in time and frequency is limited [141]. As the wavelet support widens, one improves the precision in the frequency domain at the cost of less precise information in time and, conversely, for shorter support.

In contrast to definition (2.2), which implies that the oscillation frequency and the support size of the wavelet are correlated (inversely proportional), we make them independent. Thus, our transform becomes more flexible, offering three degrees of freedom when generating wavelets $\psi_{f_o, t_s, \Delta t}$ of the same family, including the oscillation frequency f_o , support size t_s , and temporal position Δt within a fixed-size analysis window of the signal. Mathematically, the extracted feature F is then expressed as:

$$F(f_o, t_s, \Delta t) = \int_{\Delta t}^{\Delta t + t_s} x(t) \cdot \psi_{f_o, t_s, \Delta t}(t) dt \quad (2.3)$$

2.1.1.2 The architecture of feature extractor

To implement the extraction of NUWS-based features within the developed A2F converter in accordance with the definition given in (2.3), we propose the architecture of the feature extractor shown in Figure 2.2.

Within each extractor, the incoming analog signal is first optionally amplified or attenuated in addition to the processing performed in the preceding common analog front-end (AFE). Next, the input signal $x(t)$, properly scaled in terms of magnitude, undergoes the process of mixing with a wavelet produced by a wavelet generator. The latter generates the required wavelets from chosen wavelet families and with given oscillation frequencies f_o , support sizes t_s , and temporal positions Δt . The result of mixing is integrated within the analysis window between the time instants Δt and $t_s + \Delta t$. Since the A2F converter contains multiple parallel feature extractors, the ADC receives the analog values of extracted features passed

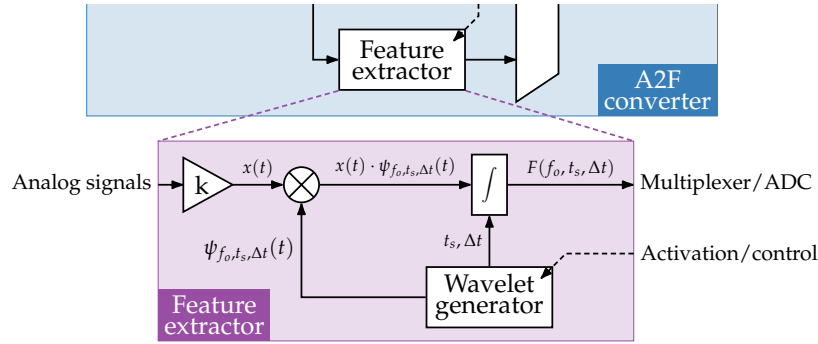


FIGURE 2.2 – Architecture of NUWS-based feature extractor

through the feature-selecting multiplexer (see Figure 2.1). The set of digitized features then serves as inputs for ML algorithms for further classification or detection task.

Within the frame of each feature extractor, its wavelet generator can be reconfigured, allowing it to produce several wavelets that do not overlap within the signal analysis window. Therefore, we can extract two or more features with non-overlapping supports, as those illustrated on top of Figure 2.3, from each extractor.

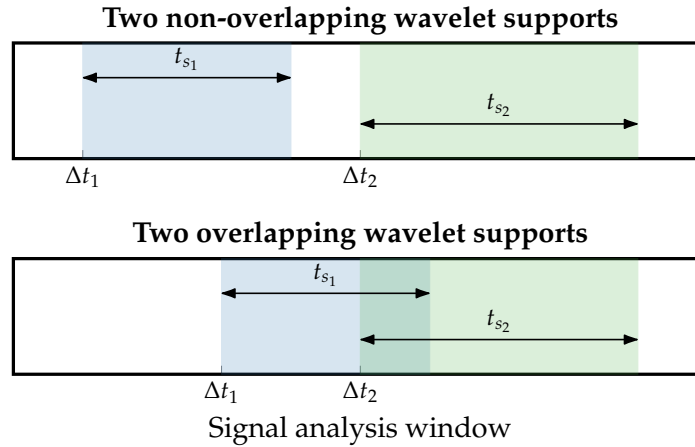


FIGURE 2.3 – Examples of non-overlapping and overlapping wavelet supports

Hence, to extract NUWS-based features, the architecture of our A2F converter requires the following components: optional amplifiers/attenuators, analog mixers, integrators, reconfigurable wavelet generators, a multiplexer, and an ADC.

2.1.3 Conclusion on the proposed A2F converter

Thus, the developed A2F converter consists of several parallel feature extractors. Within the analysis window, each extractor mixes the segment of the input analog signal with the tunable wavelet produced by the wavelet generator in its composition and integrates the result over the wavelet support duration. The reconfigurability of wavelet generators allows for extracting multiple features with non-overlapping supports within one analysis window using

the same extractor. The advantage of the NUWS-based technique is that it simultaneously obtains temporal and frequency information of the input signal. Moreover, it is adaptable to different types of signals thanks to several degrees of freedom, whose number is limited to three in our definition of extracted wavelet (2.3).

The proposed architectures of the A2F converter and its NUWS-based feature extractor are not new. However, compared to the work in [11], we enhance the efficiency of classifiers and speed up calculations by re-implementing the ML algorithms in more advanced software. In addition to binary arrhythmia detection already explored in [11], we study another application – HAR – to prove the multi-application suitability of the developed A2F converter.

2.2 Data preparation

In this section, we first describe the two datasets used in this thesis. Next, we explain all the necessary manipulations performed upon the signals from these datasets to simulate both studied applications: arrhythmia detection and HAR.

2.2.1 Description of datasets' signals

2.2.1.1 ECG recordings

To study binary arrhythmia detection in ECG signals, we chose the MIT-BIH Arrhythmia dataset [68] that researchers broadly use to evaluate their classifiers. Its original recordings were acquired by Del Mar Avionics model 445 reel-to-reel Holter recorders from 47 subjects studied by the BIH Arrhythmia Laboratory between 1975 and 1979. Among the subjects, 25 were men with ages ranging from 32 to 89 years, and 22 were women aged between 23 and 89 years. In total, there are 48 two-channel ambulatory ECG recordings, each slightly exceeding 30 minutes duration. Before digitization, the analog outputs were passed through a filter with a 0.1–100 Hz passband for anti-aliasing and ADC saturation limitation. The bandpass-filtered recordings were sampled uniformly at 360 Hz per signal with 11-bit resolution over a ± 5 mV range. Each heartbeat within every recording was annotated after a common decision of two or more cardiologists, who initially performed independent annotations and then resolved their disagreements.

We used only one channel – the upper signal – of two available channels in every recording. Typically, these signals have prominent normal QRS complexes. In most cases, the upper signal corresponds to a modified limb lead II (MLII) obtained by placing the electrodes on the chest. However, among 48 recordings, there are three exceptions. In one of them, two channels were reversed in the original dataset. Nevertheless, arrhythmia detectors should be capable of handling such situations that happen occasionally in clinical practice. In the other two recordings, the upper signal is a modified limb lead V5, which replaced MLII due to the impossibility of using it because of surgical dressings on the corresponding patients.

2.2.1.2 Inertial measurements

For HAR simulations, we chose the UCI-HAR dataset [99], which is commonly used in this field. Its original recordings contain three-axial linear acceleration and angular velocity signals with a sampling rate of 50 Hz. In laboratory conditions, a group of 30 volunteers aged from 19 to 48 years performed three dynamic and three static Activities of Daily Living (ADLs) freely – walking, walking upstairs, walking downstairs, sitting, standing, and laying. For brevity, we refer to these activities throughout the work as WALK, UP, DOWN, SIT, STD, and LAY, respectively. During the experiment, the subjects wore a waist-mounted Samsung Galaxy S II smartphone with an embedded accelerometer (Kionix KXTF9) and gyroscope (TDK InvenSense MPU3050). They repeated a protocol of activities twice: first, with the smartphone fixed on the left side of the belt and then in whatever way they preferred. To reduce the noise, the obtained signals were pre-processed with a median filter and a third-order Butterworth low-pass filter with a 20 Hz cut-off frequency. All the experiments were recorded on video to annotate the signals' intervals with their corresponding activities manually.

Since the acceleration signals have gravitational and body motion components, they were separated into gravity and body acceleration with the help of another Butterworth low-pass filter. In the dataset, some additional time signals and statistical features were obtained from initial three-axial signals as well. However, we kept only the original acceleration and gyroscope signals for our HAR simulations since our task is to extract useful features directly from analog signals, avoiding supplementary preliminary processing.

2.2.2 Shaping datasets' signals

2.2.2.1 Arrhythmia detection

Within 48 recordings of the MIT-BIH Arrhythmia dataset, among all 19 available classes, we maintained only the heartbeats with the following most frequently occurring classes (annotations): 'N' (normal beat), 'L' (left bundle branch block beat), 'R' (right bundle branch block beat), 'A' (atrial premature beat), 'V' (premature ventricular contraction), and '/' (paced beat). Thus, with our selection, we reduced the total number of beats from 112647 to 107045. Since we perform the binary arrhythmia detection, we divided all the heartbeats into two categories. Normal beats with 'N' annotation were attributed to a negative class without arrhythmia. All the remaining beats with either of the other five annotations constituted the group of observations belonging to a positive class with arrhythmia.

Intending to detect arrhythmia in each heartbeat, we set the length of the analysis window to 256 samples. This corresponds to 711 ms and, thus, approximately to the duration of one annotated heartbeat. Each heartbeat segment was synchronized within the analysis window by placing R-peak at the 100th sample. To keep a standard 70/30% proportion between training and test sets, as is typical in ML problems, we used 34 recordings (76132 observations, 71.1%) to generate features for a training set and 14 recordings (30913 observations, 28.9%)

for a test set. Such distribution resulted in 64/36% and 85/15% ratios between the number of instances belonging to positive and negative classes in training and test sets, respectively.

Since the proposed architecture of the intelligent acquisition system (Figure 2.1) contains a context detector, it can reconfigure the A2F converter’s feature extractors and thus modify the set of extracted features. Hence, after detecting the anomaly’s (arrhythmia) presence, it can more precisely explore the anomaly’s type by extracting another set of features relevant to another classifier that distinguishes multiple categories or classes. Authors in [11] performed the corresponding preliminary study and showed the feasibility of this approach by classifying abnormal heartbeats between five classes: 'L', 'R', 'A', 'V', and '/'. However, we will focus more on multi-class classification employed for another application and type of signals.

2.2.2.2 Human activity recognition

The UCI-HAR dataset’s original recordings were already divided into sliding analysis windows, 128 samples long, with a 50% overlap between adjacent segments. This corresponds to a 2.56 s segment containing only one ADL within its limits. Furthermore, the dataset provided a ready-made random partition of the obtained segments into training (7352 observations) and test (2947 observations) sets with a 71/29% proportion. This resulted in a relatively balanced distribution of instances between six classes in both sets, as shown in Figure 2.4.

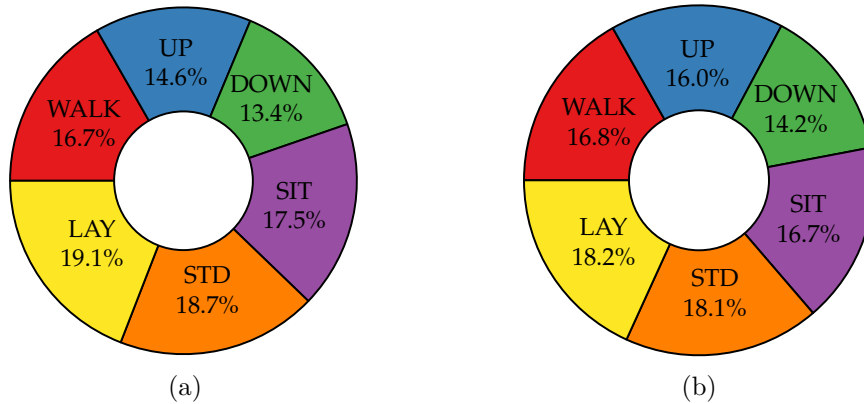


FIGURE 2.4 – Distribution of data between six classes in (a) train and (b) test sets for HAR

2.2.3 Conclusion on data preparation

Figure 2.5 summarizes operations performed during the data preparation step and reveals its position in the generic A2F converter’s implementation workflow. This step provides the training and test sets that contain observations in the form of datasets’ signals segmented into analysis windows for the next step, which performs the feature extraction. Within analysis windows, we extract NUWS-based features from the prepared signals.

An important note regarding the nature of prepared data must be made here. The A2F converter aims at extracting features from analog signals. However, the signals issued from

the datasets and exploited in our study represent uniform samples of analog signals from corresponding sensors. Hence, in our simulations, we actually approximate the analog-domain feature extraction. Effectively, the multiplication of signals' and wavelets' samples and subsequent ideal trapezoidal rule integration of the resulting uniform samples' sequences imitate analog mixing and integration of truly analog signals.

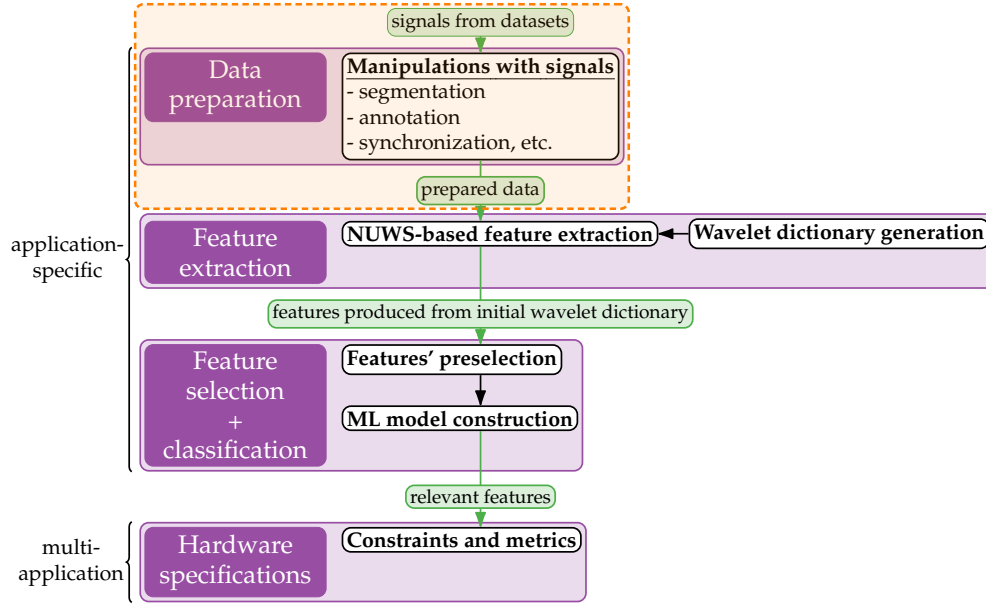


FIGURE 2.5 – Position of data preparation step in the implementation workflow of the generic A2F converter

2.3 Feature extraction

2.3.1 Choice of wavelet families

To extract NUWS-based features, we exploit Haar and Gabor wavelets. They represent principal examples of wavelet families implementable in analog electronics due to their simple mathematical forms.

2.3.1.1 Haar wavelets

Haar wavelets [142] represent a family of square functions that alternate between 1 and -1 within their support and turn to 0 elsewhere. Due to their simplicity, they are straightforward to generate. By definition, we describe the Haar wavelet's mother wavelet function as:

$$\xi(t) = \begin{cases} 1 & \text{for } 0 \leq t < \frac{1}{2} \\ -1 & \text{for } \frac{1}{2} \leq t < 1 \\ 0 & \text{elsewhere.} \end{cases} \quad (2.4)$$

Let us consider the interval defining the signal analysis window as $t \in [A, B]$. Next, we divide this interval into $2M$ equal subintervals of length $\Delta t = (B - A)/(2M)$ with $M = 2^J$ and J representing the maximum level of resolution. Introducing $j = 0, 1, \dots, J$ and $k = 0, 1, \dots, 2^j - 1$ as dilation and translation parameters, respectively [143], we can define the i -th basic Haar wavelet with $i = 2^j + k + 1$ as:

$$\xi_i(t) = \begin{cases} 1 & \text{for } t \in [t_0(i), t_1(i)] \\ -1 & \text{for } t \in [t_1(i), t_2(i)] \\ 0 & \text{elsewhere,} \end{cases} \quad (2.5)$$

where $t_p(i) = A + (2k + p)M\Delta t/2^j$ for $p = 0, 1, 2$. Hence, for any $i > 1$, the Haar wavelet is exactly one period of oscillation between 1 and -1 within its support. Additionally, the case $i = 1$, which is not defined by the foregoing notations, corresponds to the scale function with $\xi_1(t) = 1$ for $t \in [A, B]$ and $\xi_1(t) = 0$ elsewhere. Examples of the first eight Haar wavelets are demonstrated in Figure 2.6, where blue and red rectangles show the zones of $\xi_i(t)$, taking values other than zero.

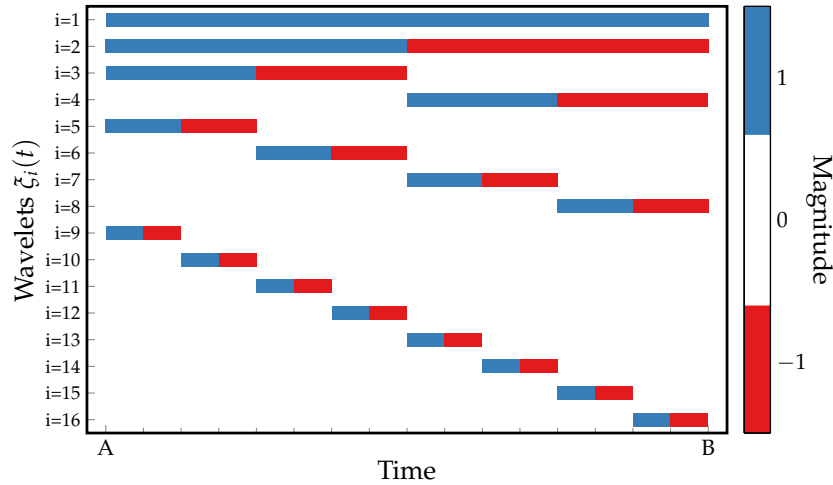


FIGURE 2.6 – Examples of first eight basic Haar wavelets

2.3.1.2 Gabor wavelets

The second family of exploited wavelets is the Gabor wavelets, invented to serve as a basis for Fourier transforms in information theory applications [144]. They result from multiplying a complex exponential by a Gaussian envelope and, thus, are challenging for a hardware generation with tunable parameters. However, their advantage is that the envelope is Gaussian in both the time and frequency domain, which minimizes the product of its standard deviations in both domains. In other words, it minimizes the uncertainty in information that the Gabor

wavelet carries. We can express the Gabor wavelet as follows:

$$\xi_{f_o, t_s, \Delta t}(t) = \frac{2^{\frac{1}{4}}}{\sqrt{t_s} \pi^{\frac{1}{4}}} e^{j2\pi f_o(t-\Delta t)} e^{-\left(\frac{t-\Delta t}{t_s}\right)^2} \quad (2.6)$$

where f_o is the central oscillation frequency of the complex sinusoidal carrier, t_s controls the width of the Gaussian function, and Δt performs the shift in time. As an example, Figure 2.7 illustrates the real and imaginary parts of the Gabor wavelet with $f_o = 250$ Hz, $t_s = 0.15$ s, $\Delta t = 0.5$ s, and normalized amplitude.

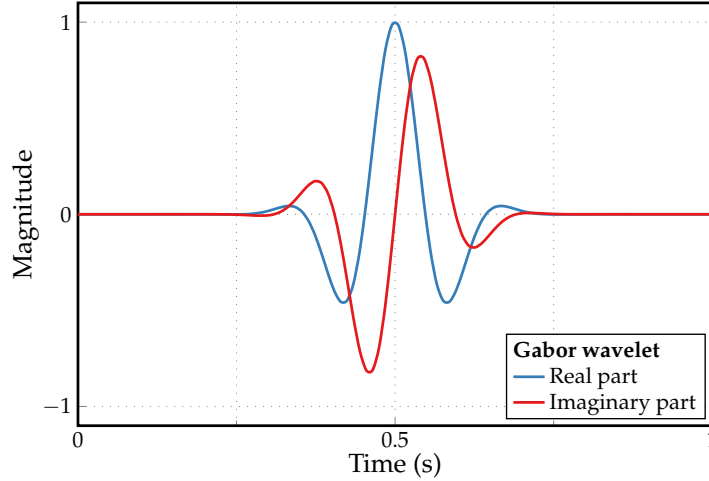


FIGURE 2.7 – Example of real and imaginary parts of Gabor wavelet

2.3.2 Generation of wavelet dictionaries

While constructing wavelet dictionaries, we utilized functions that, although not strictly defined as wavelets, possess characteristics similar to them and are referred to as wavelets throughout the thesis. Unlike the conventional definition of basic Haar wavelets (2.5), we allowed the support to contain multiple oscillation periods to generate this wavelet type's dictionaries. In the case of Gabor wavelets, compared to definition (2.6), we removed the amplitude scaling factor to normalize them to unity.

The construction of wavelet dictionaries presents a challenge since each of three quantities (degrees of freedom) – oscillation frequency f_o , support size t_s , and temporal position Δt – can take an unlimited number of values. It results in a potentially infinite wavelet dictionary containing all possible wavelets of the same family. Consequently, the number of features that can be extracted from the observed signal with the help of the NUWS technique employing these wavelets is also limitless. This fact contradicts our intention to reduce the amount of acquired samples. Hence, we should restrain the allowed values of these three quantities. In this regard, for both applications explored in this thesis, we constructed Haar and Gabor wavelet dictionaries in a manner that reduces their size and potential redundancy.

For example, the process of building Haar wavelet dictionaries occurred as follows. We started from the lowest value of oscillation frequency f_o corresponding to one wavelet period (1, -1 oscillation) in the analysis window. Then, we doubled up f_o until reaching the frequency equal to half of the dataset’s sampling frequency since half of Haar wavelet’s period cannot be shorter than one interval between consecutive input signal samples. For each f_o , we considered different support sizes t_s , starting from the one containing only one entire wavelet period and multiplying this size by two until reaching the complete analysis window length. To avoid overlapping wavelets with the same f_o and t_s , we allowed only the time shifts Δt that are the multiples of t_s . Figure 2.8 illustrates the first 26 Haar wavelets from the dictionaries constructed for both applications. Asterisk symbols denote new wavelets generated in addition to those already shown in Figure 2.6. These additional wavelets are produced by doubling the support sizes t_s of original wavelets that contained only one oscillation period.

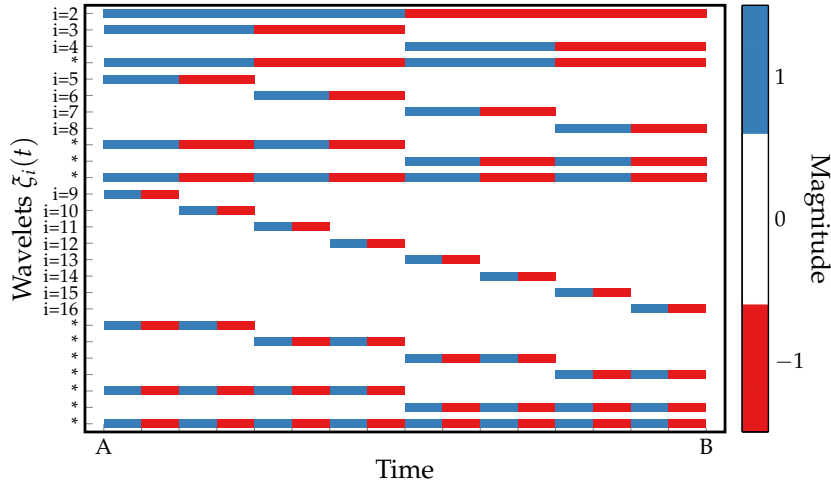


FIGURE 2.8 – Example of first 26 Haar wavelets used in simulations

A similar procedure has been applied while constructing the Gabor wavelet dictionaries but with certain peculiarities due to their more complex nature. We defined the minimum number of visible wavelet periods, thus establishing the minimum and maximum f_o and the minimum size of the Gaussian envelope t_s . To limit its possible size and temporal positions, we set the boundaries of the Gaussian envelope. Finally, the minimum time shift Δt has been defined to restrict the amount of constructed wavelets in the dictionary.

2.3.3 Conclusion on feature extraction

As shown in Table 2.1, the number of Haar and Gabor wavelets generated using the proposed method remains large, resulting in numerous extracted features for both applications. This number even surpasses the total amount of samples in the analysis window provided by the corresponding datasets: 256 samples in one annotated heartbeat segment of the MITDB and 768 samples in total from six inertial signals of the UCI-HAR dataset. Therefore, it re-

TABLE 2.1 – Comparison of original sample counts in the utilized datasets to initial wavelet dictionary sizes

Application		Arrhythmia detection	HAR
Dataset		MITDB [68]	UCI-HAR [99]
Analysis window	Length (samples)	256	128
	Nb. of signals	1	6
	Total Nb. of samples	$256 \times 1 = 256$	$128 \times 6 = 768$
Initial dictionary size	Haar wavelets	502	$248 \times 6 = 1488$
	Gabor wavelets	2534	$552 \times 6 = 3312$

veals the necessity of a proper feature selection procedure to identify a reduced set of relevant features for a particular classification task.

Figure 2.9 summarizes the operations composing the feature extraction step and indicates its position in the implementation workflow of the generic A2F converter. This step executes two operations. First, it generates an initial dictionary for a chosen wavelet family and a given analysis window length, which depends on a specific application. This dictionary is composed of wavelets with different values of oscillation frequency, support size, and temporal position. The restrictions are imposed on each of these three quantities' allowed values to reduce the size of the generated dictionary. The second operation involves mixing the segmented analog input signals with the dictionary's wavelets and integrating their product throughout the analysis

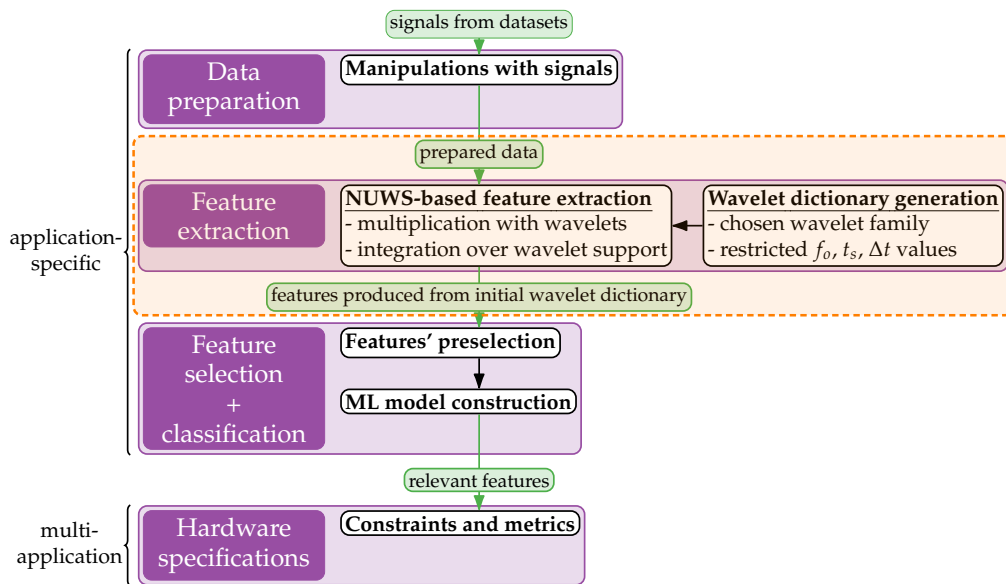


FIGURE 2.9 – Position of feature extraction step in the implementation workflow of the generic A2F converter

window. The produced coefficients representing the NUWS-based features are provided for the next step, combining feature selection and classification procedures.

2.4 Feature selection

The constructed dictionaries contain many wavelets, meaning that the number of possibly extracted NUWS-based features is extensive. Among all these wavelets, i.e., features, we need to maintain only a few that bring useful information and improve learning performance while building the ML classification models. Feature selection algorithms, regarded as dimensionality reduction techniques, carry out this operation. They involve selecting a subset of the most relevant features from the original set and removing redundant and irrelevant ones [145].

Feature selection is generally classified into supervised, unsupervised, and semi-supervised methods. Since we are dealing with classification, we apply the supervised methods designed for classification and regression problems. This group of methods aims to choose a subset of features that can effectively differentiate between samples from various classes. Supervised feature selection methods assess the relevance of each feature based on its correlation with the class labels.

We follow the procedure proposed in [11], which combines filter and wrapper methods of supervised feature selection. First, a filter method performs a fast preselection of features without building an ML model. It facilitates the deployment of the next step – the wrapping method of feature selection – whose complexity and execution time scale with the number of available features. However, the wrapping method provides adapted solutions with improved classification performance for a specific classifier and a given subset of features. We focus further only on those algorithms from these two groups of feature selection methods that showed the best performance in [11] and thus were tested in this thesis.

2.4.1 Filter methods

Filter methods involve two steps: ranking feature importance according to specific evaluation criteria and removing lowly ranked features to retain only those with a high score for a further classifier model construction. These methods generally offer greater computational efficiency compared to wrapper methods. However, they do not guarantee the optimal choice for the target learning algorithms since the feature selection relies purely on data characteristics, does not account for the interaction between features, and is entirely independent of any learning algorithm.

2.4.1.1 Fisher Score (FS)

Fisher Score (FS) [146] evaluates the distances between the feature values of the same and different classes as criteria. It prioritizes features with close values among observations from

the same class and distanced values between representatives of different classes. The Fisher score value FS of a feature F is given by:

$$FS(F) = \frac{\sum_{j=1}^{N_C} n_j \cdot (\mu_j - \mu)^2}{\sum_{j=1}^{N_C} n_j \cdot \sigma_j^2} \quad (2.7)$$

where N_C is the total number of classes, n_j indicates the number of examples belonging to a class j , μ is a mean value of feature F , while μ_j and σ_j represent the mean value and variance of feature F for samples in class j , respectively.

2.4.1.2 Information Gain (IG)

Information Gain (IG) [146] belongs to a family of information-theoretical-based methods, which can only work with discrete data. For a given dataset D , this supervised filter method of feature selection ranks each feature F by its information gain value IG expressed as:

$$IG(D, F) = H(D) - \sum_{i=1}^{N_F} \frac{|D_i|}{|D|} H(D_i) \quad \text{with } H(D_{(i)}) = \sum_{j=1}^{N_C} -p_{(i)j} \cdot \log_2(p_{(i)j}), \quad (2.8)$$

where N_F is the number of possible values that feature F can take, D_i corresponds to a subset from D with feature F taking the value F_i , $|D_i|/|D|$ denotes the portion of examples from D with $F = F_i$. $H(D_{(i)})$ stands for a Shannon entropy of a whole dataset D or a subset D_i , where $p_{(i)j}$ is the portion of examples in $D_{(i)}$ belonging to a class j , and N_C is the total number of classes.

Since this algorithm accepts exclusively discrete data, it requires preliminary data discretization techniques while operating with continuous feature values. In our case, we, therefore, divided each feature's range of continuous values into $N_F = 12$ equal intervals.

However, IG does not always execute an unbiased, fair ranking of features. Indeed, it favors the selection of features with a more significant number of values when the features take an unequal number of different values. An improved algorithm called the IG ratio introduces a factor that penalizes such features to correct for this bias [147].

2.4.2 Wrapper methods

In wrapper methods, the feature selection process iteratively relies on a predefined learning algorithm's predictive performance to assess the quality of selected features. A wrapper method typically performs the following two steps repetitively: creating a subset of features and training and evaluating the classifier built upon this subset. It repeats these two steps until satisfying some stopping criterion: either achieving the highest learning performance (based on one of the evaluation metrics presented in Section 1.3.1.2) or the desired number of chosen features or reaching the point where no more solutions exist.

2.4.2.1 Basic Sequential Forward Search (SFS)

Sequential Forward Search (SFS) [148] is a feature selection algorithm relatively simple to implement. It aims at selecting a subset of features from an entire set that best contributes to the predictive performance of a given classification model. To avoid the exhaustive test of all possible combinations of features, SFS iteratively builds up the feature set by adding only one feature at a time based on some criteria, usually related to predictive accuracy or another performance metric.

Algorithm 1 presents the basic SFS (according to our notation), where the classification accuracy stands for the predefined selection criterion. It starts by initializing the target set S with an empty set of features. In each iteration, we first obtain a new subset of features $S \cup \{F_i\}$ built upon adding one of the remaining features F_i , then we train and evaluate the classifier with this feature subset at its inputs. From all F_i , we choose the feature that improves the model performance the most, i.e., increases the accuracy ACC here. The target set S is gradually filled with features $F_{i'}$ that yield the highest classification metric. The algorithm stops the search at reaching the maximum number of selected features $N_{F,max}$. Optionally, it can stop at a certain iteration if none of the features increase the accuracy ACC . However, this does not guarantee that the final solution provides the best classification performance. Effectively, in the next iteration, some of the features added even to the subset that degraded the accuracy ACC in the previous iteration may increase it again.

Algorithm 1 Basic Sequential Forward Search

```

1:  $S \leftarrow \emptyset$ ,  $ACC(S) \leftarrow 0$  ▷ Target feature set  $S$  is initially empty
2: while  $|S| \leq N_{F,max}$  do ▷  $N_{F,max}$  is a maximum number of selected features
3:   for all  $F_i \notin S$  do ▷ Test each feature that is not yet in  $S$ 
4:      $ACC_i \leftarrow ACC(S \cup \{F_i\})$ 
5:    $i' \leftarrow \arg \max(ACC_i)$ 
6:    $S' \leftarrow S \cup \{F_{i'}\}$ 
7:   if  $ACC(S') > ACC(S)$  then ▷ Condition check and else block are optional and
only required to obtain ever-increasing accuracy
8:      $S \leftarrow S'$ 
9:      $ACC(S) \leftarrow ACC(S')$ 
10:  else
11:    break

```

The SFS algorithm's complexity scales quadratically with the number of available features. Depending on the size of the feature set, evaluating each subset can be computationally expensive. However, as shown in Table 2.1, the initial wavelet dictionaries and, thus, feature sets produced from them are significant. Therefore, we preselect the top 100 highly ranked features from these sets according to the filter method criterion (FS or IG) to considerably reduce the SFS algorithm's execution time.

2.4.2.2 Adapted SFS

One of the advantages of SFS is that we can adapt it to different performance criteria and algorithms. Given the inherent focus of the basic SFS algorithm on solely maximizing the classification accuracy, it is amenable to modification to accommodate the hardware complexity and energy consumption of the A2F converter. Therefore, the adapted SFS performs the first step in this direction by limiting the available number of parallel extractors. Each of them can extract multiple features, but only those produced by wavelets that do not overlap in the same analysis window. Figure 2.10 illustrates an example of such two Haar wavelets with non-overlapping supports.

As shown in Algorithm 2, the adapted SFS significantly differs from the basic SFS. In addition to the maximum number of selected features $N_{F,max}$, it takes the maximum number of parallel feature extractors $N_{Ext,max}$ as an input parameter. After the initialization of the target feature set S , each extractor's window Ext_j of length N_w is also set to zeros, where N_w represents the analysis window length. In arrhythmia detection and human activity recognition with chosen datasets, N_w corresponds to 256 and 128 samples, respectively. Similarly to the basic SFS, each iteration starts with training and evaluating classifiers based on all possible combinations $S \cup \{F_i\}$ built upon adding one feature. Here, we can use accuracy or any other metric as M_i . Next, we classify these features in descending order of metric M . Then, starting with the feature that improves the classification performance the most, we try to allocate the corresponding wavelet on any of the available extractors. The algorithm stops if none of the wavelets fit the unoccupied intervals within any extractor. Otherwise, it adds the allocated feature F_i to the target set S and removes it from the search set F . Moreover, at the end of the iteration, the features whose wavelets intersect the time intervals occupied within all extractors' windows are also removed from F since we can no longer extract them.

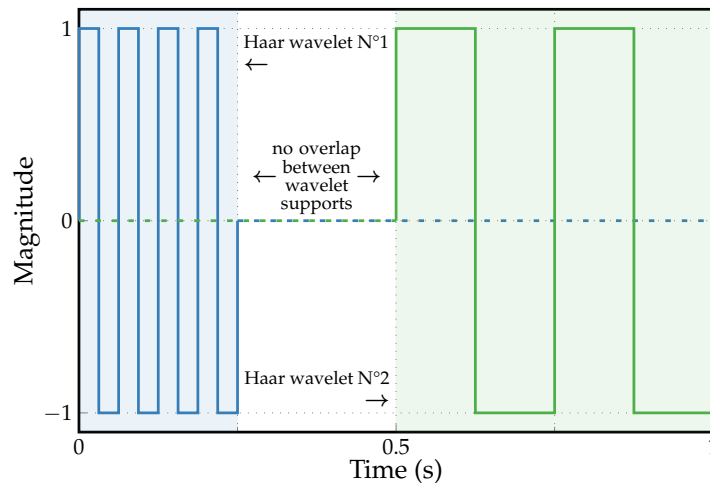


FIGURE 2.10 – Example of two non-overlapping Haar wavelets producing the NUWS-based features that can be extracted by the same extractor

Algorithm 2 Adapted/Optimized Sequential Forward Search

```

1:  $S \leftarrow \emptyset$ 
2: for all  $Ext_j \in Ext$  do ▷  $|Ext| = N_{Ext,max}$  – maximum number of extractors
3:    $Ext_j \leftarrow initArray(N_w, 0)$  ▷ Initialize each extractor’s window of size  $N_w$  to zeros
4:  $noSolution \leftarrow 0$ 
5: while  $|S| \leq N_{F,max}$  and  $noSolution \neq 1$  do
6:   for all  $F_i \in F$  do ▷  $F$  initially contains all available features
7:      $M_i \leftarrow M(S \cup \{F_i\})$  ▷  $M_i$  – accuracy or energy-aware metric (optimized SFS)
8:    $I \leftarrow sort(M_i, decreasing)$  ▷ Indices of features in descending order of metric  $M$ 
9:    $i' \leftarrow \emptyset$ 
10:  for all  $i \in I$  do
11:    for all  $Ext_j \in Ext$  do
12:      if  $(Ext_j \cap W_i) == \emptyset$  then
13:         $i' \leftarrow i$ 
14:         $Ext_j \leftarrow Ext_j \cup W_i$  ▷ Wavelet  $W_i$  is positioned onto extractor  $j$ 
15:        break
16:      if  $i' \neq \emptyset$  then
17:        break
18:  if  $i' == \emptyset$  then
19:     $noSolution \leftarrow 1$ 
20:  else
21:     $S \leftarrow S \cup \{F_{i'}\}$ 
22:     $F \leftarrow F - \{F_{i'}\}$  ▷ Removal of already chosen feature
23:     $Full \leftarrow initArray(N_w, 1)$  ▷ Array showing fully occupied time intervals
24:    for all  $Ext_j \in Ext$  do
25:       $Full \leftarrow Full \cap Ext_j$ 
26:    for all  $F_i \in F$  do
27:      if  $(Full \cap W_i) \neq \emptyset$  then
28:         $F \leftarrow F - \{F_i\}$  ▷ Removal of features that can no longer be extracted

```

2.4.2.3 Optimized SFS

The optimized SFS additionally takes into consideration the energetic cost associated with the extraction of each feature. To reduce energy consumption while maintaining a high classification performance, among the features providing the same gain in classification accuracy, it favors those requiring lower energy spent during the phases of wavelet generation and feature extraction. For this purpose, as shown in Algorithm 2, it merely replaces accuracy ACC with the energy-aware metric M_i , which measures the ratio between the gain in accuracy provided by the studied feature and its energetic cost:

$$M_i = \frac{ACC(S \cup \{F_i\}) - ACC(S)}{E_{F_i}} \quad (2.9)$$

where S stands for the set of previously chosen features, $ACC(S)$ is the classification accuracy obtained by the classifier trained on the set S , F_i represents the feature under test, and E_{F_i}

corresponds to the energy spent on its generation and extraction. The classification accuracy $ACC(\emptyset)$ of an empty set is fixed to a reference accuracy of a Zero Rule (ZeroR) classifier. For a given application, ZeroR simply designates the most prevalent class in the training data set for every tested sample. Thus, $ACC(\emptyset)$ is equal to the percentage of training examples with the most frequent class.

2.4.3 Discussion on feature selection

Since we extract NUWS-based features from the analog signal segments, only the feature space reduction techniques designed for single-vector-based ML problems have been studied. The techniques dedicated to the sequential data, such as the one presented in [149] and based on Hidden Markov Model (HMM), feature stacking, and LDA, are not applicable here.

The Sequential Floating Forward Search (SFFS) is another feature selection algorithm not discussed above, which can, however, address the inability of SFS to revert the addition of an already chosen feature to the target set S . Similarly to SFS, starting from an empty set, it fills S with features yielding the highest classification metric. However, after adding the feature, at the end of each iteration, it verifies whether removing any previously chosen feature improves the performance. SFFS can remove more than one feature at once as long as this continues to improve the performance. This algorithm could be a possible solution to improve classification accuracy for further works.

2.5 Classification algorithms

As stated in Section 1.4.2, the extracted NUWS-based features serve as inputs for ML algorithms for further classification. Given that both datasets utilized in our applications contain labeled data, we apply supervised learning for this task. In this section, we present a review of three methods used to implement supervised classification models in this thesis: Random Forest (RF), Support Vector Machine (SVM), and Neural Network (NN). These methods can perform non-linear classification tasks where a simple linear equation cannot represent class decision boundaries. Meanwhile, detecting diseases based on physiological data and classifying activities from biokinetic sensor data require non-linear models. Also suitable for non-linear tasks, K-Nearest Neighbours (KNN) models, however, need to store training data. This drawback hinders their potential implementation for classification within the sensor node with limited memory resources. Hence, we do not consider this method.

2.5.1 Random Forest (RF)

RF is a tree-based ensemble learning algorithm [150, 151] that constructs multiple DTs during the training phase, as illustrated in Figure 2.11. In its turn, DT represents a classification method with a flowchart-like-looking structure consisting of nodes and branches [53]. At each node, including the root node and following internal nodes, DT first selects the best

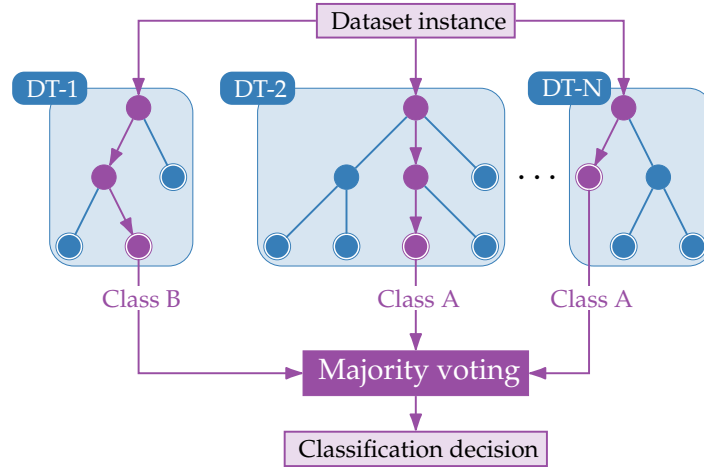


FIGURE 2.11 – Simplified Random Forest algorithm

attribute to test according to some criterion, such as IG (see Section 2.4.1.2), Gini impurity or entropy. Then, it performs the test and splits the dataset into subsets based on the attribute's value. Each branch leading from one node to another corresponds to the test result. DT recursively repeats the best attribute selection process and dataset splitting until it reaches a leaf node or a maximum allowed depth. Leaf nodes represent the points of a final decision, where all instances belong to the same class. However, individual decision trees, especially deep ones with many nodes, are known for their tendency to easily overfit, i.e., to fit too closely to training data.

On the contrary, RF with a robust number of decision trees reduces the risk of overfitting by injecting randomness in data and feature selection. This allows the improvement of the data generalization and the overall prediction performance of the classifier's model. To introduce variability in the training process and improve the model's robustness, RF employs a bootstrap sampling technique. It consists of creating different subsets of data for each decision tree by randomly selecting observations from the training data with replacements. RF also provides a random subset of features to train each tree to ensure that each tree specializes in different aspects of the data. A majority voting mechanism makes the final classification decision. It means that the most frequent prediction found among individual independent trees represents their collective decision.

2.5.2 Support Vector Machine (SVM)

SVM is another supervised ML algorithm that is naturally suitable for binary and adaptable for multi-class classification. The main purpose of an SVM is to find the optimal hyperplane that separates the data points of different classes in the N -dimensional feature space with the maximum margin [152].

When the data is linearly separable, linear SVMs use a linear decision boundary to separate the input data that does not need to undergo any transformations. Let us assume that the

training data points are expressed as (\mathbf{x}_i, y_i) , with \mathbf{x}_i representing the i -th instance's feature vector of dimension N and $y_i \in \{-1, 1\}$ being its class label. SVM constructs a hyperplane defined by the equation $\mathbf{w} \cdot \mathbf{x} + b = 0$, where \mathbf{w} stands for the weight vector (normal vector to the hyperplane), and b represents the bias term. The hyperplane's dimension depends on the number of features N . For $N = 2$, $\mathbf{x} = (x^1, x^2)$, it reduces to a single straight line, as shown in Figure 2.12. We call the data points from both classes that are the nearest to the hyperplane as support vectors. They define the hyperplane's position and orientation and, thus, the obtainable margin between the support vectors and the hyperplane. To ensure better generalization, SVM searches for a hyperplane with a maximum possible margin between the points of different classes. Such a hyperplane further serves as a decision boundary for classification. The search for an optimal hyperplane consists of solving a convex optimization problem formulated as:

$$\min_{\mathbf{w}, b} \frac{1}{2} \|\mathbf{w}\|^2 \quad \text{with } y_i (\mathbf{w} \cdot \mathbf{x}_i + b) \geq 1 \quad \forall i \quad (2.10)$$

For the test data \mathbf{x}_{test} , SVM predicts its class y_{test}^* by evaluating the following function:

$$y_{test}^* = \text{sgn}(\mathbf{w} \cdot \mathbf{x}_{test} + b) \quad (2.11)$$

However, in most real-world scenarios, the data is not linearly separable, e.g., by a straight line in a two-dimensional task. To handle such cases, non-linear SVMs preliminarily convert non-separable problems to separable ones. This involves applying the "kernel trick", which transforms the original lower-dimensional feature space into a higher-dimensional space, where the data becomes linearly separable. Feature mapping into a new space is performed using such kernels as polynomial, Gaussian, or sigmoid. In the modified space, a linear SVM then defines a non-linear decision boundary.

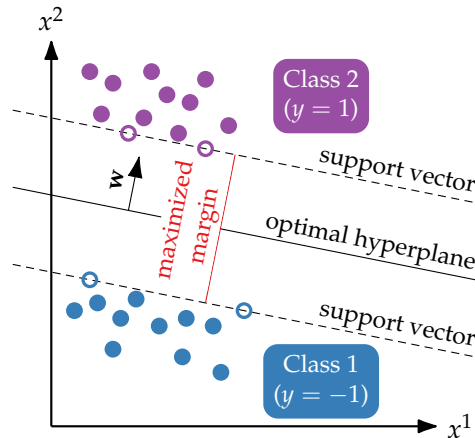


FIGURE 2.12 – Support Vector Machine's operating principle in two-dimensional feature space with linearly separable data

2.5.3 Artificial Neural Network (NN)

Artificial NNs are computational models inspired by the human brain's structure and functioning. They consist of interconnected units, or neurons, arranged in a series of layers. Due to the ability to learn complex patterns, artificial NNs are powerful tools for a wide range of applications beyond classification. They can handle problems with noisy data and a large number of features and classes.

Figure 2.13 shows a single artificial neuron, which receives n real value inputs x_i ($i \in [1, n]$). It then multiplies each input x_i by the corresponding weight w_i that determines i -th input's contribution. After multiplication, it calculates a weighted sum of the inputs, where we also add a bias term w_0 . To simplify the notation, we consider w_0 as a contribution of a constant input $x_0 = 1$. The weighted sum $z = \sum_{i=0}^n w_i \cdot x_i$ passes through an activation function $f(z)$, which allows to determine the neuron's output value y . The simplest activation function sgn results in 1 for the positive sum value z and in -1 elsewhere:

$$f(z) = sgn(z) = \begin{cases} 1 & \text{if } z > 0 \\ -1 & \text{elsewhere.} \end{cases} \quad (2.12)$$

Alternatively, with a pure sum of the weighted inputs $s = \sum_{i=1}^n w_i \cdot x_i$ and the bias w_0 seen as a threshold, the sgn activation function can be expressed as:

$$f(s) = sgn(s) = \begin{cases} 1 & \text{if } s > -w_0 \\ -1 & \text{elsewhere.} \end{cases} \quad (2.13)$$

Among the other activation functions, there are, e.g., a sigmoid function $\sigma(z)$, a Rectified Linear Unit (ReLU) $max(0, z)$, and a hyperbolic tangent $tanh(z)$:

$$\sigma(z) = \frac{1}{1 + e^{-z}} \quad (2.14)$$

$$max(0, z) = \begin{cases} z & \text{if } z > 0 \\ 0 & \text{elsewhere} \end{cases} \quad (2.15)$$

$$tanh(z) = \frac{e^z - e^{-z}}{e^z + e^{-z}} \quad (2.16)$$

The fundamental building block of artificial NNs is a perceptron, introduced by Rosenblatt in 1958 [153]. It represents the simplest type of NN, allowing the building of linear binary classifiers. A perceptron consists of a single neuron with an added learning. At every learning epoch, training a perceptron involves adjusting its input weights and bias based on the deviation of its output value y (predicted class) from the desired outcome \hat{y} (actual class):

$$w'_i = w_i + \eta (\hat{y} - y) x_i, \quad (2.17)$$

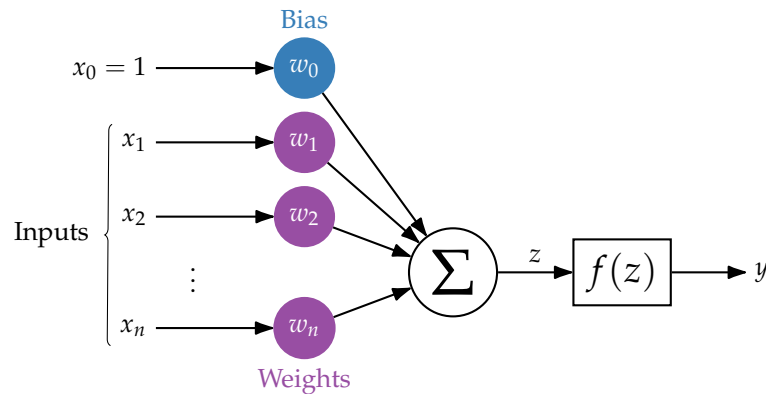


FIGURE 2.13 – Single artificial neuron's structure

where w'_i stands for the updated value of w_i and η corresponds to a learning rate, which determines the size of weight adjustments at each stage.

Since a single perceptron represents a one-layer network, it cannot solve non-linear problems that require multiple layers of abstraction. Therefore, we use it as a building block to construct more complex multi-layer NNs consisting of three types of layers. Each neuron in the input layer receives one feature from the input data and passes it through without any computation to the first hidden layer. Hence, the input layer contains the number of neurons equal to the number of features in the dataset. Next, we have one or more hidden layers, where neurons take the inputs from the previous nodes (not necessarily all) and perform a weighted sum followed by an activation function. The number of neurons in the output layer depends on the classification type – one for binary and multiple for multi-class classification.

Feedforward NNs represent the simplest kind of multi-layer NNs, where the information moves strictly in a forward direction – from the input to the output layer – and there are no cycles or loops between the units. A feedforward NN operates in two iterative phases: feedforward and backpropagation phases. In the feedforward phase, the input data propagates through the network and reaches the output layer, where the prediction is made. In the backpropagation phase, the error between the prediction and the desired output value calculated using a loss function propagates in the opposite direction. Meanwhile, the weights within neurons are updated using gradients of the loss to minimize the error. A special case of a feedforward NN is an MLP, whose layers are fully connected, i.e., each node of the current layer is connected to each node in the next layer. Figure 2.14 illustrates an example of a feedforward NN with 3-4-3-2 topology and not all fully connected layers, where dashed gray arrows denote the disabled connections.

2.5.4 Conclusion on classification algorithms

Each of the three supervised ML algorithms studied above – RF, SVM, and NN – is suitable for classification tasks with non-linear data. However, they have their advantages

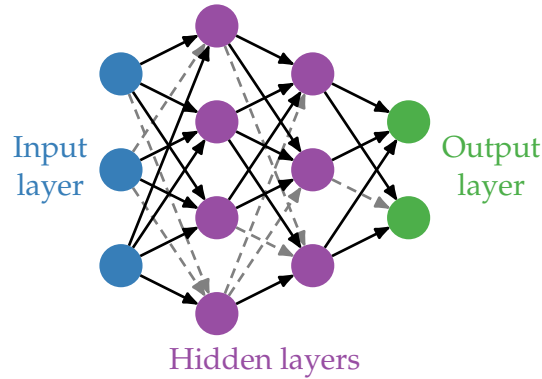


FIGURE 2.14 – An example of a feedforward Neural Network

and drawbacks, as summarized in Table 2.2. RFs are great for interpretability and robustness, easier to tune, but can become complex and resource-intensive. SVMs are effective for high-dimensional data with clear decision boundaries but computationally intensive and harder to tune. NNs are extremely powerful and flexible, especially for large datasets and complex tasks, but require significant computational resources, can be prone to overfitting, and lack interpretability. Choosing the right algorithm depends on the specific problem, the nature and size of the dataset, the available computational resources for model training, and the hardware constraints for its implementation. In Chapter 3, we identify the most suitable algorithm through training and evaluating classification models for both studied applications.

Figure 2.15 summarizes the operations performed during the feature selection and classification step and shows its position in the implementation workflow of the generic A2F converter. Specifically, through training and evaluating classifier models, we identify the relevant extracted features for both studied applications. This, in turn, allows us to define the hardware specifications that suit all applications to build a generic A2F converter.

TABLE 2.2 – Comparison of supervised ML algorithms for classification

Model	Advantages	Drawbacks
RFs	<ul style="list-style-type: none"> • Robustness to noisy data and overfitting • Ease of parallelization for faster training 	<ul style="list-style-type: none"> • High complexity and memory usage with deep and numerous trees • Poor performance with very high-dimensional data • Slow training with many trees and high-dimensional data
SVMs	<ul style="list-style-type: none"> • Good performance with high-dimensional data, especially when features outnumber samples • Robustness to overfitting 	<ul style="list-style-type: none"> • Slow, memory-intensive training, especially with large datasets • Performance dependency on kernel choice and its parameters' tuning • Lower interpretability with complex kernels
NNs	<ul style="list-style-type: none"> • Capability of modeling complex patterns and relationships in the data • Handling a large number of features and classes 	<ul style="list-style-type: none"> • Slow, memory-intensive training with large datasets; convergence speed dependency on initial weights • Design, tuning (architecture, learn. rate, etc.) complexity • Proneness to overfitting, especially with small datasets • Lack of interpretability

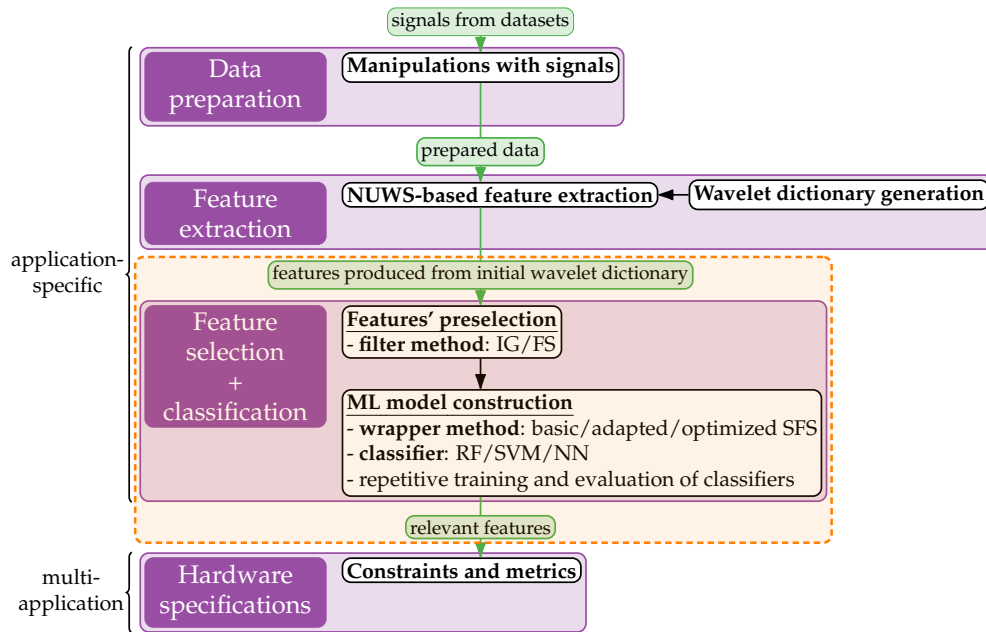


FIGURE 2.15 – Position of feature selection and classification step in the implementation workflow of the generic A2F converter

2.6 Conclusion

This Chapter first describes the proposed A2F converter's architecture and then outlines the converter's implementation workflow for two studied applications. The thesis aims to design the acquisition system with a reconfigurable generic A2F converter suitable for several types of low-frequency signals. For this purpose, we chose the architecture with multiple parallel feature extractors that operate on the NUWS principle and can individually extract multiple non-overlapping features within a single analysis window. The extracted NUWS-based features represent the coefficients obtained by mixing input analog signal segments with tunable wavelets and subsequently integrating these multiplication products.

Figure 2.16 illustrates the implementation workflow of the generic A2F converter. It summarizes the operations performed within application-specific steps (data preparation, feature extraction, two-step feature selection, and classification). In addition to direct links, this Figure shows the feedback between the steps and their operations. In particular, the lengthy execution of a joint feature selection and classification process may eventually require modifications in previous operations. Since this process includes an iterative ML model construction for a specific classifier using a wrapper feature selection method (SFS algorithm), its complexity rapidly increases with the number of available input features. Hence, we may need to take fewer features from the ranking provided by a filter method of features' preselection or even modify the wavelet dictionary generation process to produce fewer NUWS-based features in the preceding feature extraction step. Furthermore, the envisioned hardware implementation of the multi-application A2F converter's circuit imposes several constraints. Indeed, insuffi-

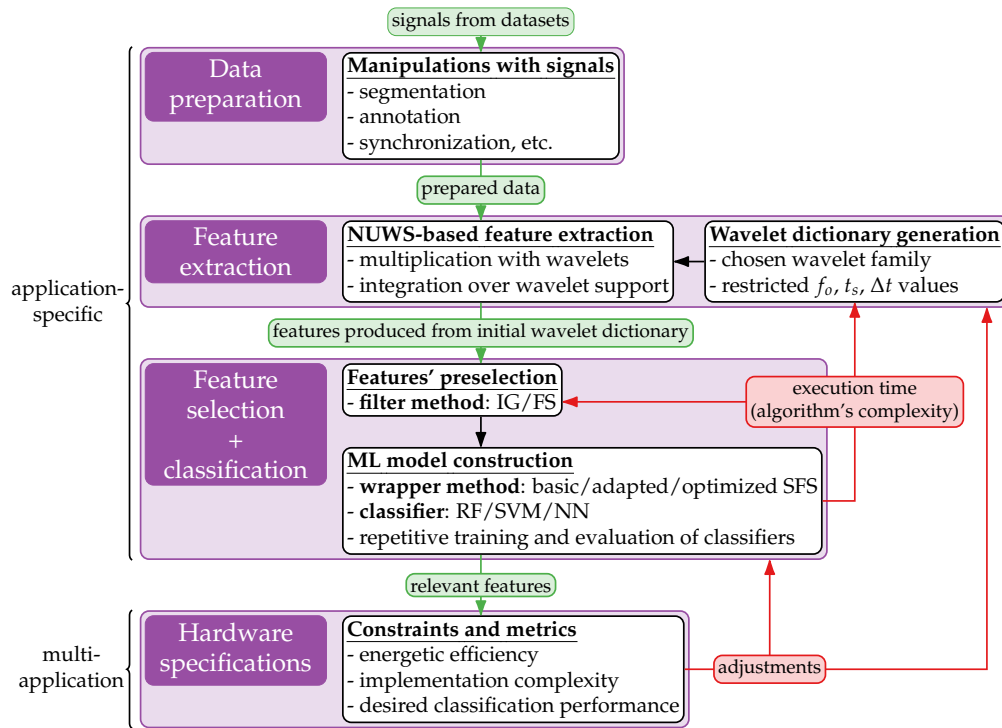


FIGURE 2.16 – Detailed implementation workflow of the generic A2F converter

cient classification performance, low energetic efficiency, or high implementation complexity may require adjustments within the feature selection, extraction, and classification steps.

In the next Chapter, we train and evaluate classification models to identify the most suitable classification algorithm and the relevant extracted features for both studied applications. With these features found, we can define in Chapter 4 the hardware specifications that suit all applications for building a generic A2F converter.

Chapter 3

Simulation results for healthcare applications

As emphasized in Chapter 1, WBAN sensors are indispensable for addressing upcoming challenges in healthcare. The energetic efficiency of such sensors is one of the most critical factors defining the WBANs' success. Substantial energy savings can be realized in sensors with a continuous signal nature by extracting only classification-relevant features in the analog domain directly within the sensor node through A2F conversion.

Chapter 2 described the proposed generic A2F converter's architecture that leverages the NUWS-based feature extraction technique, offering adaptability to different types of signals. Then, it outlined the converter's implementation workflow for two studied applications: binary arrhythmia detection in ECG signals and HAR in accelerometer and gyroscope signals.

In this Chapter, we train and evaluate classification models for these applications. We apply the feature extraction, feature selection, and classification methodologies outlined in Chapter 2. Concretely, the joint process of feature selection and task-specific classification consists of iterative ML model construction for a chosen classifier (RF, SVM, or NN) using the SFS algorithm, a wrapper feature selection method.

First, we re-produce the results obtained in [11] for binary arrhythmia detection. However, to enhance the efficiency of ML models, particularly NNs, and speed up calculations using graphics processing units (GPUs), we implement the ML algorithms using Python with Scikit-Learn and TensorFlow libraries instead of MATLAB[®] employed for this purpose in [11]. Second, we apply the simulator validated in arrhythmia detection simulations to a newly proposed application – HAR in inertial signals. As a result, we identify the relevant extracted features for each application. Based on these features, Chapter 4 derives the specifications required for the hardware design of the developed A2F converter.

3.1 Arrhythmia detection in ECG signals

Binary arrhythmia detection simulations in this work employ exclusively Haar wavelets despite a slight loss in classification accuracy compared to Gabor wavelets, as confirmed in the complete study on this matter performed in [11]. Since Haar wavelets are straightforward to generate digitally, they simplify the structure of the wavelet generator and mixer when designing the A2F converter.

3.1.1 Comparison of different filter methods and classification models

To prove the utility of the chosen wrapper method of feature selection – SFS algorithm – we first demonstrate the performance of classification models built without it. In this case, three studied classifiers were trained on the subsets of input features arranged in the order directly provided by one of the filter methods, namely FS or IG criterion. As mentioned in Section 2.4.1, such a choice of features gradually added to the examined subset is not optimal since features are ranked according to data characteristics and independently of the learning algorithm and achieved classification performance. Figure 3.1 shows the corresponding results obtained with three different types of classifiers: RF, SVM, and feedforward NN. We constructed these classifiers using Scikit-Learn, which is a popular software ML library in Python that offers a broad range of models.

From this figure onwards, we plot the accuracy and other metrics against the number of chosen features, serving as the classifier’s inputs. Additionally, we show a ZeroR accuracy as a benchmark reference line for actual classification methods. It represents the performance of a suppositive classifier that predicts the majority class to all tested observations. In our test set for arrhythmia detection, 85% of heartbeats are normal and belong to a negative

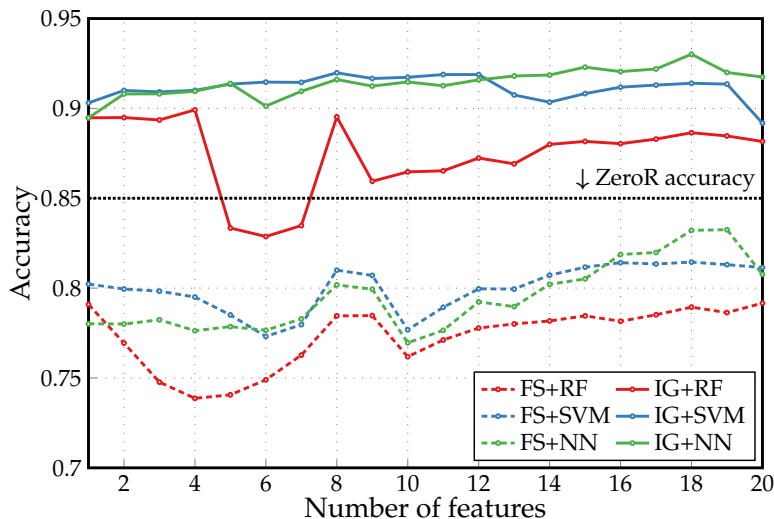


FIGURE 3.1 – Accuracy of binary arrhythmia detection performed by different classifiers built using Scikit-Learn and based on input features sorted directly by filter methods

class without arrhythmia. Thus, a ZeroR classifier attributes this class to every instance and correctly predicts 85% of cases. Figure 3.1 reveals that the classification models with input features selected by FS criterion are less accurate than the ZeroR classifier. Hence, we decided to use the IG criterion as a filter method of feature preselection in the following simulations.

Among the studied classifiers, the artificial NN outperformed the RF and SVM models regarding the highest achievable accuracy. This simple feedforward NN contains one hidden layer of ten neurons. We then built and trained NN classifiers with the same internal structure using TensorFlow for comparison. In contrast to Scikit-Learn, among other differences, TensorFlow is more of a low-level Python library implied for use with NNs, benefiting from GPUs' usage for more efficient training. Effectively, as illustrated in Figure 3.2, the NN classifiers built and trained with TensorFlow guarantee better classification performances than those with Scikit-Learn when the number of input features exceeds five. Therefore, we keep this configuration for further simulations that profit from the SFS algorithm to improve the classification performances.

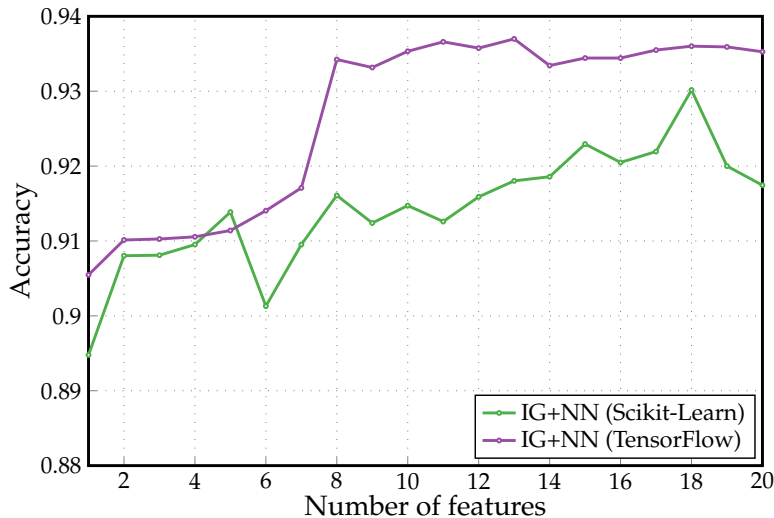


FIGURE 3.2 – Accuracy of binary arrhythmia detection performed by NN classifiers built using Scikit-Learn and TensorFlow and based on input features sorted directly by IG criterion

3.1.2 Impact of the basic SFS algorithm

Figure 3.3 demonstrates the impact of the basic SFS algorithm on the accuracy, sensitivity, and specificity of binary arrhythmia detection performed by NN classifiers with one hidden layer of ten neurons trained during 1500 epochs using the TensorFlow library. Figure 3.3a corresponds to the results of the case previously studied in Figure 3.2, where features were added to the tested input feature set in the order strictly specified by the IG ranking. On the contrary, to obtain the metric values in Figure 3.3b, we combined the preselection of the 100 best features according to the IG criterion with the basic SFS algorithm performed after it. This combination is advantageous in terms of the overall learning duration and obtained

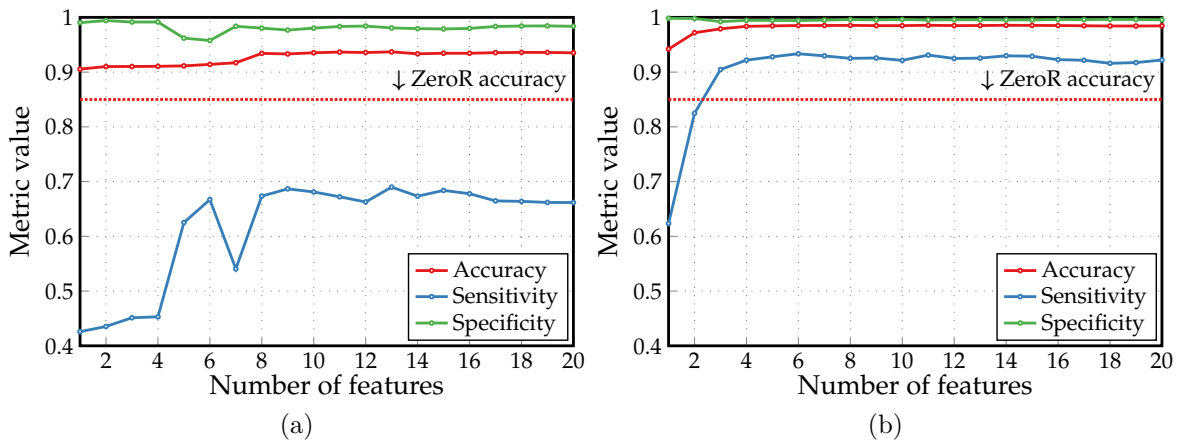


FIGURE 3.3 – Impact of basic SFS algorithm on binary arrhythmia detection performed by NN classifiers: (a) feature selection only with IG; (b) feature selection with IG + basic SFS

classification performance. Indeed, the preliminary reduction of the set available for the SFS algorithm from 502 to 100 features significantly shortens its execution time. Secondly, SFS relies on predictive performance while deciding which feature to add next to the target set.

Selecting features only with the IG criterion filter method, the highest achieved accuracy is 93.6% with 11 features. Adding the basic SFS algorithm allowed us to obtain a 98.5% accuracy in the classifier requiring only six features. The second, no less critical metric for binary arrhythmia detection is sensitivity (recall). It represents the classifier’s ability to identify true positives, i.e., to recognize arrhythmic heartbeats among truly abnormal instances. The feature selection only with the IG leads to, at most, 69% sensitivity with 13 chosen features. At the same time, the combination with the basic SFS algorithm boosts the sensitivity up to 93.4% in the classifier requiring six input features. Thus, combining two feature selection procedures increases binary arrhythmia detection’s achievable accuracy and sensitivity by 5% and 24%, respectively, with considerably fewer features. Although specificity is a less significant metric since it shows how well the classifier identifies the instances without arrhythmia, it is also improved, exceeding 99% for any number of features.

3.1.3 Classification with improved SFS algorithms

The combination of feature preselection by the IG criterion and the basic SFS algorithm allowed us to enhance the classification performance of binary arrhythmia detection. However, this SFS algorithm’s version does not consider the A2F converter’s induced hardware complexity or energy consumption. Hence, we address these issues by training and evaluating classifiers with the help of modified algorithms: the adapted and optimized SFS.

3.1.3.1 Adapted SFS to limit the number of extractors

The adapted SFS algorithm (see Algorithm 2 for details) limits the maximum number of parallel extractors $N_{Ext,max}$ within the A2F converter. This procedure affects the resulting choice of features for the target set. Indeed, each available extractor can allocate multiple wavelets with non-overlapping supports and, thus, can extract only the features produced by these wavelets during one analysis window of the input signal.

We performed the adapted SFS with three different values of a maximum number of parallel extractors and obtained the performances illustrated in Figure 3.4. The NN classifiers had the same internal structure – one hidden layer of ten neurons – and were trained on the same top 100 features from the IG ranking used earlier. Here, we demonstrate the accuracy and sensitivity as the two most important binary arrhythmia classification metrics and the energy required to extract the features chosen for the corresponding NN classifier.

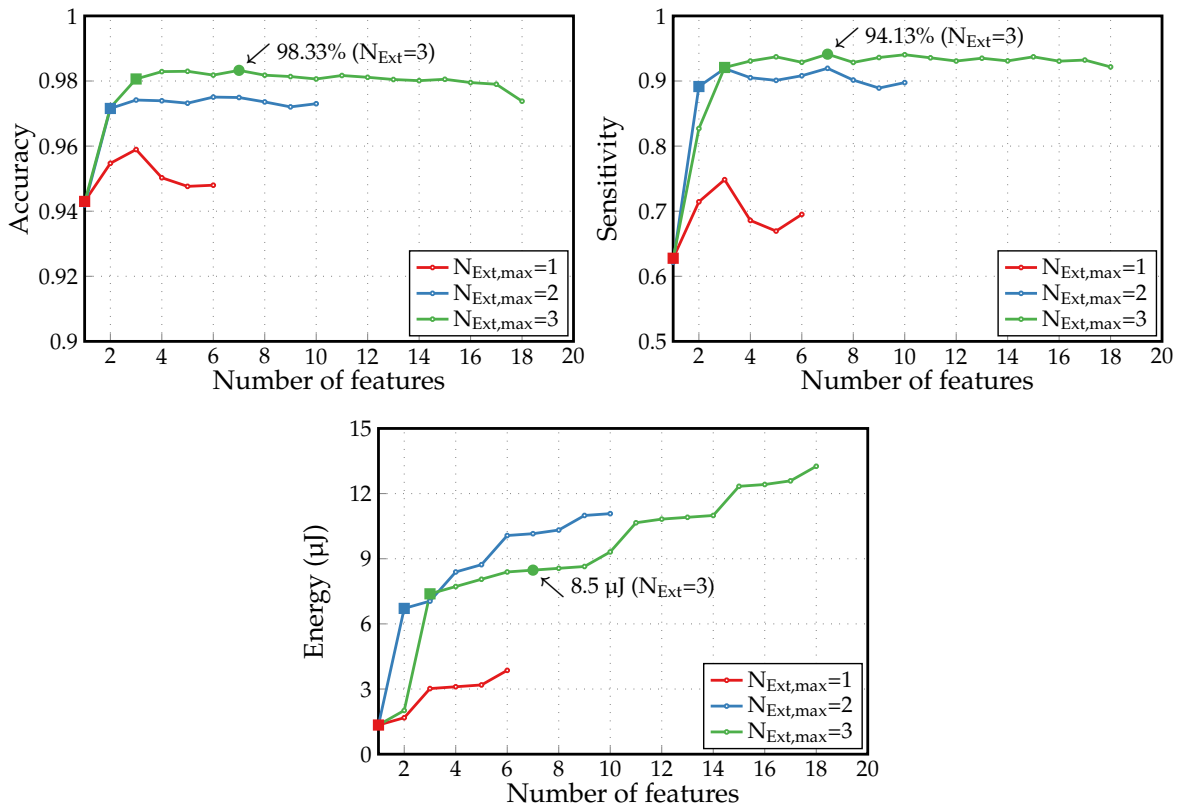


FIGURE 3.4 – Metrics of binary arrhythmia detection performed by NN classifiers with IG + adapted SFS feature selection

While calculating the energetic cost of each extracted feature E_{A2F}^{feat} , we assumed that the A2F converter's components are only active and consume the power at specific moments where the wavelets are non-zero. Thus, we can express E_{A2F}^{feat} as follows:

$$E_{A2F}^{feat} = (P_{amp} + P_{int} + P_{wavelet}) t_s + \frac{P_{ADC}}{F_s}, \quad (3.1)$$

where P_{amp} , P_{int} , $P_{wavelet}$, and P_{ADC} stand for the power of the amplification stage, the integrator, the wavelet generator, and the ADC, respectively; t_s is a wavelet support size, i.e., the non-zero part's duration of a wavelet producing the respective feature; F_s represents a sampling frequency of the ADC.

To make the first consumption estimations, we borrowed the corresponding values from the state-of-the-art components suitable for our applications (discussed in more detail in Chapter 4). In particular, the power equal to $5.04 \mu\text{W}$ of the amplification stage with a programmable gain designed for a biosensing front-end application-specific integrated circuit (ASIC) from [154] is used as P_{amp} . The G_m -C integrator's power equal to $1.08 \mu\text{W}$ from [155] serves as P_{int} . For $P_{wavelet}$, we use an $8.984 \mu\text{W}$ power consumption estimated during the generation phase of the digital wavelet generator synthesized in XFAB[®] CMOS (Complementary Metal-Oxide-Semiconductor) 180 nm technology for the NUWS-based feature extraction in the A2F converter [11]. Finally, a SAR ADC, also demonstrated in [154], provides P_{ADC} and F_s equal to $0.3 \mu\text{W}$ and 40 kHz, respectively.

For each curve in Figure 3.4, the square marker indicates the point at which the number of extractors required to extract the chosen features reached the allowed maximum $N_{Ext,max}$. For all three values of $N_{Ext,max}$, at certain numbers of features, none of the remaining wavelets fitted the unoccupied intervals within any extractor, forcing the algorithm to stop the search. In the case of $N_{Ext,max} = 1$, the imposed limit of parallel extractors affected the choice of features already from the second feature. Effectively, the only available extractor could not accommodate the feature whose wavelet support overlapped in the analysis window with that of the first feature. Thus, it had to select another less relevant one for the classification task.

The best classifier obtained by the adapted SFS algorithm limited to three feature extractors achieves a 98.33% accuracy and a 94.13% sensitivity with seven extracted features and $8.5 \mu\text{J}$ energy consumption (solid green round marker in Figure 3.4). Our results are close to those previously obtained in [11], where the extraction of six features by three extractors entailed the consumption of $10.9 \mu\text{J}$ to achieve a 98.4% accuracy.

3.1.3.2 Optimized SFS to limit the consumption

To maintain high classification metrics values while reducing consumption, we now apply the optimized SFS algorithm for binary arrhythmia detection. In addition to a limited number of available parallel extractors, this algorithm accounts for the energy cost associated with each feature's extraction by employing the energy-aware metric defined in (2.9) instead of accuracy. We performed the optimized SFS under conditions identical to those of the adapted SFS: the same NN classifiers' internal structure, the same reduced set of input features available for learning, and identical data for consumption estimations. The obtained performances are shown in Figure 3.5.

When limited to three feature extractors, this algorithm achieves a 98.17% accuracy and a 92.61% sensitivity with eight extracted features and $2.6 \mu\text{J}$ energy consumption in a trade-off

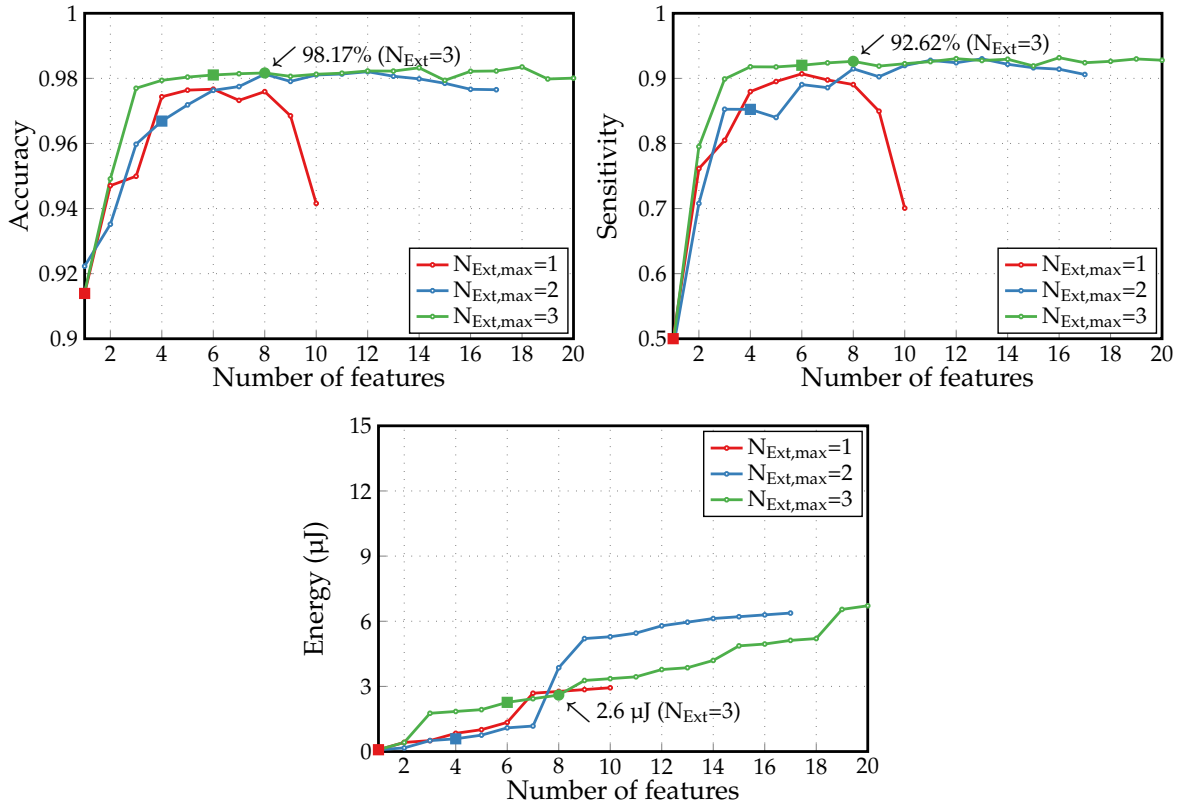


FIGURE 3.5 – Metrics of binary arrhythmia detection performed by NN classifiers with IG + optimized SFS feature selection

point indicated by a solid green round marker. Compared to the adapted SFS, this represents a slight deterioration of accuracy by 0.16% and sensitivity by 1.52%. However, it reduces the energy required during the wavelet generation and feature extraction phases by around 70%.

3.1.4 Discussion on arrhythmia detection

Similar results with the optimized SFS algorithm employing three feature extractors have been obtained in [11]. However, detecting the arrhythmia with a moderately lower accuracy of 98% required extracting two more NUWS-based features, causing an increase in associated energy consumption up to 3.35 μJ . Hence, a slight improvement in obtained classification performance approves the ML algorithms re-implemented using Python with TensorFlow library instead of MATLAB[®]. Therefore, we use our validated simulator further for our second application of the A2F converter in the form of HAR.

Several assumptions and simplifications made during simulations, as well as potential limitations of the proposed approach, must be taken into account. First, the signals issued from the MITDB were already pre-processed with noise filters. Also, the integration considered during simulations represents an approximation of real integration produced in hardware. We address the second question in Chapter 4.

As indicated in Section 2.2.1.1, only the signals from one lead (modified limb lead II in the majority of cases) of possible 12 leads have been used for training and evaluation of our classifiers, potentially limiting the applicability of the proposed approach. Moreover, we have assumed a strict synchronization of each annotated heartbeat segment within the analysis window (see Section 2.2.2.1). Although not yet implemented in this study, the required synchronization system for analog QRS-complex detection and proper R-peak placement can be borrowed from the existing ultra-low power designs [156–158].

3.2 Human activity recognition in inertial signals

Since there are more than two classes in the UCI-HAR dataset, we consider two methods of ADLs’ classification: multi-class and one-vs-all binary HAR. The multi-class classification task simply assigns every input instance to one class out of three or more possible categories. Therefore, a single multi-class HAR classifier defines the final class (WALK, UP, DOWN, SIT, STD, or LAY) of each observation. On the contrary, to arrive at one-vs-all binary classification, we transform the multi-class classification task into multiple binary classification problems. Thus, for each class in the dataset, a separate one-vs-all binary classifier is trained to distinguish that class, labeled as positive, from all other classes, labeled as negative.

The occurrences of all six classes in both training and test sets of the UCI-HAR dataset are relatively equal (see Figure 2.4b), making it balanced for the multi-class classification. Thus, in the multi-class HAR, we evaluate the average performance of our classifiers across all predictions with the help of accuracy. We also supplement this metric with recall and precision by class to provide more detailed information for each class prediction performance when needed.

However, when adapting the relatively balanced multi-class UCI-HAR dataset for six one-vs-all binary classification tasks, the positive target class always has considerably fewer instances than a combined negative class containing all other classes. Due to this strong imbalance between two classes in one-vs-all binary HAR tasks, we employ the *MCC* as a principal metric instead of accuracy to evaluate the performance of such binary classifiers. Where necessary, we also consider sensitivity and specificity to explore the classification performance in detail.

3.2.1 Performance of classifiers with initial settings

We begin training and evaluating the classification models with settings identical to those applied for the arrhythmia detection simulations. Consequently, the feedforward NN classifiers are built with one hidden layer of ten neurons and trained during 1500 epochs using the TensorFlow library. The number of neurons in the output layer, however, depends on the type of classification and is equal to the number of predicted classes – six in multi-class HAR and two in one-vs-all binary HAR. Since HAR is a newly explored application for the

A2F converter with NUWS-based feature extraction, we compare the performance of Haar and Gabor wavelets, two analogously implementable wavelet families, and choose the most suitable for this application.

3.2.1.1 Multi-class classification

Figure 3.6 plots the achieved accuracy of the multi-class HAR performed by NN classifiers with four different configurations, including two types of wavelets to extract the features (Haar or Gabor) and two procedures to select the features (IG or IG + basic SFS). Since LAY is the most frequently occurring class in the test set (see Figure 2.4b), a multi-class ZeroR classifier, serving as a reference, assigns this class to every observation and predicts with an 18.2% accuracy.

Similarly to the arrhythmia detection, before executing the basic SFS, we preliminarily reduced the set available for this algorithm from $247 \times 6 = 1482$ (Haar wavelets) and $552 \times 6 = 3312$ (Gabor wavelets) to 100 best features according to the IG criterion. As expected, combining the IG feature preselection and the basic SFS outperforms the feature selection only with the IG. The classifier utilizing 15 features based on Haar wavelets achieves a 59.31% accuracy, much higher than the ZeroR accuracy albeit significantly lower than an 83.47% accuracy obtained by the classifier requiring 16 Gabor wavelets-based features.

To explore the origin of such a massive discrepancy in the performance of two wavelet families, we compare the confusion matrices of these two particular cases in Figure 3.7. In each cell, the percentage value and, thus, the color mapping are related to the true class. This percentage value represents the recall (sensitivity) for diagonal cells, measured individually for each class according to the definition (1.9a). The individual precision based on (1.9b), i.e., the fraction of relevant instances among those predicted as a given class, is provided below the

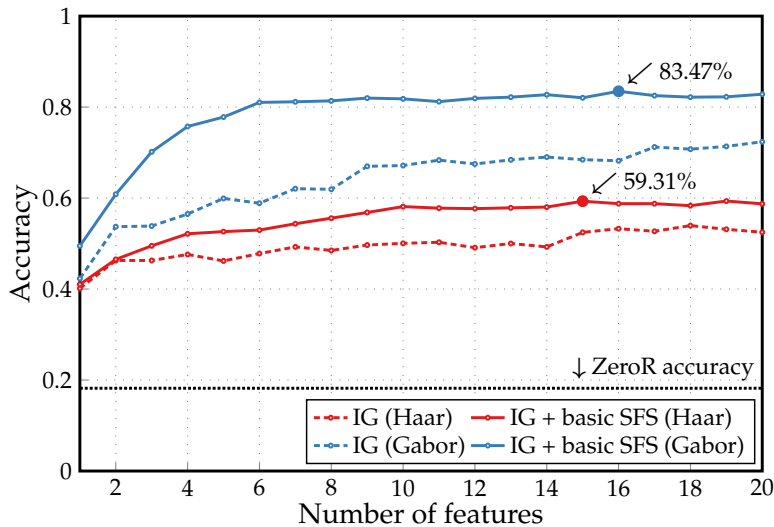


FIGURE 3.6 – Accuracy of the multi-class HAR performed by NN classifiers with initial settings and different wavelet families and feature selection procedures

confusion matrix for complementary information. The classifier with Haar wavelets heavily confuses static ADLs (SIT, STD, and LAY) between them. Mainly, it predicts incorrectly when categorizing the observations belonging to SIT and STD by assigning them to the class LAY. As a result, the individual sensitivities of SIT and STD classifications drop to 3.7% and 33.5%, respectively. We investigate the reason for this issue and tackle the resultant decrease in classification efficiency after presenting the results of one-vs-all binary HAR.

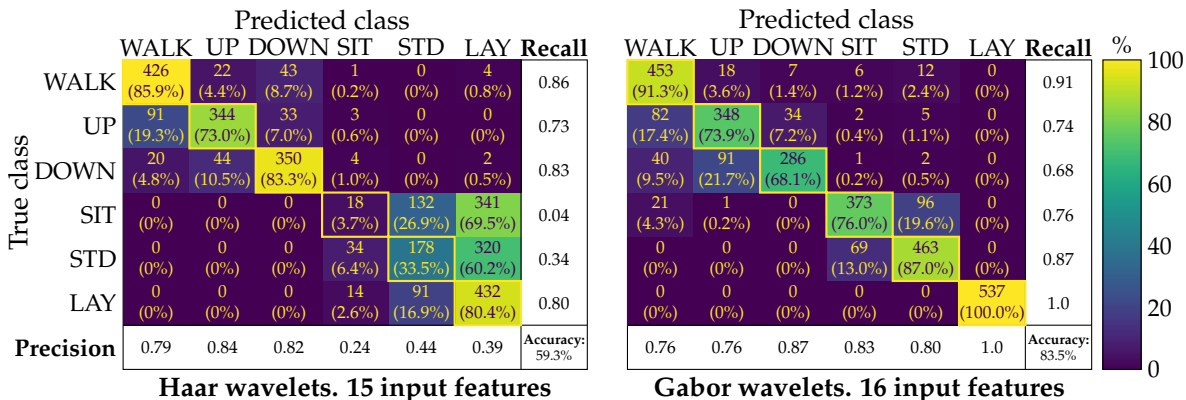


FIGURE 3.7 – Confusion matrices of two preferred NN classifiers performing the multi-class HAR with different wavelet families and IG + basic SFS feature selection

3.2.1.2 One-vs-all binary classification

Performing six one-vs-all binary HAR classifications with the combination of the IG feature preselection and the basic SFS algorithm, we obtained the *MCC* plots shown in Figure 3.8.

Again, classifiers built on features extracted from inertial signals with the help of Gabor wavelets rather than their Haar counterparts produce better results when classifying any static ADL against all other classes. In the case of Haar wavelets-based features (demonstrated in Figure 3.8a), SIT-vs-ALL, STD-vs-ALL, and LAY-vs-ALL classifiers with less than a certain number of input features even show undefined *MCC* values. This is caused by the denominator in equation (1.6) turning to zero since either *PP* or *PN* are equal to zero, which indicates that the corresponding classifiers fail to differentiate between two classes and, thus, predict the same class for all instances. Although the *MCC* score showed that the binary classifications employing Haar wavelets and distinguishing static ADLs are overall unsuccessful with any number of input features up to 20, it cannot explain why they failed. Hence, we address sensitivity (*TPR*) and specificity (*TNR*) to delve into details. For this purpose, we draw the receiver operating characteristic (ROC) curves [159] that can visualize these two metrics simultaneously for each binary classifier.

The raw output of a binary NN classifier is a value between zero and one, which represents the probability that the input observation belongs to the positive class. This raw output is converted into a prediction by setting an arbitrary classification threshold: observation is assigned to the negative class if its raw output is lower than the threshold; otherwise, it is

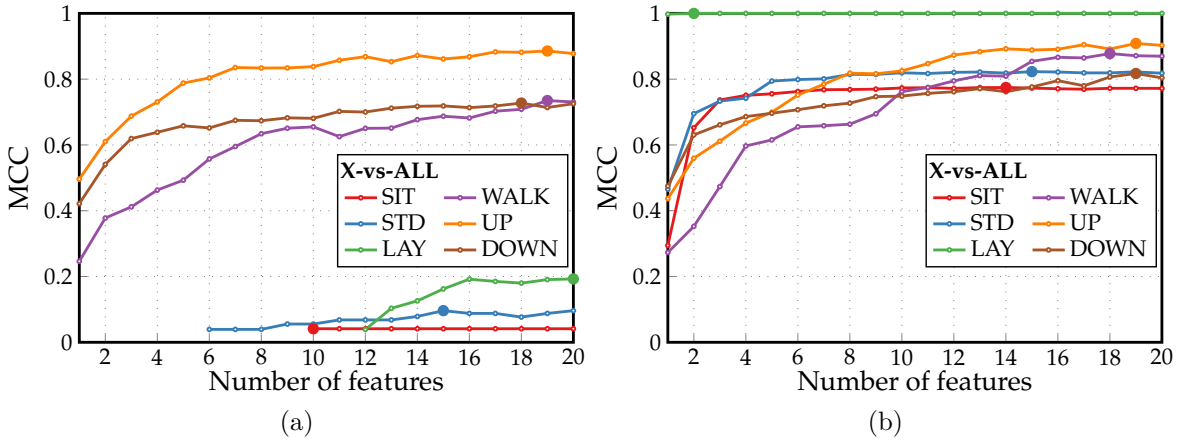


FIGURE 3.8 – MCC of one-vs-all binary HAR performed by NN classifiers with IG + basic SFS feature selection and different wavelet families: (a) Haar wavelets; (b) Gabor wavelets

assigned to the positive class. The performances of NN classifiers demonstrated in Figure 3.8 correspond to this threshold set to a default 0.5 value. However, in the ROC curves, sensitivity is drawn against $FPR = 1 - TNR$ in the entire $[0; 1]$ range of threshold values. A classification model is perfect at a given threshold if it predicts with 100% sensitivity and specificity, displayed by a $(0, 1)$ point in the ROC's axes.

Figure 3.9 shows the ROC curves for all six one-vs-all binary classifiers that achieved the highest MCC score in Figure 3.8 (solid round markers). The TPR (sensitivity) and FPR of distinguishing any static ADL from other classes with the help of Haar wavelet-based features are close or equal to zero when the classification threshold is set to 0.5. This means that the respective classifiers attribute almost all observations of the test set to a negative class ($PP = TP + FP \approx 0$ and $PN \approx P + N$, see Figure 1.5a) containing all five other classes. High specificity and, thus, low FPR are expected values since the negative class prevails with more

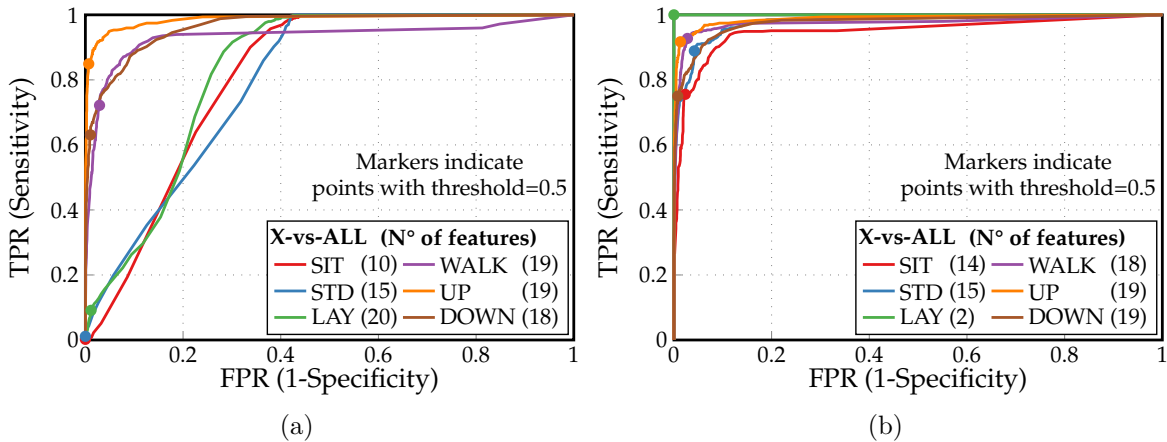


FIGURE 3.9 – ROC curves of one-vs-all binary HAR performed by NN classifiers with IG + basic SFS feature selection and different wavelet families: (a) Haar; (b) Gabor

than 80% occurrence in training and test sets of all six one-vs-all binary classifiers, according to Figure 2.4. However, binary classifiers with extremely low sensitivity values can practically not identify the positive class observations. Such classifiers are hardly better or even worse than ZeroR classifiers and can be considered useless.

3.2.2 Improved performance of multi-class classifiers with the basic SFS

As seen above, both multi-class and binary one-vs-all HAR classifiers employing features from Haar wavelets generally performed poorly while predicting the classes of static ADLs. Nevertheless, Haar wavelets are preferable for the hardware implementation of the developed A2F converter. We prefer to keep using them for the NUWS-based feature extraction, as done previously in binary arrhythmia detection. Therefore, to enhance the performance of these classifiers, we need to make changes in the process of wavelet dictionary generation or modify the NN classifiers' initialization settings or structure. In the next section, we first implement these improvements for the multi-class HAR performed by NN classifiers with the basic SFS algorithm. Next, we apply the configuration of settings we obtained to both types of constructed classifiers – multi-class and binary – with the adapted SFS.

3.2.2.1 Adjustments in wavelet dictionaries and NN initialization

First, we noticed that all static ADLs (SIT, STD, and LAY) are naturally characterized by relatively constant acceleration and angular velocity values. Whereas, as explained in Section 2.3.2 and shown in Figure 2.8, any Haar wavelet is an inherently zero average function taking both 1 and -1 values each in total during precisely half of its support size. Thus, the result of integrating such nearly constant inertial signals with any Haar wavelet tends to be zero. Subsequently, the features produced this way are irrelevant for classifying static activities since they cannot distinguish them from each other.

Hence, we improved the initial wavelet dictionaries by introducing an additional "constant" wavelet with a unitary value across the entire analysis window. This wavelet corresponds to the scale function shown in Figure 2.6 with $\xi_1(t) = 1$ within the analysis window and $\xi_1(t) = 0$ outside it. The extraction of NUWS-based features produced by the "constant" wavelet does not require the wavelet generator. Indeed, the concerned signal is directly integrated within the whole analysis window, resulting in a value proportional to the signal's average. However, this wavelet occupies all the available intervals in one feature extractor, which thus cannot accommodate any more wavelets to extract more features.

In Figure 3.10, the blue curve corresponds to the accuracies achieved by the multi-class NN classifiers with the adapted SFS and improved Haar wavelet dictionary. The introduction of the "constant" wavelet significantly influenced the feature selection process, leading to a considerable enhancement in classification performance. Effectively, compared to the classifier employing the default Haar wavelet dictionary and indicated by a solid red round marker, the highest achieved accuracy rose by more than 23% to 82.93% for the same number of input

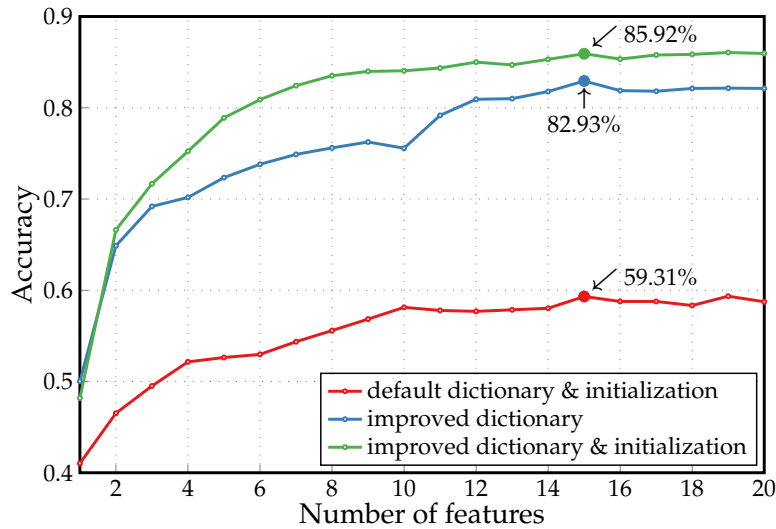


FIGURE 3.10 – Impact of improved dictionaries and NN initialization on the multi-class HAR performed by NN classifiers with Haar wavelets and IG + basic SFS feature selection

features equal to 15. Among these newly selected features, two were extracted with the help of the "constant" wavelet from the x- and y-axes of acceleration signals.

To improve the classification accuracy further, we studied the modification of the kernel and bias initializers in the trained NNs. These initializers set the initial values of the weights and biases in an NN layer, respectively, according to statistical distribution or function. Since it can affect convergence and overall performance, proper initialization is crucial for the effective training of NNs. TensorFlow sets the kernel and bias initializers by default to "glorot uniform" and "zeros". We achieved the best classification performance experimentally by switching both initializers in the NN's hidden layer to "random uniform". The accuracies of the corresponding classifiers are shown in green in Figure 3.10. The highest accuracy increased by almost 3% to 85.92%. Similar to the classifier with default initializers, this accuracy was also achieved with 15 extracted features, which included the same two features produced with the help of the "constant" wavelet from the x- and y-axes of acceleration signals.

Figure 3.11 displays the confusion matrices of the best NN classifiers obtained by these two improvement steps. Compared to the classifier with default settings (shown in Figure 3.7 on the left), the one with an improved dictionary significantly raised the individual sensitivities of static ADLs' classification, especially of SIT and STD, but reduced the individual sensitivity of DOWN classification from 83.3% down to 65.7%. However, the NN classifier with improved initialization of weights and biases in the hidden layer managed to increase the individual sensitivities of UP, DOWN, and STD classifications by 0.6%, 18.8%, and 2.6%, respectively, albeit a slight decrease in WALK's classification sensitivity by 1.6%. Hence, we keep this configuration of wavelet dictionary and initializers for further HAR simulations.

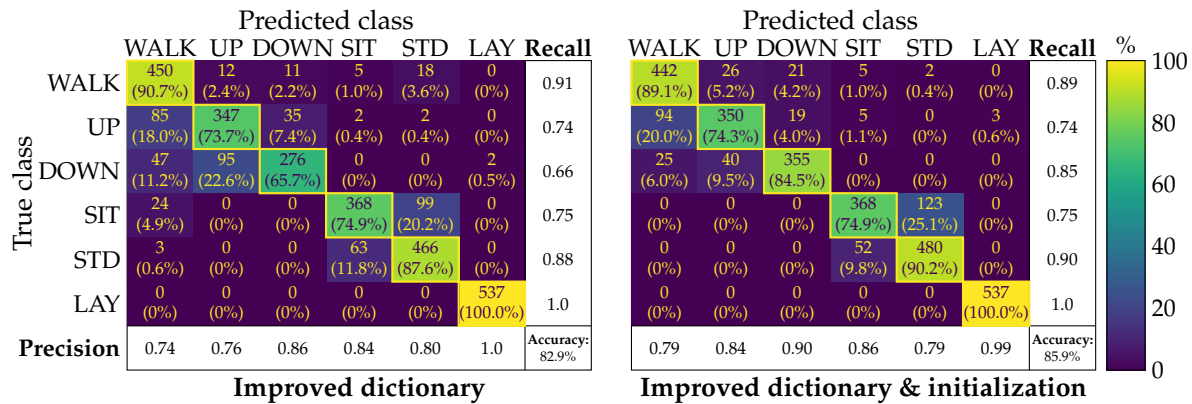


FIGURE 3.11 – Confusion matrices of two improved NN classifiers with 15 input features performing the multi-class HAR with IG + basic SFS feature selection

3.2.2.2 Choice of NN structure and wavelet family

Moving forward, we examined different internal structures of NN classifiers performing the multi-class HAR with the basic SFS: one hidden layer of ten neurons (1×10), two hidden layers of ten neurons (2×10), and one hidden layer of 20 neurons (1×20). Figure 3.12 illustrates the obtained accuracies. The preferable configuration with one hidden layer of 20 neurons achieves an 88.12% accuracy with 17 features extracted by ten extractors (solid green round marker). We also checked this configuration with Gabor wavelets, which were much more effective than Haar wavelets when training classifiers with a 1×10 hidden layer structure, default dictionaries, and default NN initialization. However, Gabor wavelets yield a worse classification performance here with the improved dictionary, initialization, and hidden layer structure, achieving an 87% accuracy with 20 extracted features, as shown by the green dashed curve in Figure 3.12.

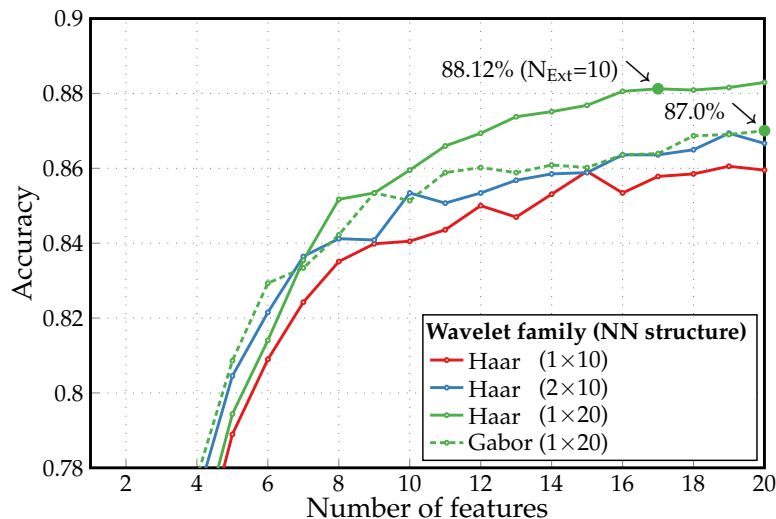


FIGURE 3.12 – Accuracy of the multi-class HAR performed by NN classifiers of different structure with different wavelet families and IG + basic SFS feature selection

In Figure 3.13, we compare the confusion matrices of NN classifiers that used two wavelet families and were obtained in the features/accuracy trade-off points mentioned above. Due to similar local shapes of inertial measurements' time series corresponding to SIT and STD, there is substantial confusion between these static ADLs, which is noticeable in both matrices. The classifier employing Haar wavelets provides the individual sensitivities of UP and DOWN classifications higher than its counterpart with Gabor wavelets by 1.9% and 6.7%, respectively. The performance indicators of the remaining four ADLs (WALK, SIT, STD, and LAY) are similar in both classifiers. Therefore, we continue to use Haar wavelets, which are also advantageous in the hardware implementation of the developed A2F converter. Next, we apply them and the obtained configuration of improved settings (dictionary, NN initializers, and NN structure) to build the classifiers with the adapted SFS.

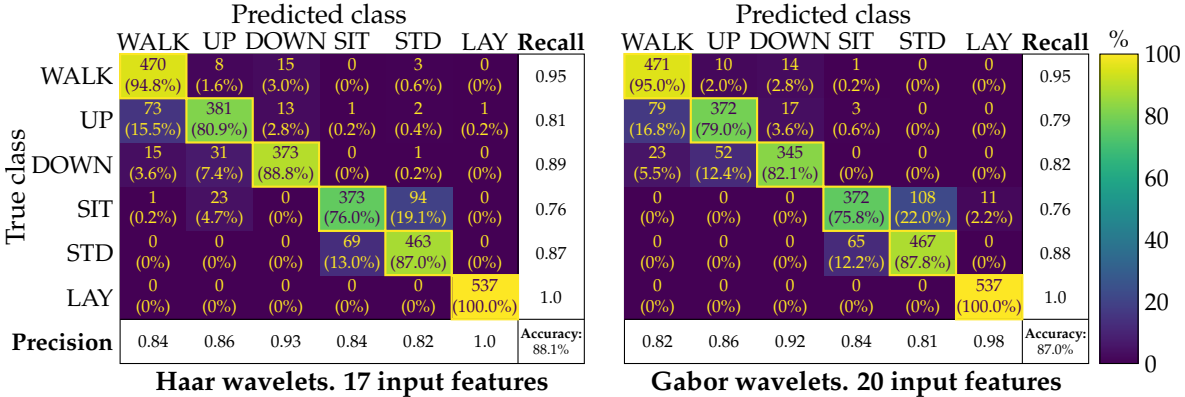


FIGURE 3.13 – Confusion matrices of NN classifiers using different wavelet families and performing the multi-class HAR with IG + basic SFS feature selection in the features/accuracy trade-off points

3.2.3 Adapted SFS to limit the number of extractors

This section presents the results of the multi-class and binary one-vs-all HAR classifications performed with the adapted SFS algorithm. The NN classifiers employ features from Haar wavelets with the improved dictionary (includes the "constant" wavelet) and use a hidden layer with a 1×20 structure, as well as non-default "random uniform" kernel and bias initializers.

3.2.3.1 Multi-class classification

Executing the multi-class HAR with the adapted SFS and different values of a maximum number of extractors ($N_{Ext,max} = 5, 7, 8, 10$) produced the accuracy curves depicted in Figure 3.14. Square markers indicate where the number of extractors necessary to extract the chosen features reached the corresponding $N_{Ext,max}$ values on all four curves. Notably, the case with $N_{Ext,max}$ set to ten, yields an accuracy lower by 0.3% (87.82%, 15 extracted features) than the classifier with the basic SFS that requires ten extractors, too (88.12%, 17

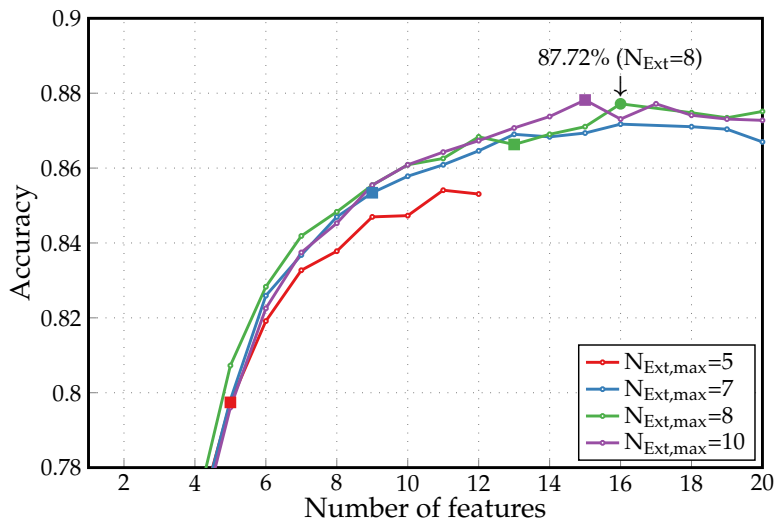


FIGURE 3.14 – Accuracy of the multi-class HAR performed by NN classifiers with Haar wavelets and IG + adapted SFS feature selection

features, see Figure 3.12). The reason lies in the random initialization of the weights and biases when training NN classifiers. This impacts the performance of different feature subsets obtained after their learning during a limited number of epochs and thus affects the choice of features added afterward to the target set. Moreover, we achieved a slightly lower classification accuracy of 87.72% with the help of 16 features that require two fewer extractors (solid green round marker in Figure 3.14).

Analyzing the features retained by this trained classifier, we discovered that only x- and y-axis acceleration ($acc_{x,y}$) and z-axis angular velocity (gyr_z) signals produced them. Also, only two features have been extracted from the gyroscope’s gyr_z signal. Therefore, we also performed the multi-class HAR with the adapted SFS by training and evaluating the NN classifiers with input data consisting exclusively of features produced from three-axial accelerometer signals ($acc_{x,y,z}$). The obtained classification performances are illustrated in Figure 3.15. To achieve an 87.75% accuracy, which is comparable to that seen in the case utilizing both types of available inertial signals (87.72%), this case, however, extracts four more features and needs two more extractors to accommodate them in a single analysis window (solid violet round marker). Nevertheless, extracting 17 features from $acc_{x,y,z}$ signals by eight extractors, the same number as before, ensures the classification with a moderate loss in accuracy – down to 87.17% (solid green round marker). Therefore, in the multi-class HAR, we can limit ourselves to one type of inertial sensor, accelerometers, without significant loss in classification performance.

3.2.3.2 One-vs-all binary classification

MCC plots in Figure 3.16 demonstrate the result of performing one-vs-all binary HAR classifications with the adapted SFS algorithm. Although we tested different values for the

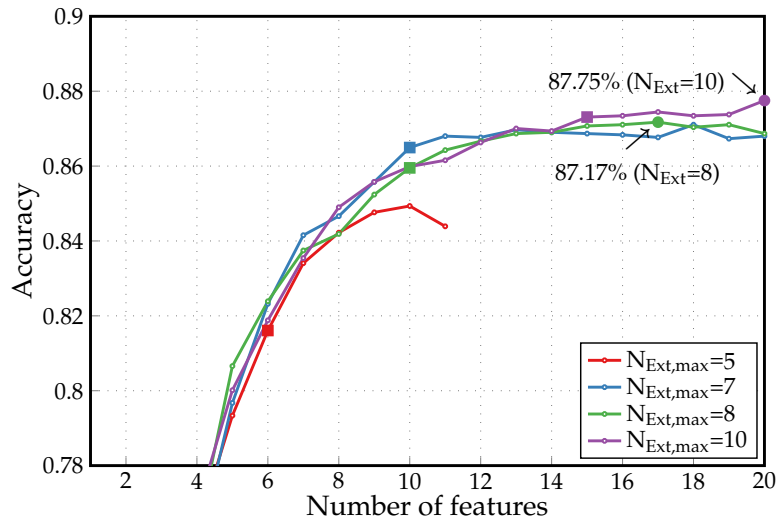


FIGURE 3.15 – Accuracy of the multi-class HAR performed by NN classifiers with Haar wavelets, features extracted from acceleration signals, and IG + adapted SFS feature selection

maximum number of parallel extractors $N_{Ext,max}$, this Figure shows only the best cases for each binary classification. Since a single feature extracted from the x-axis acceleration signal by the "constant" wavelet is enough to build a perfect classifier distinguishing LAY class from all other activities, we did not plot the MCC values of the LAY-vs-ALL classification. Solid round markers indicate the trade-off points between the number of selected features and the achieved MCC score in every curve.

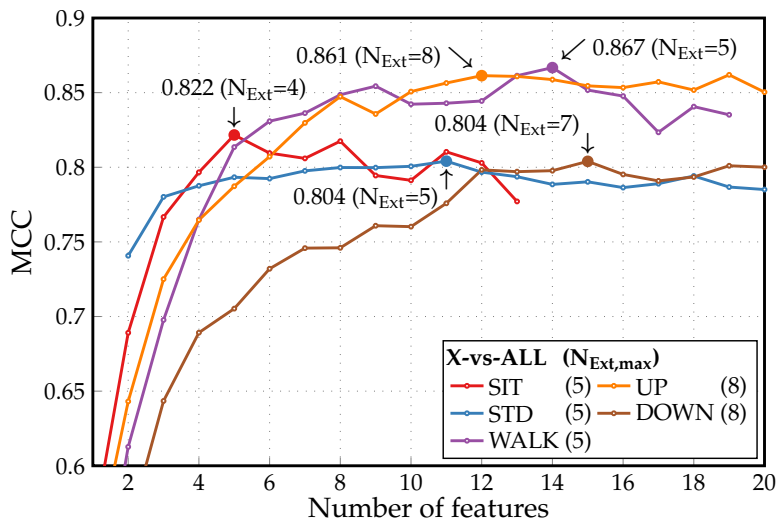


FIGURE 3.16 – MCC of one-vs-all binary HAR performed by NN classifiers with Haar wavelets and IG + adapted SFS feature selection

3.2.3.3 Comparison of binary and multi-class classifiers

We can now compare six binary one-vs-all classifiers obtained in these trade-off points to the multi-class classifiers from Figure 3.14 ($acc_{x,y}$, gyr_z) and Figure 3.15 ($acc_{x,y,z}$) regarding MCC values. Since the MCC metric evaluates binary classification problems, we converted corresponding multi-class confusion matrices into six individual binary confusion matrices for each class to calculate MCC score per each ADL. As seen from Table 3.1, even though binary one-vs-all classifiers are specifically trained to distinguish between a specific ADL and the rest, they only perform considerably better in two cases: UP- and SIT-vs-ALL classifications. The difference in average MCC values between multi-class and binary classifiers is insignificant.

TABLE 3.1 – Comparison of MCC values obtained by multi-class and binary HAR classifiers

Classification type	MCC per class						Average MCC
	WALK	UP	DOWN	SIT	STD	LAY	
Multi-class:							
• features from $acc_{x,y} + gyr_z$	0.866	0.798	0.858	0.765	0.817	1.0	0.851
• features from $acc_{x,y,z}$	0.838	0.821	0.849	0.763	0.799	1.0	0.845
Binary (X-vs-ALL)	0.867	0.861	0.804	0.822	0.804	1.0	0.860

However, binary classification is far less common in the HAR field than its multi-class counterpart. Moreover, the distinction of all six ADLs from each other requires six different binary one-vs-all classifiers and more features and extractors in total, as shown in Table 3.2, summarizing the performance of the multi-class and binary classifiers achieved in the trade-off points. All classifiers except DOWN-vs-ALL necessitate at least one feature produced with the help of the "constant" wavelet. Therefore, besides regular extractors comprising wavelet generators, such classifiers require those implementing direct integration of the input signal within the analysis window.

TABLE 3.2 – Performance summary of multi-class and binary HAR classifiers

Classification type	Binary (X-vs-ALL)						Multi-class	
	WALK	UP	DOWN	SIT	STD	LAY		
Nb. of features	14	12	15	5	11	1	16	17
Metrics:								
• MCC	0.867	0.861	0.804	0.822	0.804	1.0	0.851*	0.845*
• Accuracy (%)	not calculated (due to high class imbalance)						87.72	87.17
Nb. of extractors:								
• with wav. gener-s	5	8	7	4	5	1	8	
• with direct \int	4	7	7	2	4	0	6	
	1	1	0	2	1	1	2	

* Average of MCC scores from six classes

3.2.4 Discussion on human activity recognition

Our multi-class HAR classifiers with 16 input features from $acc_{x,y}$, gyr_z signals and 17 input features from $acc_{x,y,z}$ provide lower accuracies on the UCI-HAR dataset than the state-of-the-art CNN, LSTM models, and their hybrids. Table 3.3 compares our classifiers to the models with the highest accuracy [104], the smallest number of inputs [101], and the fewest model parameters [116]. Although showing considerably lower accuracies, our classifiers require more than one hundred times fewer parameters than [116] and 23 times smaller classification model input size than [101]. Currently obtained order of the multi-class HAR accuracy may suffice for non-critical applications. However, if necessary, it is still possible to enhance accuracy and reliability by acquiring additional types of signals and enabling multi-sensor data fusion [52, 160] and distributed event detection [161]. Feature stacking may also be applied to improve the predictive performance by combining the predictions from several ML models, thus benefiting from each model’s strengths.

TABLE 3.3 – Comparison of different classification models performing multi-class HAR on the UCI-HAR dataset

Classification model	Accuracy (%)	Model input size	Nb. of model parameters
4 layer CNN-LSTM [104]	99.39	768 = $3 \times 2 \times 128$:	~1.48M
LSTM-CNN [116]	95.78	three axes for acc and gyr	0.05M
CNN with stat. features [101]	97.63	384 = $3 \times 1 \times 128$: three axes for acc	~6.44M
This work: Feedforward NN (1 hidden layer of 20 neurons)	87.72	16 features from 3 signals: acc_x, acc_y, gyr_z	466
	87.17	17 features from 3 signals: acc_x, acc_y, acc_z	486

Either of our two simple feedforward NNs performing the multi-class HAR can be implemented through digital architecture within the sensor node rather than at the aggregator. Since only the classification results are sent in this case, it will help cut down further on sensor energy usage induced by wireless transmission. Furthermore, employing analog memristor-based, reconfigurable NN [162–165] will enable digitizing strictly the classifier’s output while providing the application- or context-specific adaptation.

However, similar to the arrhythmia detection case, we have to account for assumptions and simplifications made during simulations for this application. The inertial signals issued from the UCI-HAR dataset also underwent an initial noise preprocessing. Second, just as during the training and evaluation of arrhythmia detection classifiers, the integration process performed to extract the NUWS-based features for HAR classifiers represents an approximation of real integration produced in hardware.

It is also critical to acknowledge the constraints imposed by using specifically the UCI-HAR dataset to build HAR classification models. Besides the narrow variety of activities

restricted to six ADLs, these include their low representativeness caused by ranges of values, such as stride frequency and stair step height in dynamic ADLs, limited by the experiment conditions. In addition, it is essential to account for multiple heterogeneities arising from various possible software, hardware, and data acquisition configurations in inertial motion-based HAR systems [98]. At the same time, the UCI-HAR dataset signals were collected from a specific body location by a specific model smartphone with a specific operating system and embedded inertial sensors.

HAR application scenarios for healthcare purposes in WBANs highlight the potential of the A2F converter's implementation in real-time systems [166], e.g., performing urgent fall detection in elderly people. However, the analysis window duration set to 2.56 s in the UCI-HAR dataset results in a relatively long minimum response time of our system and, thus, limits the study to offline models. Hence, future research with the same dataset may be directed towards adequately reducing the analysis window length based on the duration of corresponding human activities [167] to explore the system's real-time perspectives and capabilities. Alternatively, another suitable dataset may be studied, such as the recently released comprehensive multimodal wearable sensor-based CSL-SHARE dataset [168] with a wider variety of ADLs and biosignals useful for HAR purposes.

3.3 Conclusion

This Chapter presents the results of training and evaluating classification models built separately for each of the two studied applications using Python with Scikit-Learn and TensorFlow libraries. It follows the methodologies of data preparation, feature extraction, feature selection, and classification outlined in Sections 2.2, 2.3, 2.4, and 2.5, respectively.

In binary arrhythmia detection, we begin with training different classifiers (RF, SVM, and NN) upon the features produced from Haar wavelets and sorted in the order directly provided by one of the two exploited filter methods (FS or IG). As a result, the combination of the IG criterion and the NN classifier with one hidden layer of ten neurons outperforms other combinations. Using the TensorFlow library, which enables more efficient training of NNs on GPUs, also improves the classification performance. Next, this configuration is used for further simulations that benefit from the SFS algorithm, which automatically selects features according to the metric depending on the classification model's performance. Namely, we evaluate the NN classifiers built with the basic, adapted, and optimized SFS algorithms. The basic SFS is intended to select features that simply maximize the classification accuracy. The adapted SFS additionally limits the available number of extractors that accommodate the chosen features. The optimized SFS also accounts for the energetic cost of extracted features. The final NN classifier obtained with the optimized SFS algorithm achieves a 98.17% accuracy with 2.6 μ J energy consumption. In this case, our A2F converter needs only eight features extracted from the entire period of the ECG signal with the help of three parallel extractors instead of the

256 samples required for uniform Nyquist-rate sampling. This reduction corresponds to a 96.9% compression of the number of signal samples/features intended for transmission.

In HAR, we study two methods – multi-class and one-vs-all binary classification – and begin with training and evaluating the NN classifiers with the basic SFS and settings (NN’s internal structure, number of epochs) identical to those set as final in arrhythmia detection simulations. However, to improve the achieved classification performances, we ultimately modify the wavelet dictionary, the NN initialization parameters, and the NN’s internal structure. Based on classifiers obtained with the adapted SFS, we consider the multi-class HAR a preferable method to its binary counterpart due to greater prevalence in the HAR field and lower implementation complexity at similar performance levels. To achieve an 87.72% or 87.17% accuracy in our final multi-class HAR NN classifiers (one hidden layer of 20 neurons), the A2F converter needs 16 or 17 features extracted from three inertial signals ($acc_{x,y} + gyr_z$, or $acc_{x,y,z}$) composed of $384 = 3 \times 128$ samples in total with the help of eight parallel extractors instead of all 384 samples required for uniform Nyquist-rate sampling. This reduction corresponds to a 95.8% or 95.6% compression of the number of signal samples/features intended for transmission, a similar outcome to the binary arrhythmia detection case.

In the next Chapter, eight and 16 features considered relevant for corresponding binary arrhythmia detection and multi-class HAR NN classifiers, respectively, serve to derive the specifications required for the hardware design of the generic A2F converter embracing at least these two applications.

Chapter 4

Hardware design of the Analog-to-Feature converter

A2F conversion shows high potential in improving sensor autonomy for applications dealing with classification. This Chapter paves the way towards the complete circuit design of the generic A2F converter based on the classification-relevant features identified in Chapter 3 during separate modeling of NN classifiers for two studied applications: binary arrhythmia detection in ECG signals and multi-class HAR in accelerometer and gyroscope signals.

First, we deduce the hardware specifications and review the existing state-of-the-art solutions for principal blocks constituting the developed A2F converter. This step allows us to select the appropriate technology node and architectures for these components that fulfill the defined specifications.

Second, we present the simulations on the circuit level of the G_m -C integrator, a critical component of the A2F converter, based on the design found in the literature. We define its biasing and control voltages to achieve a specified cut-off frequency that should be low enough to suit both explored applications.

Third, we evaluate our NN classifiers using more realistic non-ideal integration coefficients, i.e., features produced at the outputs of the simulated G_m -C integrator in transient analysis. This procedure helps to verify whether classification algorithms can learn and accommodate the non-idealities introduced by at least such analog circuits as integrators.

Fourth, with a revised value of the integrator's power consumption, we compare the energetic efficiency of our communication chain to those based on Nyquist and A2I approaches to show the benefits of using the A2F conversion in WBAN sensors with a continuous signal nature. Moreover, we compare the performance of our system employing the in-sensor classification to recent embedded designs.

4.1 Required specifications

4.1.1 Overall architecture of the acquisition system

As a part of the intelligent acquisition system shown in Figure 2.1, our generic A2F converter requires eight parallel feature extractors to accommodate both explored applications. According to the results obtained in the previous Chapter, only three extractors are sufficient for binary anomaly detection in ECG signals with a 98.17% accuracy. Meanwhile, for multi-class HAR achieving 87.72% or 87.17% accuracy, extracting 16 or 17 chosen features from inertial signals requires all eight extractors. To satisfy the most demanding case – the multi-class HAR based on $acc_{x,y} + gyr_z$ signals – the A2F converter contains six regular (with wavelet generation) and two basic (with direct integration) feature extractors. Figure 4.1 displays a possible hardware implementation of the acquisition system with the A2F converter suitable for the two studied applications. Therefore, the principal components of the feature extraction and digitization chain are the amplification stage, the wavelet generator, the analog mixer, the G_m -C integrator, and the ADC.

For the developed A2F converter to be able to adapt to different types of signals between different applications and to reconfigure on the go within the scope of the same application, e.g., to perform a profound classification after a coarse binary anomaly or event detection, it is desirable to equip the inputs of feature extractors with multiplexers that can select appropriate inputs from available analog signals, such as three-axial acceleration and angular velocity in the HAR task. Instead of equipping each extractor’s input with an individual multiplexer, we

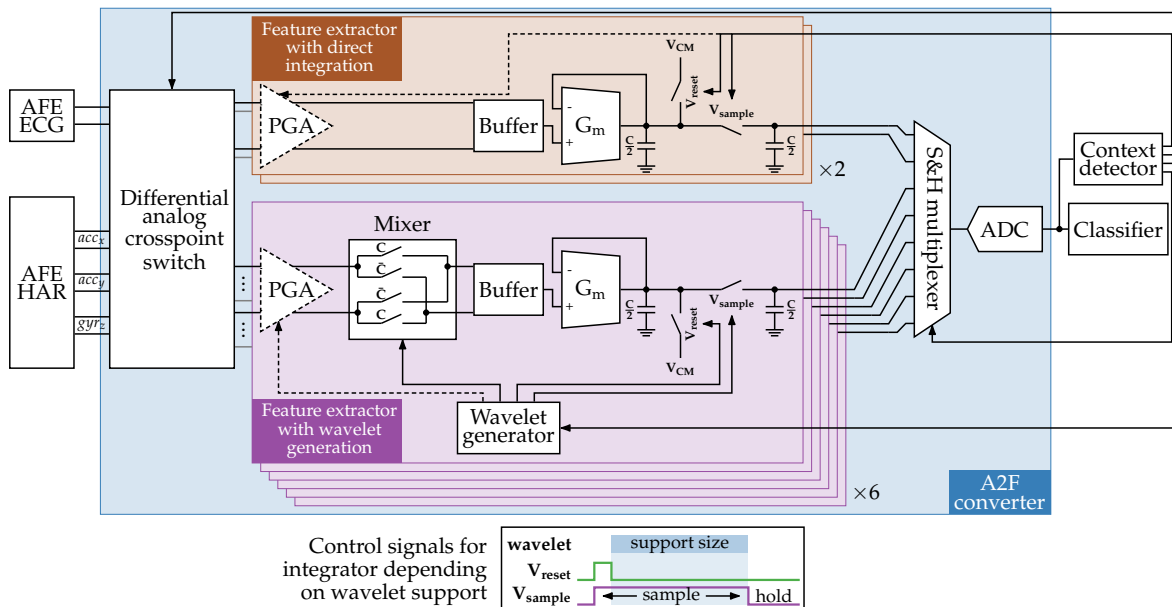


FIGURE 4.1 – Hardware implementation of the acquisition system with the A2F converter satisfying the two studied applications

can follow a more universal approach with a differential analog crosspoint switch. This circuit represents a matrix of switches that route multiple analog input signals to multiple outputs. However, careful routing is required to maintain signal integrity and prevent common-mode noise. In our converter, this switch, yet not implemented in the thesis, would be controlled by the context detector and consist of four differential inputs and eight differential outputs.

At the bottom of Figure 4.1, we schematically illustrate the time diagrams of control signals V_{reset} and V_{sample} provided for integrators. Within the duration of the analysis window, these voltages open and close two switches at moments depending on the support of a given wavelet. When V_{reset} is high, the integrator's output is re-initialized to a common-mode voltage value V_{CM} . When V_{sample} is high, the sampling takes place, the integrator's output is connected to the multiplexer's input, and their capacitors $\frac{C}{2}$ share the same voltage. Right before the beginning of the wavelet support, V_{reset} is released, and then the integrator's input voltage begins to integrate on a total capacitance of C . At the end of wavelet support, V_{sample} resets to zero, and the multiplexer's input capacitor is disconnected from the integrator's output to hold the accumulated voltage, which represents the unprocessed extracted feature value.

Within one analysis window, equal to 0.711 s and 2.56 s in the arrhythmia detection and the HAR tasks, respectively, the A2F converter extracts all the required NUWS-based features. Some extractors produce multiple features within the duration of a single window. For example, the distribution of 16 chosen features across eight extractors in the case of the multi-class HAR based on mixed inertial signals $acc_{x,y} + gyr_z$ is shown in Table 4.1. The extractors numbered 2, 3, 5, 6, and 8 accommodate two or three features produced by the non-overlapping wavelets. Hence, the output multiplexer, which routes feature extractors'

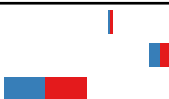







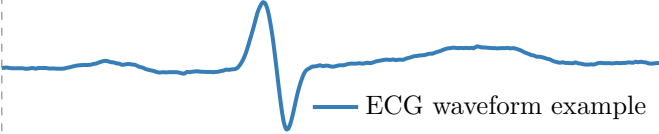
TABLE 4.1 – Features selected for extraction in the multi-class HAR from $acc_{x,y} + gyr_z$ signals

Extractor number	Input signal	Wavelet that produces the feature (■ ⇒ "1", ■ ⇒ "-1")	Feature relevance (according to SFS)
1	acc_y	[0, 2.56]	1
2	acc_x	[0.711, 1.422] (blue), [1.422, 2.133] (red)	2
	acc_y	[0.711, 1.422] (blue), [1.422, 2.133] (red)	10
3	acc_x	[1.422, 2.133] (blue), [2.133, 2.844] (red)	15
	acc_x	[1.422, 2.133] (blue), [2.133, 2.844] (red)	3
4	acc_x	[0, 0.711] (blue), [0.711, 1.422] (red), [1.422, 2.133] (blue), [2.133, 2.844] (red)	8
	acc_x	[0, 0.711] (blue), [0.711, 1.422] (red), [1.422, 2.133] (blue), [2.133, 2.844] (red)	12
5	acc_x	[0.711, 1.422] (blue), [1.422, 2.133] (red)	4
	gyr_z	[0.711, 1.422] (blue), [1.422, 2.133] (red)	14
6	acc_x	[1.422, 2.133] (blue), [2.133, 2.844] (red)	5
	acc_x	[1.422, 2.133] (blue), [2.133, 2.844] (red)	11
7	acc_x	[1.422, 2.133] (blue), [2.133, 2.844] (red)	6
	acc_x	[1.422, 2.133] (blue), [2.133, 2.844] (red)	9
8	acc_y	[0, 0.711] (blue), [0.711, 1.422] (red), [1.422, 2.133] (blue), [2.133, 2.844] (red)	6
	acc_y	[0, 0.711] (blue), [0.711, 1.422] (red), [1.422, 2.133] (blue), [2.133, 2.844] (red)	7
8	acc_y	[0.711, 1.422] (blue), [1.422, 2.133] (red)	16
	gyr_z	[0.711, 1.422] (blue), [1.422, 2.133] (red)	13

outputs to a single ADC, has to handle not only multiple features provided by parallel extracting branches but also several features that appear sequentially for a limited duration at the same multiplexer’s inputs.

To satisfy these needs and to send all extracted features one by one to the ADC, we need a so-called S&H multiplexer. This circuit should combine internal analog storage and multiplexing by temporarily storing its analog inputs sampled at specific times and then selectively routing them to its output based on control signals provided by the context detector. According to Table 4.1, the shortest time that one multiplexer’s input should store the same value before the arrival of the next one is 640 ms (11.1 ms in the binary arrhythmia detection case, according to Table 4.2). However, since six features are extracted at the end of the analysis window, the shorter the minimum possible storage time, the better for faster processing of features and a real-time A2F converter’s applicability. Nevertheless, we have not addressed the details of implementing the S&H multiplexer in this thesis. From Table 4.2, we notice that features considered relevant for arrhythmia detection are extracted at specific moments around the QRS complex, similar to traditional, for this application, interpretable features. Thus, the classification performance may be sensitive to R-peak synchronization precision.

TABLE 4.2 – Features selected for extraction in the binary arrhythmia detection

Extractor number	Wavelet that produces the feature (■ ⇒ "1", ■ ⇒ "-1")	Feature relevance (according to SFS)
1		1
		2
		3
2		4
		5
3		7
		8
		6
	0 Time (ms) 711	
		

4.1.2 Feature extraction

Using a differential signal conditioning circuitry, including the differential amplification stage, is crucial for the developed A2F converter in targeted WBAN sensors, especially when capturing biopotential signals due to highly sensitive skin-electrode contacts. Indeed, it enhances signal quality, reduces offset potentials, and improves noise rejection and immunity to interference from the environment and power supplies. To process at least the two studied types of signals – single-channel ECG recordings and three outputs from inertial sensors – the amplification stage should have a variable gain offered by a combination of a Low Noise

Amplifier (LNA) and a Programmable Gain Amplifier (PGA). The LNA can be a part of the AFE that performs the signal conditioning. The PGA can also be in the AFE or optionally included in the feature extractor circuit to adjust the gain depending on the application or signal type. Nevertheless, if commercially available three-axial analog output accelerometers (as well as a z-axis gyroscope if needed), for example, from Analog Devices [169], are used to provide inertial measurements for the HAR task, amplification may not be necessary, as their outputs are ratiometric to reference voltages ranging from 1.8 V to 6 V.

Designing the A2F converter with NUWS-based feature extraction that employs Haar wavelets, first and foremost, facilitates the implementation of wavelet generators thanks to their entirely digital structure. Additionally, it simplifies the analog mixer to four switches. Indeed, since Haar wavelets take values 1 or -1 within their support, the mixing process consists of mere inversion or non-inversion of positive and negative outputs of the differential amplification stage before integration. CMOS switches composed of a PMOS and an NMOS (positive and negative channel Metal-Oxide-Semiconductor) transistor connected in parallel offer better performance in this task than a single transistor of any type. They effectively pass both low and high voltages without signal distortion induced by threshold voltage loss. The integrator, functioning basically as a first-order LPF, should possess a cut-off frequency F_c considerably lower than the frequency of the slowest signal that undergoes the integration. From the analysis of the extracted features in Figure 3.5 and Figures 3.14, 3.15 (solid green round markers), these frequencies are 11.25 Hz and 1.56 Hz for binary arrhythmia diagnosis and multi-class HAR, respectively. However, to ensure the eventual possibility of extracting any other feature produced with the help of constructed wavelet dictionaries, it is desirable to achieve $F_c < 1/2.56 \text{ s} = 0.39 \text{ Hz}$, i.e., lower than the slowest Haar wavelet with one period in the HAR analysis window.

4.1.3 Digitization

Up to this point, all the simulations presented in Chapter 3 utilized 64-bit double-precision floating-point data to train and evaluate classifiers. Nevertheless, the analog domain NUWS-based features we extract by the A2F converter are traditionally transformed into a digital form to serve as inputs for subsequent classification executed directly within the sensor or after transmission to an aggregator.

For binary arrhythmia detection, the previous study on this application [11] found that a 6-bit precision is sufficient to maintain the same level of prediction accuracy as with the 64-bit data. Therefore, to determine the required ADC resolution to accommodate both studied applications, we also studied the impact of the quantification level on the accuracy of the multi-class HAR classification. Figure 4.2 shows the performances of corresponding NN classifiers trained on features generated from acceleration and angular velocity signals with the help of the adapted SFS algorithm limited to eight feature extractors. We applied the same configuration of Haar wavelets and classifier settings to compare the case with unquantified

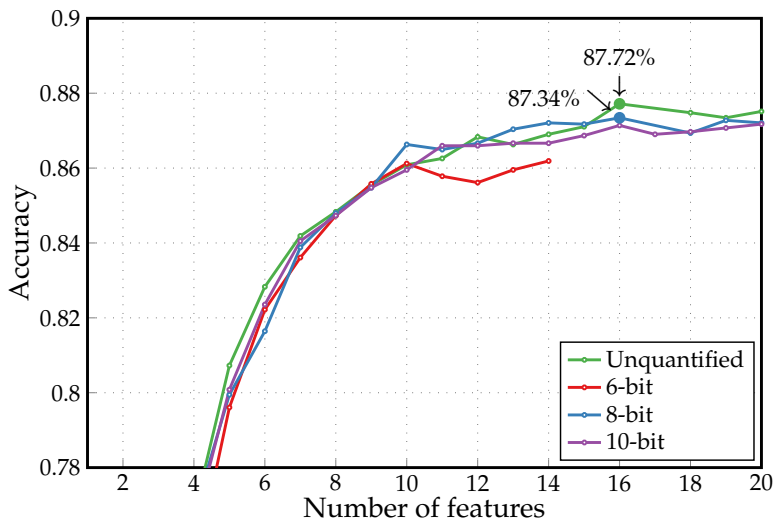


FIGURE 4.2 – Impact of the quantification level on the accuracy of the multi-class HAR performed by NN classifiers with Haar wavelets and IG + adapted SFS feature selection limited to eight extractors

data (a solid green round marker in Figure 3.14). However, we provided the NN classifiers with the training and test sets composed of features quantified after the preselection by the IG criterion. Executed by the SFS algorithm, the choice of features is unavoidably affected by the level of quantification since some features preferred earlier no longer supply information considered relevant for the classification. Hence, the achieved accuracies also change.

In contrast to the arrhythmia detection task, a noticeably lower accuracy is achieved for the multi-class HAR with a 6-bit precision compared to the unquantified case. Also, even more extractors are required to accommodate more than 15 features. Conversely, an 8-bit precision already provides the accuracy of similar order (87.34% at 16 features) to the case without quantification despite the variability of classification performances. Fluctuations in the curves are induced by the process of random initialization of weights and biases while training a new NN classifier each time we increase the number of input features. One possible solution in further work to overcome these fluctuations could be to fix an initialization seed and use the same one when training the classifier with a new input feature.

The highest required ADC conversion rate F_s depends on the maximum oscillation frequency of extracted features. In our case, datasets' sampling rates define the frequency of the fastest Haar wavelet in dictionaries constructed for each studied application. Indeed, one period of this wavelet is twice the interval between consecutive samples of the input signal brought from the dataset. Hence, the developed A2F converter imposes greatly relaxed constraints on the ADC speed, which does not need to exceed half the value of the highest sampling frequency between the two utilized datasets, namely, 180 Hz. Table 4.3 summarizes the hardware specifications of principal components constituting feature extraction and digitization chain of the developed A2F converter.

TABLE 4.3 – Summary of required specifications for hardware implementation of the feature extraction and digitization chain

Section	Component	Requirements
Input multiplexing	Differential analog crosspoint switch	• matrix of switches, • 4 diff. inputs, • 8 diff. outputs
8 feature extractors: • 6 with wavelet generators • 2 with direct integration	Amplifier	• differential structure, • variable gain
	Analog mixer	4 CMOS switches
	Wavelet generator	• storage of wavelet configurations, • programmable clock (360 Hz/50 Hz)
	Integrator	$F_c < 0.39$ Hz
Output multiplexing	Sample-and-hold multiplexer	• internal analog storage of features, • routing stored features to ADC
Digitization	ADC	• 8-bit precision, • $F_s \geq 180$ Hz

4.2 Review of existing hardware solutions

4.2.1 Amplification stage

The amplification stage of a biosensing front-end ASIC proposed in [154] was used in Chapter 3 to estimate the energetic cost of feature extraction while executing adapted and optimized SFS algorithms for training NN classifiers. As an initial consideration, this circuit, implemented in a 180 nm CMOS process and optimized for low noise, power, and area, meets our requirements. Its reconfigurable differential amplifier comprises an LNA and a PGA, providing a variable gain between 38 dB and 72 dB. Table 4.4 compares its performance with several other state-of-the-art designs. This amplification stage stands out from the rest with its considerably small area and a wider range of gain variation, although its power consumption significantly exceeds that of the most recent designs, especially of [170] and [171].

TABLE 4.4 – Performances of amplification stages from state-of-the-art front-end designs

Ref.	Tech. (nm)	Area (mm ²)	Power (μ W)	Supply (V)	Gain (dB)	Input ref. noise	Type of results
[154]		0.0228* [†]	5.04 [‡] , 5.74 [§]	1.4	38–72	2.98 μ V _{rms} (1–4500 Hz)	Measurement
[172]		0.72* [†]	2.3 [¶] , 3	1.8	42–50	1.22 μ V _{rms} (1–100 Hz)	
[173]	180	0.57* [†]	2.17	1	40–53.5	1.16 μ V _{rms} (0.5–100 Hz)	Simulation
[174]		0.07	81	2.7	0–21.6	150 nV/ \sqrt Hz (at 10 Hz)	
[170]		0.122*	0.507	1.2	30–45	0.67 μ V _{rms} (0.5–150 Hz)	
[171]	65	0.16	0.303	0.8	44–71	1.4 μ V _{rms} (1–100 Hz)	

*Total chip area [†]Active part [‡]LNA-PGA [§]LNA-PGA-LPF [¶]Instrum. amplifier ^{||}PGA-LPF-ADC

4.2.2 Wavelet generator

As mentioned in Section 3.1.3.1, we use the digital wavelet generator design elaborated in [11]. The authors synthesized this circuit in X_{FAB}[®] CMOS 180 nm technology and optimized it for low chip area (0.03 mm²) and power consumption (9 μW) with the help of the Clock Gating technique that deactivates the clock signal in unused circuit parts. This generator operates at 2 MHz and produces two binary signals: *C* and *Enable*. *C* controls the mixer's switches in Figure 4.1 and, thus, designates the Haar wavelet's polarity – the wavelet takes a value +1 when *C* is "1" and –1 otherwise. *Enable* indicates the wavelet duration – the wavelet is non-zero when *Enable* is "1".

4.2.3 ADC

The 10-bit charge redistribution SAR ADC, also proposed in [154] and implemented in a 180 nm CMOS process, satisfies our needs. It consumes 0.3 μW power, has a maximum sampling rate $F_{s,Nyq} = 40$ kHz, and provides 9.02 bits of ENOB. These characteristics result in the Walden FoM equal to 14.3 fJ/conversion step. However, this value is considerably worse than the lowest reported value in SAR architectures. The ADC design shown in [27] and implemented in a more advanced 65 nm CMOS process (see Table 1.3 for details) provides 9.1 effective bits and requires 0.35 fJ/conversion. In scenarios where the ADC constitutes a significant portion of the A2F converter's overall power consumption, employing this design with extremely low energy usage may prove necessary. Given the exceptionally low conversion rate required for our applications, it might be helpful to adjust the existing state-of-the-art SAR ADC circuit to achieve even lower consumption at the expense of reducing its maximum speed. However, as it is calculated in one of the further sections, even the contribution of the ADC from [154] to the total consumption of the feature extraction and digitization chain remains negligible. Hence, we can stick to this design when estimating the energetic efficiency of our communication chain for the two studied applications.

4.2.4 Integrator

The integration at frequencies as low as 0.39 Hz may eventually be necessary for feature extraction from inertial signals in the HAR task with a 2.56 s analysis window length. For this purpose, we need to implement a first-order LPF with a sub-Hertz cut-off frequency, which is a significant challenge in practice. Nevertheless, Table 4.5 presents a few examples of designs found in the literature that look to fulfill our specifications. The solution proposed in [155] is an improved version of a widely tunable G_m -C integrator designed in [175]. Despite providing relatively low power consumption, dimensions, and a wide range of cut-off frequency flexibility, the filter from [155] still presents two possible issues. First, its lowest achievable cut-off frequency is relatively close to the specified minimum value equal to 0.39 Hz. Second, a buffer is necessary to pass from the mixer's differential output to the filter's single-ended

TABLE 4.5 – Performances of first-order LPFs with a sub-Hertz cut-off frequency

Ref.	Tech. (nm)	Area (mm ²)	Power (μ W)	Supply (V)	DR (dB)	Cut-off frequency range
[155]	180	0.0156	1.08	1.8	65.5 – 73.0	0.22 Hz – 39.1 kHz
[175]		0.051	2.7		> 80	0.114 Hz – 2.5 kHz
[176]	350	0.07	0.005	1	64	0.002 Hz – 90 Hz

input, as shown in Figure 4.1. Despite a higher minimum cut-off frequency and increased power consumption compared to the design [176], the circuit in [155] occupies a significantly lower area, provides a larger input dynamic range (DR), and uses a 180 nm CMOS process as well allowing to maintain consistency with previously chosen amplification stage and wavelet generator. Therefore, in the next section, we perform the simulations at the schematic level of the G_m -C integrator based on the design elaborated in [155], aiming to achieve a very low cut-off frequency but without tuning, which is unnecessary for the A2F converter.

Regarding the choice of technology node for the entire converter’s circuit implementation, we opt for a 180 nm CMOS process. According to the data presented in Tables 4.4 and 4.5, this process is still widely employed in many modern analog designs due to its maturity, availability of design tools, and optimal balance between performance and cost-effectiveness.

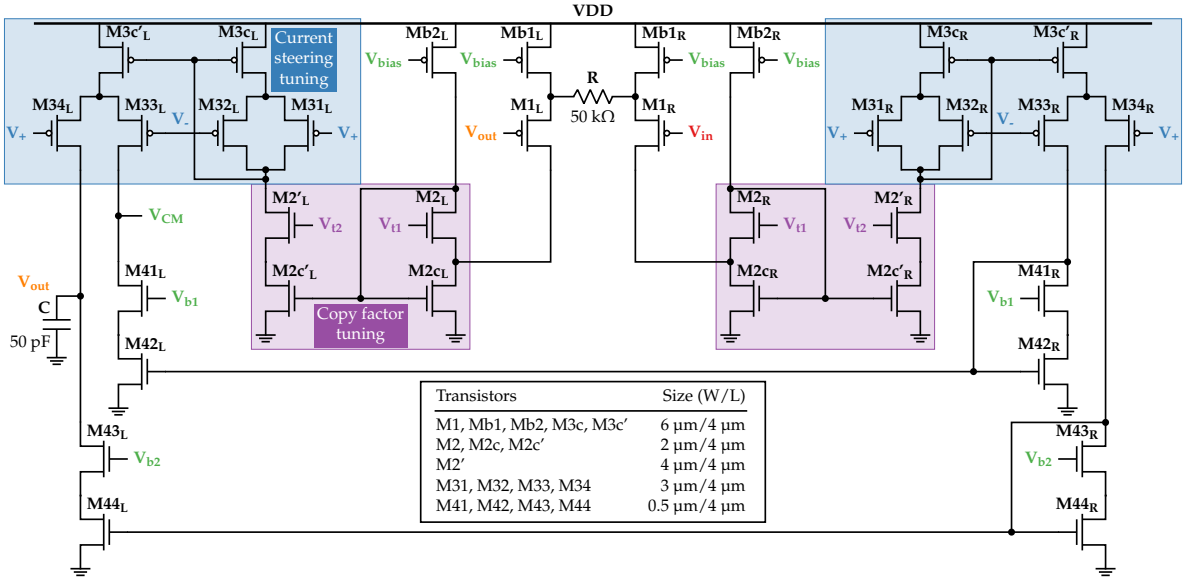
4.3 G_m -C integrator design

In this section, we present the simulations of the first-order LPF based on [155] design and determine its biasing and control voltages to achieve a cut-off frequency low enough for the studied A2F converter’s applications.

4.3.1 Architecture and its functioning principle

Figure 4.3 shows a schematic of the proposed G_m -C integrator with all transistors’ dimensions (width W , length L). This design is based on a classic mirrored operational transconductance amplifier (OTA) with a degenerated PMOS input differential pair. Voltage V_{in} at the gate of $M1_R$ is the circuit’s input. The gate of $M1_L$ and the loading capacitor C are connected together and form the output node V_{out} . Voltages $V_+ = V_c + V_{gc}$ and $V_- = V_c - V_{gc}$ comprise their "common mode" V_c and a deviation V_{gc} . Hence, the circuit has four control voltages: V_{t1} , V_{t2} , V_c , and V_{gc} . Three biasing voltages are V_{bias} , V_{b1} , and V_{b2} . Voltage V_{CM} tied to one of the output branches also serves as a common mode of the input V_{in} .

In this circuit, the minimization of the cut-off frequency is achieved either by maximizing the loading capacitance C or by minimizing the OTA’s transconductance G_m . Since the area constraints and other limitations imposed by CMOS technology restrict the former, we set its value to $C = 50$ pF. On the other hand, the OTA’s transconductance G_m is regulated in this


 FIGURE 4.3 – Transistor-level schematic of the G_m -C integrator proposed in [155]

circuit using two adjustment techniques. The first one, *copy factor tuning*, allows controlling the amounts of complementary currents copied from the input stage through the NMOS high swing cascode current mirror (transistors M2, M2c, and M2c' in left and right branches) by setting $V_{t2} \leq V_{t1}$. The second technique, *current steering tuning*, splits the current passed through the 1:1 PMOS high swing cascode current mirror (transistors M31, M32, M3c, and M3c' in both branches) into two complementary currents flowing through transistors M33 and M34. The differential control voltage V_{gc} allows adjusting the complementary gate voltages V_+ and V_- and, therefore, the fractional values of corresponding output currents.

The primary purpose of using this G_m -C integrator for our A2F converter is to obtain a very low sub-Hz cut-off frequency. Hence, we aim to select the V_{t2} and V_{gc} voltage values that minimize the OTA's transconductance. This selection implies that both adjustment techniques should reduce the output current in the integrator's output branch made of transistors M34, M43, and M44. Thus, we should decrease V_{t2} and increase V_{gc} as much as possible. However, the OTA becomes more asymmetrical as V_{t2} and V_{\pm} deviate from equilibrium values V_{t1} and V_c , respectively, degrading the integrator's DR and noise performance. Therefore, we choose the optimal pair of V_{t2} and V_{gc} values through simulations.

Although implemented using a 180 nm CMOS process, the integrator in [155] was designed with TSMC[®] technology, which differs from the targeted XFAB[®] technology. Moreover, several biasing voltages are not stated in this paper. Hence, we determine all the necessary and missing voltage values from the schematic-level simulation results presented below before assessing the integrator's performance. These values include all four control voltages (V_{t1} , V_{t2} , V_c , and V_{gc}), two biasing voltages (V_{b1} and V_{b2}), and the input common-mode voltage V_{CM} . Voltage V_{bias} is set by a biasing current introduced through a 1:1 current mirror at this node.

4.3.2 Direct current (DC) simulations

First, DC simulations of the circuit in the open-loop configuration are performed to determine proper V_{t1} and V_c values. According to Figure 4.4a, $V_{t1} = 0.6$ V is enough to keep the currents I_{Mb1} and I_{Mb2} approximately equal to a 50 nA biasing current introduced through a 1:1 current mirror via V_{bias} node to Mb1 and Mb2 transistors. This choice of V_{t1} also maintains M2 and M2c in the subthreshold region. Next, as seen in Figure 4.4b, with the current steering tuning off ($V_{gc} = 0$ V $\Rightarrow V_{\pm} = V_c$), a constant common voltage V_c is swept from 0 V to 1.8 V with V_{t2} varied in a 0.35–0.6 V range allowed by $V_{t2} \leq V_{t1}$ condition. For further simulations, V_c is set to a 1.1 V value, ensuring that the current sunk by M2c' remains on the plateau for slight variations of V_c and any $V_{t2} \leq V_{t1} = 0.6$ V.

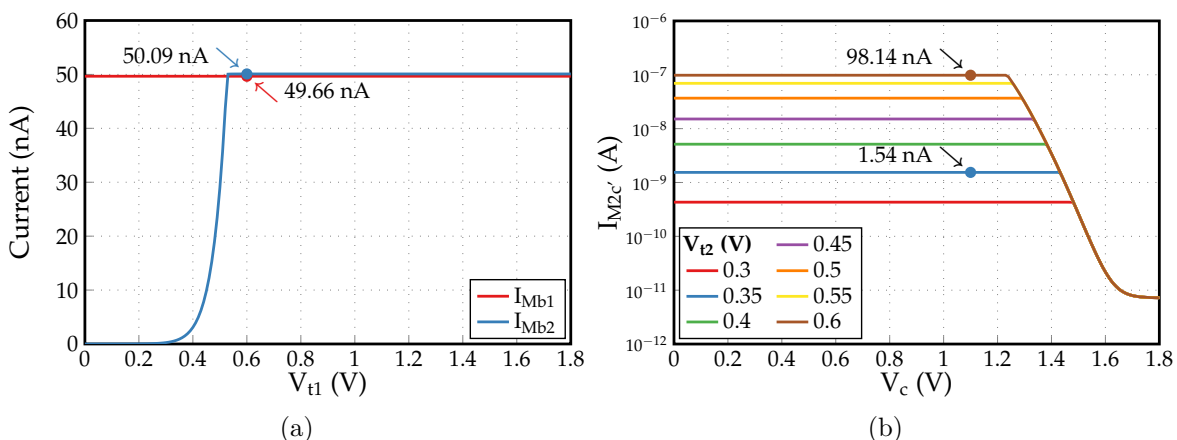


FIGURE 4.4 – Results of DC simulations in the open-loop configuration to determine control voltages (a) V_{t1} and (b) V_c

4.3.3 Alternating current (AC) simulations

Next, we perform the AC simulations in the integrator configuration to determine proper V_{t2} and V_{gc} values. Figure 4.5 presents the corresponding results obtained with an input common-mode voltage V_{CM} initially set to 0.9 V, half of the power supply voltage V_{DD} , as in [155]. Voltages V_{t2} and V_{gc} are swept from 0.35 V to 0.6 V and from -0.1 V to 0.15 V, respectively. Biasing voltages V_{b1} and V_{b2} are set to $V_{t2} + 0.1$ V to ensure the correct functioning of the output branches. Figure 4.5a illustrates a DC gain error GE_{DC} with an arbitrarily chosen upper limit $GE_{DC} = 0.5$ dB set to reduce the non-linearity. Excluding V_{t2} and V_{gc} pairs that result in $GE_{DC} > 0.5$ dB, we obtain the cut-off frequencies F_c shown in Figure 4.5b. Aiming for $F_c < 0.39$ Hz, we choose the three best V_{t2} and V_{gc} pairs with the lowest achieved cut-off frequencies for $V_{CM} = 0.9$ V case and summarize them in Table 4.6.

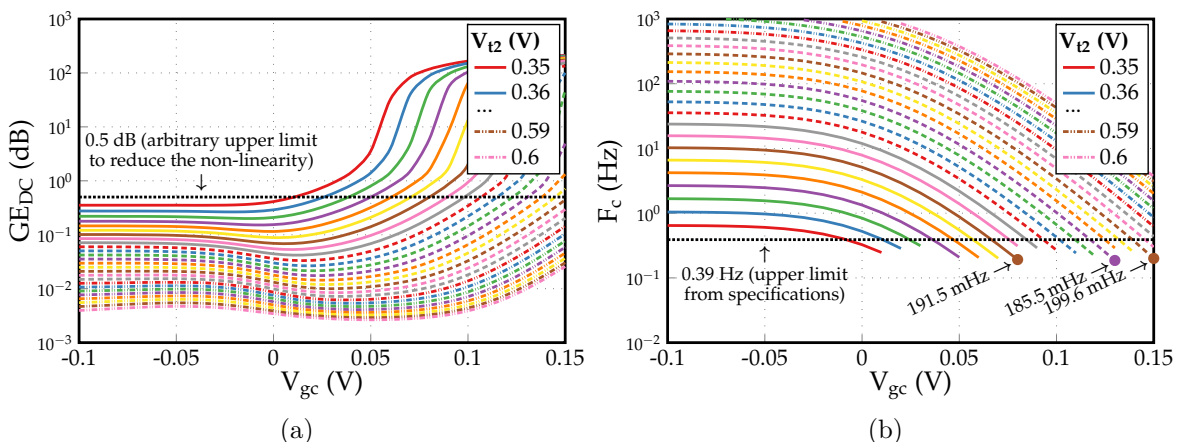


FIGURE 4.5 – Results of AC simulations in the integrator configuration with $V_{CM} = 0.9\text{ V}$ to determine control voltages V_{t2} and V_{gc} : (a) cut-off frequency F_c ; (b) DC gain error GE_{DC}

TABLE 4.6 – Best V_{t2} , V_{gc} pairs with the lowest cut-off frequencies F_c from AC simulations with $V_{CM} = 0.9\text{ V}$

V_{CM} (V)	V_{t2} (mV)	V_{gc} (mV)	F_c (mHz)	GE_{DC} (dB)
0.9	410	80	192	0.495
	470	130	186	0.481
	500	150	200	0.444

4.3.4 Input common-mode voltage

The pair with $V_{t2} = 0.5\text{ V}$ and $V_{gc} = 0.15\text{ V}$ displays a good trade-off between the cut-off frequency and the DC gain error, providing $F_c = 199.6\text{ mHz}$ and $GE_{DC} = 0.444\text{ dB}$. We use this pair of values to produce static input-output characteristics shown in Figure 4.6a, where the integrator's output voltage V_{out} is plotted against its "differential" input voltage $v_{in} = V_{in} - V_{CM}$ for a range of common-mode voltage V_{CM} values. It is seen that the maximum allowed V_{out} is limited to $\lesssim 1.17\text{ V}$. Hence, it is reasonable to switch to $V_{CM} = 0.6\text{ V}$ for the sake of higher input symmetry and DR. Figure 4.6b shows that decreasing V_{CM} leads to a slight increase of F_c up to 209 mHz , but also reduces GE_{DC} to 0.415 dB .

Next, we reproduce the results of AC simulations with the input common-mode voltage V_{CM} set to 0.6 V but do not show the obtained curves due to their strong similarity to Figure 4.5. As displayed in Table 4.7, three updated optimal V_{t2} and V_{gc} pairs provide comparatively close performances regarding F_c and GE_{DC} to the pairs with $V_{CM} = 0.9\text{ V}$ in Table 4.6. With a revised common-mode voltage $V_{CM} = 0.6\text{ V}$, we prefer to keep the same control voltages $V_{t2} = 0.5\text{ V}$ and $V_{gc} = 0.15\text{ V}$ that still offer a satisfactory compromise between the cut-off frequency and the DC gain error.

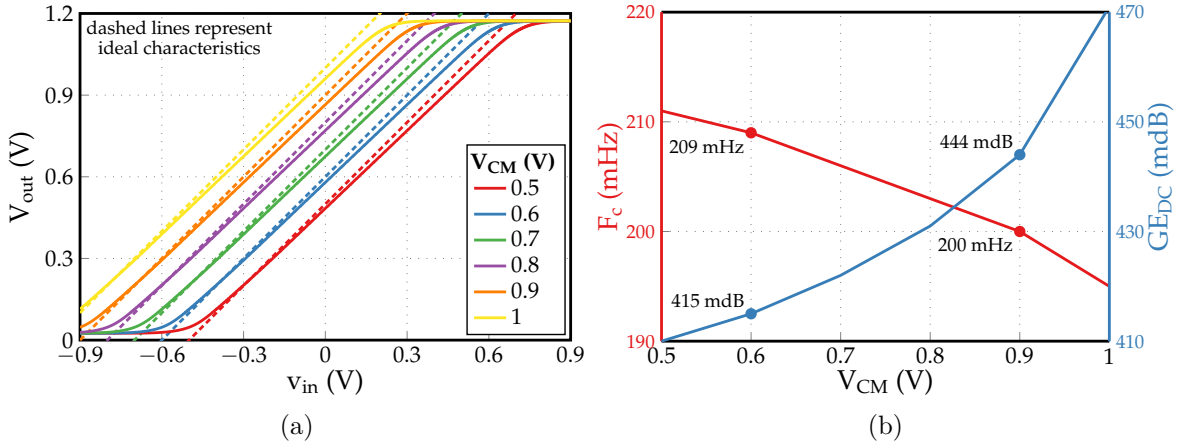


FIGURE 4.6 – Impact of common-mode voltage V_{CM} values on (a) v_{in} - V_{out} characteristic and (b) cut-off frequency F_c and DC gain error GE_{DC}

TABLE 4.7 – Best V_{t2} , V_{gc} pairs with the lowest cut-off frequencies F_c from AC simulations with $V_{CM} = 0.6$ V

V_{CM} (V)	V_{t2} (mV)	V_{gc} (mV)	F_c (mHz)	GE_{DC} (dB)
0.6	420	90	184	0.490
	470	130	193	0.453
	500	150	209	0.415

4.3.5 Biasing voltages

Now, with the input common-mode voltage V_{CM} and all the control voltages V_{t1} , V_{t2} , V_c , and V_{gc} set, we can determine the optimal biasing voltages V_{b1} and V_{b2} . For this purpose, we sweep their values during the next phase of AC and DC simulations. Figure 4.7 illustrates the obtained results and introduces two new characteristics. The maximum input amplitude Amp_{max} stands for the minimum value between minimum (negative) and maximum (positive) "differential" input voltages that ensure $\partial V_{out}/\partial V_{in}$ deviation from ideal unity gain below 0.5 dB. Seeking to minimize F_c and GE_{DC} while maintaining a high input DR, we introduced the following FoM that should be maximized:

$$FoM = \frac{Amp_{max}}{F_c \cdot GE_{DC}} \quad (4.1)$$

It is seen that changing V_{b1} values above 0.6 V has a negligible impact on all of the four considered characteristics. Meanwhile, $V_{b2} = 0.4$ V is close to an optimum in terms of FoM and shows a good trade-off between F_c , GE_{DC} , and Amp_{max} .

Table 4.8 summarizes the chosen biasing and control voltages required for the functioning of the circuit and its performance characteristics. Our choice of control voltages reduced the transconductance and, thus, the currents in the output stages of the G_m -C integrator.

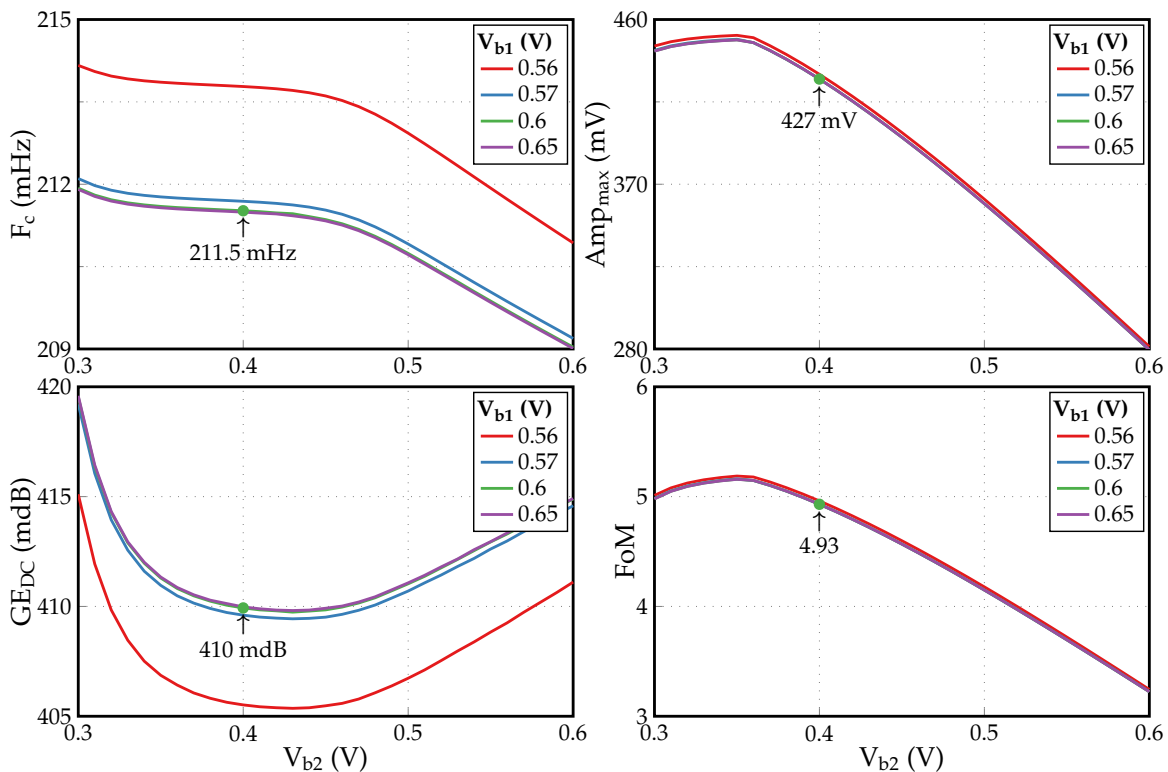


FIGURE 4.7 – Impact of biasing voltages on the integrator’s performance characteristics

TABLE 4.8 – Integrator’s biasing, control voltages and performance summary

Biasing and control voltages							Performance summary			
V_{CM} (V)	V_{t1} (V)	V_{t2} (V)	V_c (V)	V_{gc} (V)	V_{b1} (V)	V_{b2} (V)	F_c (mHz)	GE_{DC} (dB)	Amp_{max} (mV)	Power (nW)
0.6	0.6	0.5	1.1	0.15	0.6	0.4	211.5	0.41	427	625

Therefore, its estimated power consumption, calculated as a product of the sum of currents and the supply voltage, decreased from $1.08 \mu\text{W}$ measured in [155] to 625 nW . In the next section, this revised value serves to estimate the energy spent by the communication chain with the A2F converter.

The integrator and wavelet generator are specific and critical blocks for the developed A2F converter. Meanwhile, other components of its communication chain represent classic blocks with a broad range of available design solutions in the literature. Hence, we can borrow the values for their power consumption from recent designs chosen in Section 4.2 for this purpose.

4.4 Classification with non-ideal integration coefficients

It is important to check how the ML classification models can deal with the non-idealities introduced by analog circuits, such as non-linearities and noise. The developed A2F con-

verter aims to extract the features from signals directly in the analog domain with the help of the NUWS technique. Hence, the feature extraction chain and preceding signal conditioning circuitry employ such analog blocks as an amplification stage, mixer, and integrator. Therefore, it is crucial to verify whether the classification algorithms can learn and accommodate the non-idealities of these components, thus making the A2F conversion approach robust to imprecisions caused by their usage.

As a first step towards this goal, we can assess the impact of using more realistic non-ideal integration coefficients F_{GmC} provided by the simulated G_m -C integrator and serving as input features for our trained NN classifiers. Until now, we have trained and evaluated the NN classifiers with the integration coefficients F_{init} , i.e., features produced by imitating analog mixing and integration of truly analog signals. Effectively, we multiplied datasets' samples (sampled at 360 Hz in the MITDB and 50 Hz in the UCI-HAR dataset) with generated wavelets' samples and performed an ideal trapezoidal rule integration of the resulting uniform sequence of samples. Hence, our simulations approximated the analog-domain feature extraction.

We can re-evaluate our classifiers by passing more realistic non-ideal integration coefficients F_{GmC} to their inputs. For this purpose, we interpolate the datasets' signals to make them closer to analog form, multiply the result with wavelets, and feed the obtained samples with proper scaling to the integrator's input during transient analysis. The voltage values read from the integrator's output at the end of the integration period are scaled back and then serve as F_{GmC} . Table 4.9 compares the performances of the reference cases marked as ① with three other cases for both studied applications.

Case ② skips the learning phase and uses the classifier model produced by ①. In the evaluation phase of ②, realistic coefficients F_{GmC} serving as a test set are produced from eight and 16 wavelets corresponding to features chosen by ①. In both applications, especially

TABLE 4.9 – Re-evaluation of NN classifiers using non-ideal integrator's outputs

Task	Case	Training phase		Evaluation phase		
		Type of inputs	Available features	Type of inputs	Chosen features	Accuracy (%)
Binary arrhythmia detection	①	F_{init}	100 best (IG)	F_{init}	8	98.17
	②	Model trained in ①		F_{GmC}	8 from ①	97.18
	③	F_{GmC}	8 from ①			97.71
	④		100 best (IG)			7
Multi-class HAR ($acc_{x,y}+gyr_z$)	①	F_{init}	100 best (IG)	F_{init}	16	87.72
	②	Model trained in ①		F_{GmC}	16 from ①	35.15
	③	F_{GmC}	16 from ①			85.88
	④		100 best (IG)			16

in the HAR task, the accuracy drops in this case. It confirms that F_{init} and F_{GmC} differ significantly, and we need to train the classifiers with non-ideal coefficients F_{GmC} as well.

In case ③, we still provide only eight and 16 wavelets corresponding to features chosen by ① but make the training based on F_{GmC} . This case improves the classification performances in both applications and brings the achieved accuracies much closer to the levels of reference case ①. Furthermore, in ④, we re-run the entire feature selection procedure based on F_{GmC} , including the preselection of the 100 best features according to the IG criterion, before performing the corresponding SFS algorithms (optimized for the arrhythmia detection, adapted for the HAR). In arrhythmia detection, this even allows the accuracy to slightly exceed the value obtained in ① by 0.17%. However, case ④ does not improve the classification performance in the HAR. There are two principal reasons for this: large deviations of F_{GmC} values from F_{init} induced by the accumulation of errors in the features requiring long integration (wavelets) and the absence of specific features in the list of features available for the SFS algorithm since they bring less relevant information now according to the IG criterion.

Cases ③ and ④, re-trained on non-ideal integration coefficients F_{GmC} , yield close or even exceeding classification performances compared to case ①, initially trained with ideal integration coefficients. This fact confirms that classification algorithms can learn and accommodate the non-idealities introduced by at least such analog circuits as integrators. Therefore, A2F converters are capable of mitigating design constraints on analog circuits.

4.5 Evaluation of energetic efficiency

In this section, we compare the energetic efficiency of our communication chain to those relying on Nyquist and A2I techniques to show the benefits of using the A2F converter in WBAN sensors, particularly for the two explored applications. We estimate the energy consumption in the arrangements composed of the acquisition systems based on these approaches and of the BLE wireless transmitter from [38], which consumes 3.7 nJ per transmitted bit.

The acquisition chain representing the conventional Nyquist approach considered here is entirely composed of the components presented in [154] and operates at $F_s = 2$ kHz. Alongside the previously mentioned amplification stage and SAR ADC, it involves an antialiasing G_m-C type third-order LPF preceding the ADC and consuming 0.7 μW. Thus, its total power consumption is 6.04 μW.

Similarly to [11], for the binary arrhythmia detection application, we also consider the A2I architecture proposed in [136] and designed for the CS acquisition of biological signals. In the case of ECG signals, this A2I converter is configured to work with 32 channels and 128 sampling cycles in the analysis window, corresponding to a compression ratio of four compared to the Nyquist approach. SAR ADCs within each channel provide a 10-bit precision as well. For a sampling frequency F_s of 2 kHz, the total power consumption of the circuit is 0.9 μW.

Nonetheless, this does not account for the power required to recover the original signal from the compressed data.

4.5.1 Energetic cost of feature extraction and digitization

To estimate the energetic cost E_{A2F}^{feat} of each extracted feature in Section 3.1, we used the definition (3.1) that we recall here:

$$E_{A2F}^{feat} = (P_{amp} + P_{int} + P_{wavelet}) t_s + \frac{P_{ADC}}{F_s} \quad (4.2)$$

It assumes that the A2F converter’s principal components in the extraction chain, i.e., the amplifier, the integrator, and the wavelet generator, are active only during the wavelet support duration t_s . Their power consumptions are $P_{amp} = 5.04 \mu\text{W}$, $P_{int} = 0.625 \mu\text{W}$, and $P_{wavelet} = 8.984 \mu\text{W}$. To digitize any feature, the ADC with $P_{ADC} = 0.3 \mu\text{W}$ and $F_s = 40 \text{ kHz}$ consumes the energy required for one sampling period, i.e., $E_{ADC}^{feat} = 7.5 \text{ pJ}$ per feature.

In the case of binary arrhythmia diagnosis, to estimate the energy consumption induced by employing the A2F converter in the communication chain, we rely on eight features selected by the optimized SFS algorithm (solid green round marker in Figure 3.5). Applying the optimized SFS algorithm to the multi-class HAR resulted in a choice of features that led to a severe limitation of achievable classification accuracy in favor of energy reduction. To solve this issue, we need to modify the algorithm’s original evaluation criterion (metric) or implement more profound changes to the feature selection procedure, such as employing the SFFS. These directions have not been explored in this thesis but are a solution for further work. To maintain relatively high classification performances in the multi-class HAR, we perform the energetic estimations based on the costs of 16 and 17 features chosen by the adapted SFS (solid green round markers in Figures 3.14, 3.15, yet not showing the required energy) when using all available inertial signals and exclusively acceleration signals, respectively.

4.5.2 Consumption estimations

4.5.2.1 Classification at aggregator

We can first estimate the energy required to extract the relevant features from ten seconds of ECG and inertial signals and to transmit them from the corresponding sensors to the aggregators for further classification, taking into account the revised value of the G_m -C integrator’s power consumption. According to the hardware implementation diagram proposed in Figure 4.1, we can assume the allocation of one amplifier for each input signal outside the feature extractors. In this case, the amplification stage does not consume twice during the overlapping segment of two features extracted from the same signal using overlapping wavelets. Conversely, in calculations based on the definition (4.2), we considered the amplification’s stage contribution to the energy consumption independently for each feature. Therefore, we

now introduce an effective operating time of the amplification stage t_{amp} during the analysis window. The acquisition and transmission energies for ten seconds of studied signals, E_{A2F}^{10s} and E_{TX}^{10s} , are then evaluated according to the following expressions:

$$E_{A2F}^T = \left[P_{amp} \cdot t_{amp} + (P_{int} + P_{wavelet}) \cdot t_s^w + E_{ADC}^{feat} \cdot N_{feat}^w \right] \cdot \frac{T}{T_w} \quad (4.3a)$$

$$E_{TX}^T = FoM \cdot n_{ADC} \cdot N_{feat}^w \cdot \frac{T}{T_w} \quad (4.3b)$$

where t_s^w stands for the sum of support durations of all wavelets producing all N_{feat}^w selected features within one analysis window of length T_w ; T denotes the desired time interval for calculation; the product of the transmitter's FoM and ADC's resolution n_{ADC} is the transmitter's efficiency expressed in energy per sent feature. The necessary data for calculations and the obtained E_{A2F}^{10s} and E_{TX}^{10s} values for both applications are outlined in Table 4.10.

TABLE 4.10 – Estimated energy consumption to extract and transmit features from ten seconds of studied signals using A2F conversion with classification at aggregator

Task	Extracted features			Acquisition (A2F)		Transmission	
	N_{feat}^w	t_s^w (t_{amp})	T_w	Consumption	E_{A2F}^{10s}	FoM	E_{TX}^{10s}
Bin. arrh. detection	8	0.172 s (0.133 s)	0.711 s	$P_{amp} = 5.04 \mu\text{W}$ $P_{int} = 0.625 \mu\text{W}$	32.7 μJ		4.2 μJ
Multi-class HAR	16	13.92 s (5.76 s)	2.56 s	$P_{wavelet} \approx 9 \mu\text{W}$ $E_{ADC}^{feat} = 7.5 \text{ pJ}$	456 μJ^*	3.7 nJ/bit	2.3 μJ
	17	12.32 s (5.76 s)		($n_{ADC} = 10 \text{ bit}$)	396 μJ^*		2.5 μJ

* Excludes wavelet generation for two features produced from the "constant" wavelet

Figure 4.8 shows, on a logarithmic scale, the contribution of the acquisition and transmission stages and the total energy spent on processing ten seconds of ECG signal using three wireless approaches. The proposed communication chain with the A2F converter consumes 21.7 and 5.3 times less in total than those employing the Nyquist and A2I approaches, respectively. Whereas the consumption of the transmission process in the A2F converter is 44 times lower than that of the A2I converter, the energy spent in the acquisition chain represents 88.6% of total consumption in the A2F approach, and its value even exceeds the acquisition part in the A2I converter by 3.6 times.

Performing similar calculations for the HAR, we obtain the breakdown of energy consumption shown in Figure 4.9 induced by processing ten seconds of the inertial signals with the Nyquist and A2F approaches. Both cases of the A2F conversion – with features extracted from signals of two types ($acc_{x,y} + gyr_z$) and only from accelerometer signals ($acc_{x,y,z}$) – are compared to the Nyquist approach that samples three signals uniformly with $F_s = 2 \text{ kHz}$ and sends them to the aggregator. As observed, employing the A2F converter leads to a

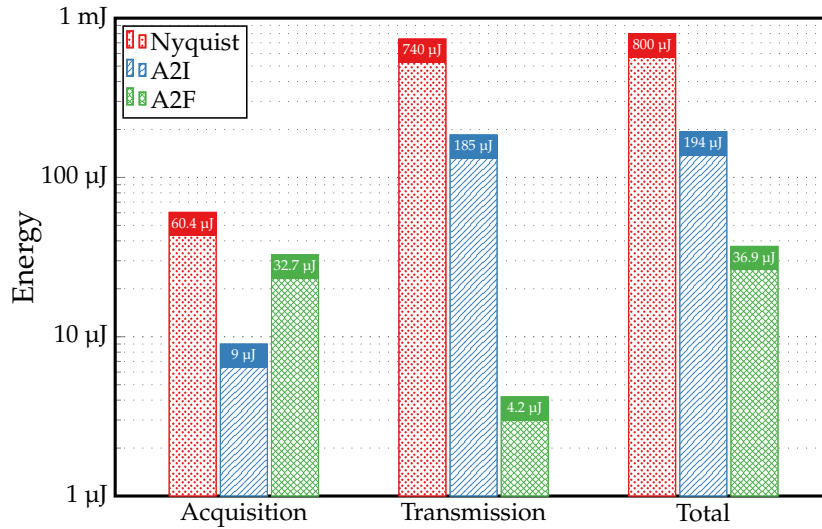


FIGURE 4.8 – Energy to process ten seconds of ECG signal with three wireless approaches

substantial decrease in the overall energy consumption of WBAN inertial sensors by 5.2 or 6 times, owing to the drastic reduction in energy associated with transmission. However, the acquisition part in the A2F approach of both applications remains high and even exceeds that of the Nyquist approach by 2.5 or 2.2 times while used for the HAR task. Hence, developing a modified version of the optimized SFS algorithm – power-aware feature selection based on the complete A2F converter’s circuit simulations – is necessary.

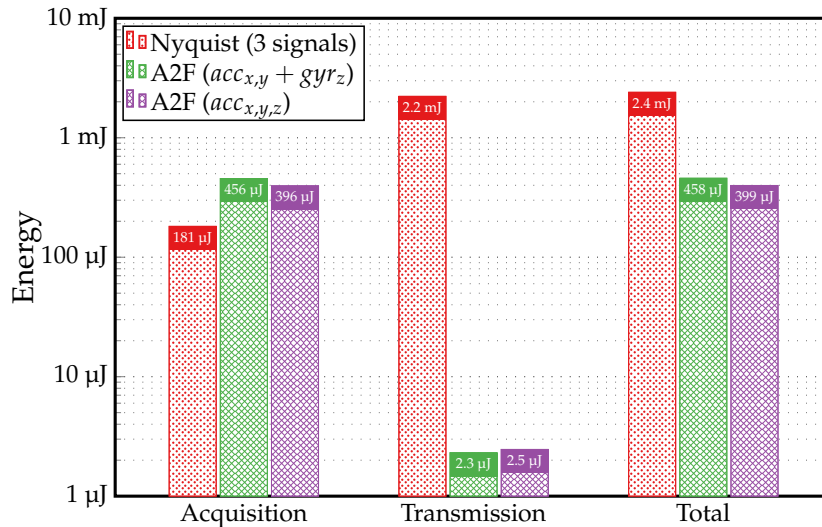


FIGURE 4.9 – Energy to process ten seconds of inertial signals with two wireless approaches

4.5.2.2 Classification within sensor

So far, we have considered sending the extracted features from the sensors for further classification at the aggregator level. However, as discussed in Section 3.2.4, we can perform

the classification directly within the sensor to further diminish the transmitted data and send only the classification results. For this purpose, it is possible to implement at least a digital architecture of our simple feedforward NNs realized on Field Programmable Gate Array (FPGA) [177–179], in ASIC [179,180], or on microcontroller [181,182].

In [177], a multi-layer perceptron with one hidden layer and a 7-6-5 topology was implemented in Xilinx Artix-7[®] FPGA. The proposed design consumes $P_{FPGA} = 120$ mW and requires $t_{class} = 270$ ns for one classification. Without re-evaluating this data, due to a similarity of the topology with our NNs, we can use these values to estimate the energy spent on processing ten seconds of analyzed signals with the classification performed directly within the sensor. While the acquisition part remains unchanged, we spend additional energy due to classification and reduce the consumption attributed to the transmission process. The former is calculated as a product of the required power P_{FPGA} , the time necessary for one classification t_{class} , and the number of classifications performed in ten seconds.

In binary arrhythmia detection, instead of sending eight features coded on ten bits, we transmit only one bit of the classification result, thus reducing by 80 times the energy of transmission. Figure 4.10 compares the obtained consumption breakdowns of two approaches. For both studied cases ($acc_{x,y} + gyr_z$ and $acc_{x,y,z}$) in the multi-class HAR, to accommodate six classes, we transmit three bits per classification rather than 16 or 17 features coded on ten bits. This results in a 53 or 57-times reduction in the energy consumed by the transmitter, as illustrated in Figure 4.11. However, despite a considerable decrease in transmission energy in both applications, the total consumption reduction is negligible, especially in the HAR task. Now, the acquisition process represents more than 98% of the sensor’s total consumption in both applications. Hence, optimization should be done within the signal conditioning and feature extraction circuitry to cut down substantially on energy usage in WBAN sensors.

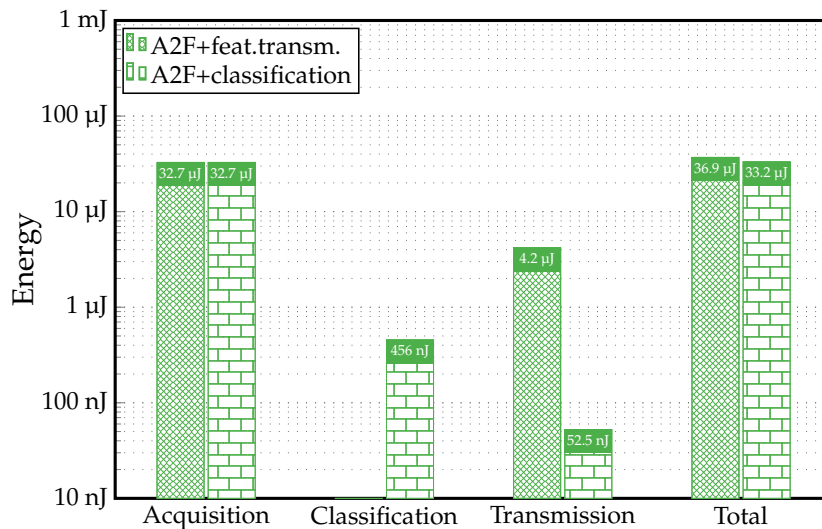


FIGURE 4.10 – Energy to process ten seconds of ECG signal with two A2F approaches

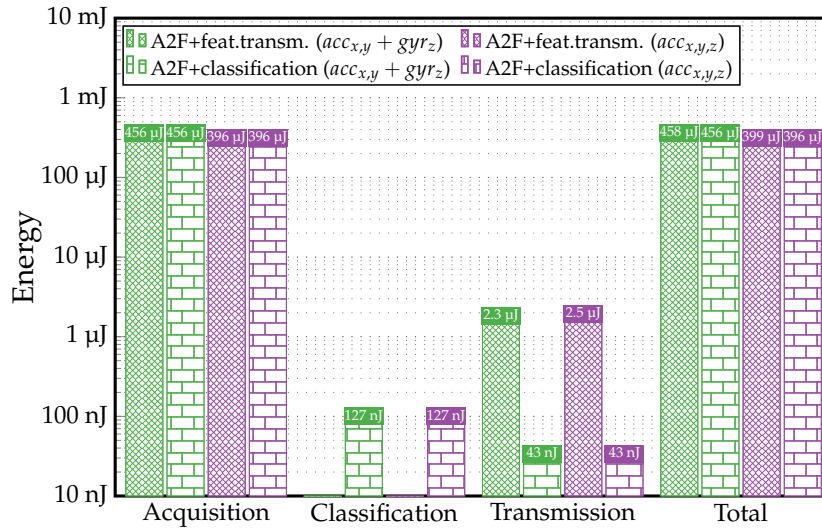


FIGURE 4.11 – Energy to process ten seconds of inertial signals with two A2F approaches

4.5.2.3 Comparison to existing embedded designs

We can compare the performance of our system employing the A2F conversion with in-sensor classification (omitting the transmission energy) to recent embedded designs.

An ECG processor ASIC with arrhythmia detection proposed in [183] and implemented in a 65 nm CMOS technology consumes $2.04 \mu\text{W}$ of power. It locates R-peaks and abnormal R-R intervals by searching for local extremes of the signal derivative with self-adaptive thresholds, achieving a 96.9% classification sensitivity on the MIT-BIH Arrhythmia dataset. The authors improved the classification accuracy and sensitivity to 97.5% and 98.2% in the ASIC proposed in [184] and designed for long-term implantable cardiac monitoring. This solution employs an adaptive R-peak detection and arrhythmia marking algorithm using slope threshold and median filter with immunity to different interferences. Within the measured total power increased to $2.63 \mu\text{W}$ due to more functions onboard compared to [183], the detection part consumes only 81.9 nW. A wearable ECG processor for arrhythmia detection presented in [185] and fabricated in a 110 nm CMOS technology provides an average classification accuracy of 97.34% with a $4.08 \mu\text{W}$ total power consumption. It utilizes a Hilbert transform-based R-peak detection, a Haar discrete wavelet transform to extract features, and a hybrid classifier that combines a linear pre-classifier and a polynomial kernel SVM. At the same time, our A2F converter shows a 98.17% accuracy and a 92.62% sensitivity with an average power consumption of $3.32 \mu\text{W}$ while detecting arrhythmia according to estimated energy usage on acquisition and classification from Figure 4.10.

A wearable HAR system designed on the Spartan-6 FPGA in [186] uses a PCA-based dimensionality reduction technique to choose the relevant features extracted from time and frequency domains and a two-hidden-layer back-propagation NN for classification. However, it was tested using the accelerometer data from another dataset, namely PAMAP, achieving

an 89.2% accuracy at a 268 mW power consumption. A HAR framework implemented on the TI-CC2650 microcontroller unit in [187] shows a 97.7% accuracy in identifying six activities and their transitions in the online training experiment with nine users while consuming 11.24 mW during computation. The proposed solution extracts the FFT and DWT features from stretch and accelerometer sensors for further inference and training using an NN. The authors followed up in [188] with the first fully integrated custom hardware accelerator implemented in a 65 nm TSMC[®] technology. This design achieves a 95% accuracy in recognizing eight human activities while consuming 51 μ W of active and 14 μ W of idle power. A deep NN exploits similar features to those extracted in the previous work for classification purposes. In comparison, the A2F converter proposed here distinguishes six human activities with an estimated average power consumption equal to 45.6 μ W (features from $acc_{x,y} + gyr_z$ signals) or 39.6 μ W (features from $acc_{x,y,z}$ signals) and an 87.7% or 87.2% accuracy.

Thus, our system employing the A2F conversion, the NUWS-based feature extraction, and in-sensor classification offers lower energetic efficiency than certain embedded designs for both studied applications. Nevertheless, unlike these designs, the developed solution promises genericity and adaptability across different applications for various low-frequency signals while remaining relatively low-power.

4.6 Conclusion

This Chapter lays the foundation for a complete circuit design in the hardware of the generic A2F converter developed in this thesis.

Preliminary, in Chapter 3, we iteratively constructed ML models in the joint feature selection and task-specific classification process. This procedure was carried out separately for two studied applications, terminated in each case by choosing an NN classifier, achieving a good trade-off between the classification performance and the number of required features at the classifier's inputs. Corresponding features, considered relevant for a given classification task, serve as a basis for defining hardware specifications in this Chapter. Specifically, we derive the specifications of the principal A2F converter's components, including the amplification stage, analog mixer, wavelet generator, integrator, and ADC. Next, we examine available recent hardware solutions for these components in the literature.

In particular, thanks to employing Haar wavelets, the wavelet generator can utilize an entirely digital structure, while the analog mixer is simplified to four CMOS switches. Both the amplification stage and ADC proposed in [154] and implemented in a 180 nm CMOS process satisfy our needs. The wavelet generator design elaborated in [11] using the same process node fulfills our specifications. However, achieving a sub-Hz cut-off frequency in the G_m -C integrator, a critical A2F converter's component, is challenging. Hence, this Chapter presents the circuit-level simulations of the integrator based on the design [155] realized in a 180 nm CMOS process with seemingly suitable characteristics for the A2F converter. Through

simulations, we define its biasing and control voltages that result in a cut-off frequency that is as low as possible to guarantee the ability to integrate the product of the input signal with the slowest Haar wavelet among two wavelet dictionaries dedicated to our applications.

We evaluate our NN classifiers using more realistic non-ideal integration coefficients, i.e., features produced at the outputs of the simulated G_m -C integrator in transient analysis. The results confirm that classification algorithms can learn and accommodate the non-idealities introduced by such analog circuits as integrators. Therefore, A2F converters are capable of mitigating design constraints on analog circuits.

With the integrator's power consumption value revised after simulations, we estimate that the proposed communication chain with the A2F converter consumes 20 and five times less compared to the Nyquist approach for the ECG and inertial signals, respectively. This fact highlights the potential of A2F conversion in achieving flexible, low-power WBAN sensors that capture their signals continuously in healthcare and beyond.

When comparing our system employing in-sensor classification to recent embedded solutions found in the literature, we note that certain designs offer better energetic efficiency for both applications, especially considering the rough consumption estimates made for the A2F converter components. Nevertheless, the advantage of the developed solution lies in its genericity, meaning that it promises multi-application suitability while remaining relatively low-power. Further reduction of energy spent in our acquisition chain can be achieved by employing analog, reconfigurable NNs [163–165] based on memristors to digitize the classification result solely. This would also enable learning algorithms such as back-propagation to be implemented on a chip [162], providing the application- or context-specific adaptation.

Conclusions and Perspectives

Conclusions on the completed work

Due to world population growth and aging [1], one of the crucial challenges humanity has to address in the upcoming future is an inevitable rise in the rate of chronic diseases, a leading cause of death [2], and reducing their burden on public healthcare. If the current trend of the rising rate of NCDs continues, they could account for 86% of deaths by 2050 [3], emphasizing the need for better management through early diagnosis and prevention, which reduce the overall healthcare cost by avoiding potentially more expensive medical treatment [4–7]. However, conventional healthcare often fails to detect these diseases early enough since it prioritizes treatment of evident symptoms rather than preventive care due to limited or unavailable technology for real-time monitoring.

A key solution to building the urgently needed proactive healthcare systems is the implementation of WBANs [8]. The emergence of these networks has become possible owing to recent progress in microelectronics and IoT. Nevertheless, the sensors composing WBANs, especially biopotential and inertial sensors with a continuous signal nature, are strongly restricted in energy usage and data transmission rates [9, 10]. The energetic efficiency of these sensors can be improved significantly by reducing the quantity of acquired and wirelessly sent data in applications involving anomaly detection or event classification based on features extracted from corresponding signals. The conventional wireless sensor approach executes the feature extraction and classification at the aggregator and thus implies the power-hungry transmission of all samples acquired at the Nyquist rate to preserve the full signal information.

Moving at least the feature extraction operation inside the biopotential and inertial sensors should bring more benefits regarding their autonomy enhancement. Reviewing existing feature extraction and classification methods for two applications – arrhythmia diagnosis in ECG signals and HAR in inertial sensors – revealed their high computational cost and low flexibility application-wise. Thus, implementing such methods within sensor nodes is often energetically inefficient and hinders the development of low-power multimodal sensors embracing diverse types of signals and applications. The study of alternative acquisition techniques that allow capturing less information in the analog domain for further digitization showed the utility of the A2F conversion for the transmitted data amount and consumption reduction. This approach extracts only features relevant for classification from the analog signal directly

within the sensor [12]. Following the work carried out in [11], this thesis proposes to develop a reconfigurable generic A2F converter suitable for various types of low-frequency (below hundreds of kilohertz) signals and lay the foundation for its hardware implementation. For this purpose, we address two applications: binary arrhythmia detection in ECG signals and HAR in accelerometer and gyroscope signals. The developed converter leverages the NUWS-based feature extraction technique [13], adaptable to different types of signals thanks to its multiple degrees of freedom.

First of all, we described the chosen A2F architecture with multiple parallel feature extractors operating on the NUWS principle, each capable of extracting multiple non-overlapping features within a single analysis window. Then, we outlined the implementation workflow applied throughout the thesis. It includes the application-specific steps – data preparation, feature extraction, feature selection, and classification – and the definition of the hardware specifications for multi-application suitability. Data preparation accomplishes the operations of segmentation, annotation, and synchronization of the signals issued from datasets. The feature extraction step employs the NUWS technique that multiplies the segments of prepared data with generated tunable wavelets and integrates the result over the segment duration. The produced coefficients represent features that are fed to the next step of joint feature selection and classification. Namely, the preselected 100 best features according to the FS or IG criterion pass to an iterative construction of classifiers with the SFS algorithm (basic, adapted, or optimized version), which chooses the features for the classifier’s inputs that improve its prediction performance.

Based on the outlined workflow, we trained and evaluated classification models for both studied applications. In the binary arrhythmia detection case, the final classifier is obtained with the combination of IG preselection and optimized SFS algorithm and contains one hidden layer of ten neurons. At its inputs, it receives only eight of the available 502 features produced from the input ECG signals and Haar wavelet dictionary, which corresponds to a 96.9% reduction of the data amount compared to the Nyquist rate. This classifier achieves a 98.17% accuracy and a 92.62% sensitivity; the A2F converter requires three extractors to accommodate the chosen features and spends 2.6 μJ to extract and digitize them based on preliminary consumption estimations. In the multi-class HAR task, two final classifiers are obtained with the combination of IG preselection and adapted SFS algorithm and contain one hidden layer of 20 neurons. At their inputs, they receive 16 and 17 of available 1488 features produced from three input inertial signals ($acc_{x,y} + gyr_z$ and $acc_{x,y,z}$) and Haar wavelet dictionary, which corresponds to a 95.8% and 95.6% compression, respectively, compared to the Nyquist approach. These classifiers achieve 87.72% and 87.17% accuracies; the A2F converter requires eight extractors to accommodate the chosen features for either of the two cases.

To pave the way for the converter’s hardware implementation, we derived the specifications for its principal components, which include the amplification stage, analog mixer, wavelet generator, integrator, and ADC. Following the review of existing solutions for these

components, we performed the simulations at the schematic level of the G_m -C integrator, a critical component of the A2F converter, based on the design found in the literature. We determined its control and biasing voltages to achieve a sub-Hz cut-off frequency low enough for our needs. Next, we evaluated the NN classifiers with more realistic non-ideal integration coefficients from the simulated G_m -C integrator. The obtained results proved that classification algorithms can learn and accommodate the non-idealities introduced by at least such analog circuits as integrators. Therefore, A2F converters can help alleviate design limitations associated with analog circuits. Finally, based on the integrator's revised power consumption and the values borrowed from the state-of-the-art designs for other components, including the digital wavelet generator developed in [11], we estimated the energetic efficiency of our communication chain. We concluded that its consumption is divided by around 20 and five times compared to the Nyquist approach for the ECG and inertial signals, respectively. This fact highlights the potential of A2F conversion in achieving flexible, low-power WBAN sensors with a continuous signal nature in healthcare and other fields. Our system with in-sensor classification offers lower energetic efficiency than certain recent embedded designs implementing the studied applications. However, unlike these designs, it promises genericity and adaptability across different applications for various low-frequency signals while remaining relatively low-power.

Compared with the work carried out in [11], this thesis has made it possible to:

- re-implement feature extraction, feature selection, and classification in more advanced software to enhance the efficiency of the ML algorithms, particularly NNs, and speed up calculations using GPUs & re-produce the simulation results for binary arrhythmia detection in ECG signals with a slight improvement in classification performance;
- conduct a comprehensive study on a newly proposed application in the form of HAR in inertial signals with a focus on multi-class classification to prove the genericity of the developed A2F converter;
- perform a circuit-level design of a critical converter's component, G_m -C integrator, that provides a significantly low sub-Hz cut-off frequency to suit both explored applications;
- evaluate the NN classifiers with more realistic non-ideal integration coefficients, i.e., features to show the ability of the NUWS-based A2F converter to mitigate design constraints imposed on such analog circuits as integrators;
- estimate the energetic efficiency of the communication chain with the A2F conversion and compare it to recent embedded designs with in-sensor classification.

Perspectives

This study contributes to a founding step towards implementing reconfigurable generic A2F converters in WBAN sensors for healthcare and beyond, but several challenges and potential improvements remain for future work:

- completion of the circuit design with all converter components and its physical implementation in a single chip based on a mature 180 nm CMOS technology or a smaller, more advanced node offering more compact and power-efficient digital circuitry. This step would demonstrate the benefit of the A2F conversion for WBAN sensors in practice;
- optimization of signal conditioning and feature extraction circuitry coupled with an improved power-aware feature selection algorithm based on the complete A2F converter's circuit simulations would reduce the consumption associated with signal acquisition, which takes up to 99.9% of total consumption in sensors employing the A2F conversion according to our estimations;
- implementation of a digital or analog NN within the sensor node;
- re-evaluation of the constructed NN classifiers' performance with the noise introduced in the analyzed dataset signals to check the converter's robustness to noise;
- more profound analysis of anomalies and arrhythmias in ECG signals through multi-class classification for further exploration of feature extractors' reconfigurability;
- study of the potential for real-time HAR and multimodal data fusion for the developed system by switching to a more comprehensive dataset, such as CSL-SHARE [168];
- improving the already achieved classification performances of the multi-class HAR with a more complex but efficient NN structure or feature stacking that combines several classifier models. Another research direction is to address the modification of the optimized SFS algorithm's original evaluation metric or implement the SFFS feature selection procedure instead, which could tackle the limitation of achievable classification accuracy in favor of energy reduction while applying the optimized SFS to the multi-class HAR;
- consideration of other types of signals, sensors, and applications for a broader exploration of the converter's genericity.

Bibliography

- [1] “World Population Prospects 2024 | Population Division.” [Online]. Available: <https://www.un.org/development/desa/pd/world-population-prospects-2024>
- [2] “Non communicable diseases.” [Online]. Available: <https://www.who.int/news-room/fact-sheets/detail/noncommunicable-diseases>
- [3] “Chronic diseases taking ‘immense and increasing toll on lives’, warns WHO | UN News,” May 2023. [Online]. Available: <https://news.un.org/en/story/2023/05/1136832>
- [4] D. S. Celermajer, C. K. Chow, E. Marijon, N. M. Anstey, and K. S. Woo, “Cardiovascular Disease in the Developing World,” *Journal of the American College of Cardiology*, vol. 60, no. 14, pp. 1207–1216, Oct. 2012. [Online]. Available: <https://www.jacc.org/doi/full/10.1016/j.jacc.2012.03.074>
- [5] D. Crosby, S. Bhatia, K. M. Brindle, L. M. Coussens, C. Dive, M. Emberton, S. Esener, R. C. Fitzgerald, S. S. Gambhir, P. Kuhn, T. R. Rebbeck, and S. Balasubramanian, “Early detection of cancer,” *Science*, vol. 375, no. 6586, p. eaay9040, Mar. 2022. [Online]. Available: <https://www.science.org/doi/full/10.1126/science.aay9040>
- [6] J. B. Soriano, J. Zielinski, and D. Price, “Screening for and early detection of chronic obstructive pulmonary disease,” *The Lancet*, vol. 374, no. 9691, pp. 721–732, Aug. 2009. [Online]. Available: [https://www.thelancet.com/journals/lancet/article/PIIS0140-6736\(09\)61290-3/fulltext](https://www.thelancet.com/journals/lancet/article/PIIS0140-6736(09)61290-3/fulltext)
- [7] W. C. Knowler, E. Barrett-Connor, S. E. Fowler, R. F. Hamman, J. M. Lachin, E. A. Walker, D. M. Nathan, and Diabetes Prevention Program Research Group, “Reduction in the incidence of type 2 diabetes with lifestyle intervention or metformin,” *The New England Journal of Medicine*, vol. 346, no. 6, pp. 393–403, Feb. 2002.
- [8] S. Movassaghi, M. Abolhasan, J. Lipman, D. Smith, and A. Jamalipour, “Wireless Body Area Networks: A Survey,” *IEEE Communications Surveys & Tutorials*, vol. 16, no. 3, pp. 1658–1686, 2014. [Online]. Available: <https://ieeexplore.ieee.org/document/6710228>
- [9] R. Goyal, N. Mittal, L. Gupta, and A. Surana, “Routing Protocols in Wireless Body Area Networks: Architecture, Challenges, and Classification,” *Wireless Communications and Mobile Computing*, vol. 2023, no. 1, p. 9229297, 2023. [Online]. Available: <https://onlinelibrary.wiley.com/doi/abs/10.1155/2023/9229297>
- [10] L. Zhong, S. He, J. Lin, J. Wu, X. Li, Y. Pang, and Z. Li, “Technological Requirements and Challenges in Wireless Body Area Networks for Health Monitoring:

- A Comprehensive Survey,” *Sensors*, vol. 22, no. 9, p. 3539, Jan. 2022. [Online]. Available: <https://www.mdpi.com/1424-8220/22/9/3539>
- [11] A. Back, “Conception et intégration d’un convertisseur analogique-paramètres flexible pour les capteurs intelligents,” PhD thesis, Institut polytechnique de Paris, Feb. 2022. [Online]. Available: <https://theses.fr/2022IPPAT020>
- [12] B. Rumberg, D. W. Graham, V. Kulathumani, and R. Fernandez, “Hibernets: Energy-Efficient Sensor Networks Using Analog Signal Processing,” *IEEE Journal on Emerging and Selected Topics in Circuits and Systems*, vol. 1, no. 3, pp. 321–334, Sep. 2011. [Online]. Available: <https://ieeexplore.ieee.org/document/6018315>
- [13] M. Pelissier and C. Studer, “Non-Uniform Wavelet Sampling for RF Analog-to-Information Conversion,” *IEEE Transactions on Circuits and Systems I: Regular Papers*, vol. 65, no. 2, pp. 471–484, Feb. 2018. [Online]. Available: <https://ieeexplore.ieee.org/document/8015153>
- [14] “The top 10 causes of death.” [Online]. Available: <https://www.who.int/news-room/fact-sheets/detail/the-top-10-causes-of-death>
- [15] “World health statistics 2024: Monitoring health for the SDGs, sustainable development goals.” [Online]. Available: <https://www.who.int/publications/i/item/9789240094703>
- [16] S. R. Jino Ramson and D. J. Moni, “Applications of wireless sensor networks — A survey,” in *2017 International Conference on Innovations in Electrical, Electronics, Instrumentation and Media Technology (ICEEIMT)*, Feb. 2017, pp. 325–329. [Online]. Available: <https://ieeexplore.ieee.org/document/8116858>
- [17] D. Davcev, K. Mitreski, S. Trajkovic, V. Nikolovski, and N. Koteli, “IoT agriculture system based on LoRaWAN,” in *2018 14th IEEE International Workshop on Factory Communication Systems (WFCS)*, Jun. 2018, pp. 1–4. [Online]. Available: <https://ieeexplore.ieee.org/document/8402368>
- [18] M. Pech, J. Vrchota, and J. Bednář, “Predictive Maintenance and Intelligent Sensors in Smart Factory: Review,” *Sensors*, vol. 21, no. 4, p. 1470, Jan. 2021. [Online]. Available: <https://www.mdpi.com/1424-8220/21/4/1470>
- [19] J. Guerrero-Ibáñez, S. Zeadally, and J. Contreras-Castillo, “Sensor Technologies for Intelligent Transportation Systems,” *Sensors*, vol. 18, no. 4, p. 1212, Apr. 2018. [Online]. Available: <https://www.mdpi.com/1424-8220/18/4/1212>
- [20] D. Gil, A. Ferrández, H. Mora-Mora, and J. Peral, “Internet of Things: A Review of Surveys Based on Context Aware Intelligent Services,” *Sensors*, vol. 16, no. 7, p. 1069, Jul. 2016. [Online]. Available: <https://www.mdpi.com/1424-8220/16/7/1069>
- [21] M. Ciolacu, A. F. Tehrani, L. Binder, and P. M. Svasta, “Education 4.0 - Artificial Intelligence Assisted Higher Education: Early recognition System with Machine Learning to support Students’ Success,” in *2018 IEEE 24th International Symposium for Design and Technology in Electronic Packaging (SIITME)*, Oct. 2018, pp. 23–30. [Online]. Available: <https://ieeexplore.ieee.org/document/8599203>

- [22] E. Mbunge, B. Muchemwa, S. Jiyane, and J. Batani, "Sensors and healthcare 5.0: Transformative shift in virtual care through emerging digital health technologies," *Global Health Journal*, vol. 5, no. 4, pp. 169–177, Dec. 2021. [Online]. Available: <https://www.sciencedirect.com/science/article/pii/S2414644721000932>
- [23] "IEEE Standard for Local and metropolitan area networks - Part 15.6: Wireless Body Area Networks," *IEEE Std 802.15.6-2012*, pp. 1–271, Feb. 2012. [Online]. Available: <https://ieeexplore.ieee.org/document/6161600>
- [24] H. Taleb, A. Nasser, G. Andrieux, N. Charara, and E. Motta Cruz, "Wireless technologies, medical applications and future challenges in WBAN: A survey," *Wireless Networks*, vol. 27, no. 8, pp. 5271–5295, Nov. 2021. [Online]. Available: <https://doi.org/10.1007/s11276-021-02780-2>
- [25] R. Punj and R. Kumar, "Technological aspects of WBANs for health monitoring: A comprehensive review," *Wireless Networks*, vol. 25, no. 3, pp. 1125–1157, Apr. 2019. [Online]. Available: <https://doi.org/10.1007/s11276-018-1694-3>
- [26] X. Lai, Q. Liu, X. Wei, W. Wang, G. Zhou, and G. Han, "A Survey of Body Sensor Networks," *Sensors*, vol. 13, no. 5, pp. 5406–5447, May 2013. [Online]. Available: <https://www.mdpi.com/1424-8220/13/5/5406>
- [27] H. S. Bindra, A.-J. Annema, S. M. Louwsma, and B. Nauta, "A 0.2 - 8 MS/s 10b flexible SAR ADC achieving 0.35 - 2.5 fJ/conv-step and using self-quenched dynamic bias comparator," in *2019 Symposium on VLSI Circuits*, Jun. 2019, pp. C74–C75. [Online]. Available: <https://ieeexplore.ieee.org/document/8778093>
- [28] M. Zhang, C.-H. Chan, Y. Zhu, and R. P. Martins, "3.5 A 0.6V 13b 20MS/s Two-Step TDC-Assisted SAR ADC with PVT Tracking and Speed-Enhanced Techniques," in *2019 IEEE International Solid-State Circuits Conference - (ISSCC)*, Feb. 2019, pp. 66–68. [Online]. Available: <https://ieeexplore.ieee.org/document/8662350>
- [29] Z. Chen, L. Shen, S. Ye, J. Gao, J. Li, J. Cui, X. Xu, Y. Luan, H. Zhang, L. Ye, and R. Huang, "9.4 A 182.3dB FoMs 50MS/s Pipelined-SAR ADC using Cascode Capacitively Degenerated Dynamic Amplifier and MSB Pre-Conversion Technique," in *2024 IEEE International Solid-State Circuits Conference (ISSCC)*, vol. 67, Feb. 2024, pp. 174–176. [Online]. Available: <https://ieeexplore.ieee.org/document/10454297>
- [30] C.-C. Liu, "27.4 A 0.35mW 12b 100MS/s SAR-assisted digital slope ADC in 28nm CMOS," in *2016 IEEE International Solid-State Circuits Conference (ISSCC)*, Jan. 2016, pp. 462–463. [Online]. Available: <https://ieeexplore.ieee.org/abstract/document/7418107>
- [31] S.-E. Hsieh, T.-C. Wu, and C.-C. Hou, "A 1.8GHz 12b Pre-Sampling Pipelined ADC with Reference Buffer and OP Power Relaxations," in *2023 IEEE International Solid-State Circuits Conference (ISSCC)*, Feb. 2023, pp. 166–168. [Online]. Available: <https://ieeexplore.ieee.org/document/10067258>

- [32] H. Zhang, Y. Zhu, C.-H. Chan, and R. P. Martins, "27.6 A 25MHz-BW 75dB-SNDR Inherent Gain Error Tolerance Noise-Shaping SAR-Assisted Pipeline ADC with Background Offset Calibration," in *2021 IEEE International Solid-State Circuits Conference (ISSCC)*, vol. 64, Feb. 2021, pp. 380–382. [Online]. Available: <https://ieeexplore.ieee.org/document/9365833>
- [33] P. Cenci, M. Bolatkale, R. Rutten, M. Ganzerli, G. Lassche, K. Makinwa, and L. Breems, "A 3.2mW SAR-assisted $CT\Delta\Sigma$ ADC with 77.5dB SNDR and 40MHz BW in 28nm CMOS," in *2019 Symposium on VLSI Circuits*, Jun. 2019, pp. C230–C231. [Online]. Available: <https://ieeexplore.ieee.org/document/8778176>
- [34] J.-C. Wang and T.-H. Kuo, "A 3mW 2.7GS/s 8b Subranging ADC with Multiple-Reference-Reference-Embedded Comparators," in *2023 IEEE International Solid-State Circuits Conference (ISSCC)*, Feb. 2023, pp. 276–278. [Online]. Available: <https://ieeexplore.ieee.org/document/10067498>
- [35] D.-R. Oh, K.-J. Moon, W.-M. Lim, Y.-D. Kim, E.-J. An, and S.-T. Ryu, "An 8b 1GS/s 2.55mW SAR-Flash ADC with Complementary Dynamic Amplifiers," in *2020 IEEE Symposium on VLSI Circuits*, Jun. 2020, pp. 1–2. [Online]. Available: <https://ieeexplore.ieee.org/document/9163064>
- [36] V. H.-C. Chen and L. Pileggi, "An 8.5mW 5GS/s 6b flash ADC with dynamic offset calibration in 32nm CMOS SOI," in *2013 Symposium on VLSI Circuits*, Jun. 2013, pp. C264–C265. [Online]. Available: <https://ieeexplore.ieee.org/document/6578688>
- [37] B. Murmann, "ADC Performance Survey 1997-2024." [Online]. Available: <https://github.com/bmurmann/ADC-survey>
- [38] F.-W. Kuo, S. Binsfeld Ferreira, H.-N. R. Chen, L.-C. Cho, C.-P. Jou, F.-L. Hsueh, I. Madadi, M. Tohidian, M. Shahmohammadi, M. Babaie, and R. B. Staszewski, "A Bluetooth Low-Energy Transceiver With 3.7-mW All-Digital Transmitter, 2.75-mW High-IF Discrete-Time Receiver, and TX/RX Switchable On-Chip Matching Network," *IEEE Journal of Solid-State Circuits*, vol. 52, no. 4, pp. 1144–1162, Apr. 2017. [Online]. Available: <https://ieeexplore.ieee.org/document/7862859>
- [39] X. Chen, J. Breiholz, F. B. Yahya, C. J. Lukas, H.-S. Kim, B. H. Calhoun, and D. D. Wentzloff, "Analysis and Design of an Ultra-Low-Power Bluetooth Low-Energy Transmitter With Ring Oscillator-Based ADPLL and 4 \times Frequency Edge Combiner," *IEEE Journal of Solid-State Circuits*, vol. 54, no. 5, pp. 1339–1350, May 2019. [Online]. Available: <https://ieeexplore.ieee.org/abstract/document/8653480>
- [40] X. Chen, A. Alghaihab, Y. Shi, D. S. Truesdell, B. H. Calhoun, and D. D. Wentzloff, "A Crystal-Less BLE Transmitter With Clock Recovery From GFSK-Modulated BLE Packets," *IEEE Journal of Solid-State Circuits*, vol. 56, no. 7, pp. 1963–1974, Jul. 2021. [Online]. Available: <https://ieeexplore.ieee.org/document/9321145>
- [41] Y. Shi, X. Chen, H.-S. Kim, D. Blaauw, and D. Wentzloff, "28.3 A 606 μ W mm-Scale Bluetooth Low-Energy Transmitter Using Co-Designed 3.5 \times 3.5mm² Loop

- Antenna and Transformer-Boost Power Oscillator,” in *2019 IEEE International Solid-State Circuits Conference - (ISSCC)*, Feb. 2019, pp. 442–444. [Online]. Available: <https://ieeexplore.ieee.org/document/8662333>
- [42] L.-H. Wang, T.-Y. Chen, K.-H. Lin, Q. Fang, and S.-Y. Lee, “Implementation of a Wireless ECG Acquisition SoC for IEEE 802.15.4 (ZigBee) Applications,” *IEEE Journal of Biomedical and Health Informatics*, vol. 19, no. 1, pp. 247–255, Jan. 2015. [Online]. Available: <https://ieeexplore.ieee.org/document/6762822>
- [43] G. Singh, E. Allebes, Y. He, E. Tiurin, P. Mateman, J. F. Dijkhuis, G.-J. van Schaik, E. Bechthum, J. van den Heuvel, M. El Soussi, A. Breeschoten, H. Korpela, G.-J. Gordebeke, S. Lemey, C. Bachmann, and Y.-H. Liu, “An IR-UWB IEEE 802.15.4z Compatible Coherent Asynchronous Polar Transmitter in 28-nm CMOS,” *IEEE Journal of Solid-State Circuits*, vol. 56, no. 12, pp. 3799–3810, Dec. 2021. [Online]. Available: <https://ieeexplore.ieee.org/abstract/document/9568648>
- [44] K.-S. Choi, J. Ko, K.-M. Kim, J. Kim, and S.-G. Lee, “A 0.3-to-1-GHz IoT Transmitter Employing Pseudo-Randomized Phase Switching Modulator and Single-Supply Class-G Harmonic Rejection PA,” *IEEE Journal of Solid-State Circuits*, vol. 57, no. 3, pp. 892–905, Mar. 2022. [Online]. Available: <https://ieeexplore.ieee.org/document/9497329>
- [45] M. A. A. Ibrahim and M. Onabajo, “A Low-Power BFSK Transmitter Architecture for Biomedical Applications,” *IEEE Transactions on Circuits and Systems I: Regular Papers*, vol. 67, no. 5, pp. 1527–1540, May 2020. [Online]. Available: <https://ieeexplore.ieee.org/document/8943330>
- [46] M. Rahman and R. Harjani, “A 2.4GHz IEEE 802.15.6 Compliant 1.52nJ/bit TX & 1.32nJ/bit RX Multiband Transceiver for Low Power Standards,” in *2018 25th IEEE International Conference on Electronics, Circuits and Systems (ICECS)*, Dec. 2018, pp. 821–824. [Online]. Available: <https://ieeexplore.ieee.org/document/8617891>
- [47] B. Chatterjee, A. Srivastava, D.-H. Seo, D. Yang, and S. Sen, “A Context-aware Reconfigurable Transmitter with 2.24 pJ/bit, 802.15.6 NB-HBC and 4.93 pJ/bit, 400.9 MHz MedRadio Modes with 33.6% Transmit Efficiency,” in *2020 IEEE Radio Frequency Integrated Circuits Symposium (RFIC)*, Aug. 2020, pp. 75–78. [Online]. Available: <https://ieeexplore.ieee.org/document/9218344>
- [48] B. Chatterjee, A. Datta, M. Nath, G. K. K, N. Modak, and S. Sen, “A 65nm 63.3 μ W 15Mbps Transceiver with Switched-Capacitor Adiabatic Signaling and Combinatorial-Pulse-Position Modulation for Body-Worn Video-Sensing AR Nodes,” in *2022 IEEE International Solid-State Circuits Conference (ISSCC)*, vol. 65, Feb. 2022, pp. 276–278. [Online]. Available: <https://ieeexplore.ieee.org/document/9731793>
- [49] “Bluetooth Technology Overview.” [Online]. Available: <https://www.bluetooth.com/learn-about-bluetooth/tech-overview/>
- [50] N. Verma, A. Shoeb, J. Bohorquez, J. Dawson, J. Gutttag, and A. P. Chandrakasan, “A Micro-Power EEG Acquisition SoC With Integrated Feature

- Extraction Processor for a Chronic Seizure Detection System,” *IEEE Journal of Solid-State Circuits*, vol. 45, no. 4, pp. 804–816, Apr. 2010. [Online]. Available: <https://ieeexplore.ieee.org/document/5437484>
- [51] S. Cho, H. Han, H. Park, S.-U. Lee, J.-H. Kim, S. W. Jeon, M. Wang, R. Avila, Z. Xi, K. Ko, M. Park, J. Lee, M. Choi, J.-S. Lee, W. G. Min, B.-J. Lee, S. Lee, J. Choi, J. Gu, J. Park, M. S. Kim, J. Ahn, O. Gul, C. Han, G. Lee, S. Kim, K. Kim, J. Kim, C.-M. Kang, J. Koo, S. S. Kwak, S. Kim, D. Y. Choi, S. Jeon, H. J. Sung, Y. B. Park, M. Je, Y. T. Cho, Y. S. Oh, and I. Park, “Wireless, multimodal sensors for continuous measurement of pressure, temperature, and hydration of patients in wheelchair,” *npj Flexible Electronics*, vol. 7, no. 1, pp. 1–15, Feb. 2023. [Online]. Available: <https://www.nature.com/articles/s41528-023-00238-3>
- [52] H. F. Nweke, Y. W. Teh, G. Mujtaba, and M. A. Al-garadi, “Data fusion and multiple classifier systems for human activity detection and health monitoring: Review and open research directions,” *Information Fusion*, vol. 46, pp. 147–170, Mar. 2019. [Online]. Available: <https://www.sciencedirect.com/science/article/pii/S1566253518304135>
- [53] T. M. Mitchell, *Machine Learning*, ser. McGraw-Hill Series in Computer Science. New York: McGraw-Hill, 1997.
- [54] M. I. Jordan and T. M. Mitchell, “Machine learning: Trends, perspectives, and prospects,” *Science*, vol. 349, no. 6245, pp. 255–260, Jul. 2015. [Online]. Available: <https://www.science.org/doi/abs/10.1126/science.aaa8415>
- [55] P. Cunningham, M. Cord, and S. J. Delany, “Supervised Learning,” in *Machine Learning Techniques for Multimedia: Case Studies on Organization and Retrieval*, M. Cord and P. Cunningham, Eds. Berlin, Heidelberg: Springer, 2008, pp. 21–49. [Online]. Available: https://doi.org/10.1007/978-3-540-75171-7_2
- [56] B. W. Matthews, “Comparison of the predicted and observed secondary structure of T4 phage lysozyme,” *Biochimica et Biophysica Acta (BBA) - Protein Structure*, vol. 405, no. 2, pp. 442–451, Oct. 1975. [Online]. Available: <https://www.sciencedirect.com/science/article/pii/0005279575901099>
- [57] D. Chicco and G. Jurman, “The advantages of the Matthews correlation coefficient (MCC) over F1 score and accuracy in binary classification evaluation,” *BMC Genomics*, vol. 21, no. 1, p. 6, Jan. 2020. [Online]. Available: <https://doi.org/10.1186/s12864-019-6413-7>
- [58] D. Chicco, N. Tötsch, and G. Jurman, “The Matthews correlation coefficient (MCC) is more reliable than balanced accuracy, bookmaker informedness, and markedness in two-class confusion matrix evaluation,” *BioData Mining*, vol. 14, no. 1, p. 13, Feb. 2021. [Online]. Available: <https://doi.org/10.1186/s13040-021-00244-z>
- [59] D. Chicco and G. Jurman, “The Matthews correlation coefficient (MCC) should replace the ROC AUC as the standard metric for assessing binary

- classification,” *BioData Mining*, vol. 16, p. 4, Feb. 2023. [Online]. Available: <https://www.ncbi.nlm.nih.gov/pmc/articles/PMC9938573/>
- [60] J. Yang, K. Ye, R. Zhang, X. Fan, R. Xiong, S. Zhang, Q. Liu, M. Lin, B. Wang, X. Tan, Q. Wen, and X. Ou, “The characteristics and molecular targets of antiarrhythmic natural products,” *Biomedicine & Pharmacotherapy*, vol. 168, p. 115762, Dec. 2023. [Online]. Available: <https://www.sciencedirect.com/science/article/pii/S0753332223015603>
- [61] “Arrhythmias - What Is an Arrhythmia? | NHLBI, NIH,” Mar. 2022. [Online]. Available: <https://www.nhlbi.nih.gov/health/arrhythmias>
- [62] L. J. Gessman, P. N. Schacknow, and R. G. Brindis, “Sudden Cardiac Death at Home: Potential Lives Saved With Fully Automated External Defibrillators,” *Annals of Emergency Medicine*, vol. 83, no. 1, pp. 35–41, Jan. 2024. [Online]. Available: <https://www.sciencedirect.com/science/article/pii/S0196064423006455>
- [63] A.-A. EC57, “Testing and reporting performance results of cardiac rhythm and st segment measurement algorithms,” *Association for the Advancement of Medical Instrumentation, Arlington, VA*, 1998.
- [64] E. Merdjanovska and A. Rashkovska, “Comprehensive survey of computational ECG analysis: Databases, methods and applications,” *Expert Systems with Applications*, vol. 203, p. 117206, Oct. 2022. [Online]. Available: <https://www.sciencedirect.com/science/article/pii/S0957417422005917>
- [65] A. Rashkovska, M. Depolli, I. Tomašić, V. Avbelj, and R. Trobec, “Medical-Grade ECG Sensor for Long-Term Monitoring,” *Sensors*, vol. 20, no. 6, p. 1695, Jan. 2020. [Online]. Available: <https://www.mdpi.com/1424-8220/20/6/1695>
- [66] M. Wasimuddin, K. Elleithy, A.-S. Abuzneid, M. Faezipour, and O. Abuzagheh, “Stages-Based ECG Signal Analysis From Traditional Signal Processing to Machine Learning Approaches: A Survey,” *IEEE Access*, vol. 8, pp. 177 782–177 803, 2020. [Online]. Available: <https://ieeexplore.ieee.org/document/9206538>
- [67] A. Boulif, B. Ananou, M. Ouladsine, and S. Delliaux, “A Literature Review: ECG-Based Models for Arrhythmia Diagnosis Using Artificial Intelligence Techniques,” *Bioinformatics and Biology Insights*, vol. 17, p. 11779322221149600, Jan. 2023. [Online]. Available: <https://doi.org/10.1177/11779322221149600>
- [68] G. Moody and R. Mark, “The impact of the MIT-BIH Arrhythmia Database,” *IEEE Engineering in Medicine and Biology Magazine*, vol. 20, no. 3, pp. 45–50, May 2001. [Online]. Available: <https://ieeexplore.ieee.org/document/932724>
- [69] Ö. Yildirim, “A novel wavelet sequence based on deep bidirectional LSTM network model for ECG signal classification,” *Computers in Biology and Medicine*, vol. 96, pp. 189–202, May 2018. [Online]. Available: <https://www.sciencedirect.com/science/article/pii/S0010482518300738>

- [70] J. Gao, H. Zhang, P. Lu, and Z. Wang, "An Effective LSTM Recurrent Network to Detect Arrhythmia on Imbalanced ECG Dataset," *Journal of Healthcare Engineering*, vol. 2019, no. 1, p. 6320651, 2019. [Online]. Available: <https://onlinelibrary.wiley.com/doi/abs/10.1155/2019/6320651>
- [71] H. Li, D. Yuan, Y. Wang, D. Cui, and L. Cao, "Arrhythmia Classification Based on Multi-Domain Feature Extraction for an ECG Recognition System," *Sensors*, vol. 16, no. 10, p. 1744, Oct. 2016. [Online]. Available: <https://www.mdpi.com/1424-8220/16/10/1744>
- [72] S. M. Anwar, M. Gul, M. Majid, and M. Alnowami, "Arrhythmia Classification of ECG Signals Using Hybrid Features," *Computational and Mathematical Methods in Medicine*, vol. 2018, no. 1, p. 1380348, 2018. [Online]. Available: <https://onlinelibrary.wiley.com/doi/abs/10.1155/2018/1380348>
- [73] F. A. Elhaj, N. Salim, A. R. Harris, T. T. Swee, and T. Ahmed, "Arrhythmia recognition and classification using combined linear and nonlinear features of ECG signals," *Computer Methods and Programs in Biomedicine*, vol. 127, pp. 52–63, Apr. 2016. [Online]. Available: <https://www.sciencedirect.com/science/article/pii/S0169260715301097>
- [74] S. Raj and K. C. Ray, "Automated recognition of cardiac arrhythmias using sparse decomposition over composite dictionary," *Computer Methods and Programs in Biomedicine*, vol. 165, pp. 175–186, Oct. 2018. [Online]. Available: <https://www.sciencedirect.com/science/article/pii/S0169260718307260>
- [75] R. Rajagopal and V. Ranganathan, "Design of a hybrid model for cardiac arrhythmia classification based on Daubechies wavelet transform," *Advances in Clinical and Experimental Medicine*, vol. 27, no. 6, pp. 727–734, 2018. [Online]. Available: <https://advances.umw.edu.pl/en/article/2018/27/6/727/>
- [76] K. N. V. P. S. Rajesh and R. Dhuli, "Classification of ECG heartbeats using nonlinear decomposition methods and support vector machine," *Computers in Biology and Medicine*, vol. 87, pp. 271–284, Aug. 2017. [Online]. Available: <https://www.sciencedirect.com/science/article/pii/S0010482517301701>
- [77] W. Ullah, I. Siddique, R. M. Zulqarnain, M. M. Alam, I. Ahmad, and U. A. Raza, "Classification of Arrhythmia in Heartbeat Detection Using Deep Learning," *Computational Intelligence and Neuroscience*, vol. 2021, no. 1, p. 2195922, 2021. [Online]. Available: <https://onlinelibrary.wiley.com/doi/abs/10.1155/2021/2195922>
- [78] S. Ma, J. Cui, W. Xiao, and L. Liu, "Deep Learning-Based Data Augmentation and Model Fusion for Automatic Arrhythmia Identification and Classification Algorithms," *Computational Intelligence and Neuroscience*, vol. 2022, no. 1, p. 1577778, 2022. [Online]. Available: <https://onlinelibrary.wiley.com/doi/abs/10.1155/2022/1577778>
- [79] J. Wang, "Automated detection of premature ventricular contraction based on the improved gated recurrent unit network," *Computer Methods and Programs*

- in Biomedicine*, vol. 208, p. 106284, Sep. 2021. [Online]. Available: <https://www.sciencedirect.com/science/article/pii/S0169260721003588>
- [80] O. Yildirim, U. B. Baloglu, R.-S. Tan, E. J. Ciaccio, and U. R. Acharya, “A new approach for arrhythmia classification using deep coded features and LSTM networks,” *Computer Methods and Programs in Biomedicine*, vol. 176, pp. 121–133, Jul. 2019. [Online]. Available: <https://www.sciencedirect.com/science/article/pii/S0169260718314329>
- [81] Ö. Yıldırım, P. Pławiak, R.-S. Tan, and U. R. Acharya, “Arrhythmia detection using deep convolutional neural network with long duration ECG signals,” *Computers in Biology and Medicine*, vol. 102, pp. 411–420, Nov. 2018. [Online]. Available: <https://www.sciencedirect.com/science/article/pii/S0010482518302713>
- [82] S. L. Oh, E. Y. K. Ng, R. S. Tan, and U. R. Acharya, “Automated diagnosis of arrhythmia using combination of CNN and LSTM techniques with variable length heart beats,” *Computers in Biology and Medicine*, vol. 102, pp. 278–287, Nov. 2018. [Online]. Available: <https://www.sciencedirect.com/science/article/pii/S0010482518301446>
- [83] Q. Qin, J. Li, L. Zhang, Y. Yue, and C. Liu, “Combining Low-dimensional Wavelet Features and Support Vector Machine for Arrhythmia Beat Classification,” *Scientific Reports*, vol. 7, no. 1, p. 6067, Jul. 2017. [Online]. Available: <https://www.nature.com/articles/s41598-017-06596-z>
- [84] M. Zubair and C. Yoon, “Cost-Sensitive Learning for Anomaly Detection in Imbalanced ECG Data Using Convolutional Neural Networks,” *Sensors*, vol. 22, no. 11, p. 4075, Jan. 2022. [Online]. Available: <https://www.mdpi.com/1424-8220/22/11/4075>
- [85] R. Hu, J. Chen, and L. Zhou, “A transformer-based deep neural network for arrhythmia detection using continuous ECG signals,” *Computers in Biology and Medicine*, vol. 144, p. 105325, May 2022. [Online]. Available: <https://www.sciencedirect.com/science/article/pii/S0010482522001172>
- [86] G. Chen, Z. Hong, Y. Guo, and C. Pang, “A cascaded classifier for multi-lead ECG based on feature fusion,” *Computer Methods and Programs in Biomedicine*, vol. 178, pp. 135–143, Sep. 2019. [Online]. Available: <https://www.sciencedirect.com/science/article/pii/S0169260719305747>
- [87] W. Yang, Y. Si, D. Wang, and G. Zhang, “A Novel Approach for Multi-Lead ECG Classification Using DL-CCANet and TL-CCANet,” *Sensors*, vol. 19, no. 14, p. 3214, Jan. 2019. [Online]. Available: <https://www.mdpi.com/1424-8220/19/14/3214>
- [88] S. Irfan, N. Anjum, T. Althobaiti, A. A. Alotaibi, A. B. Siddiqui, and N. Ramzan, “Heartbeat Classification and Arrhythmia Detection Using a Multi-Model Deep-Learning Technique,” *Sensors*, vol. 22, no. 15, p. 5606, Jan. 2022. [Online]. Available: <https://www.mdpi.com/1424-8220/22/15/5606>
- [89] S. Chatterjee, R. S. Thakur, R. N. Yadav, L. Gupta, and D. K. Raghuvanshi, “Review of noise removal techniques in ECG signals,” *IET Signal Processing*, vol. 14, no. 9, pp.

- 569–590, 2020. [Online]. Available: <https://onlinelibrary.wiley.com/doi/abs/10.1049/iet-spr.2020.0104>
- [90] Q. Xiao, K. Lee, S. A. Mokhtar, I. Ismail, A. L. b. M. Pauzi, Q. Zhang, and P. Y. Lim, “Deep Learning-Based ECG Arrhythmia Classification: A Systematic Review,” *Applied Sciences*, vol. 13, no. 8, p. 4964, Jan. 2023. [Online]. Available: <https://www.mdpi.com/2076-3417/13/8/4964>
- [91] Q. Yao, R. Wang, X. Fan, J. Liu, and Y. Li, “Multi-class Arrhythmia detection from 12-lead varied-length ECG using Attention-based Time-Incremental Convolutional Neural Network,” *Information Fusion*, vol. 53, pp. 174–182, Jan. 2020. [Online]. Available: <https://www.sciencedirect.com/science/article/pii/S1566253518307632>
- [92] N. V. Chawla, K. W. Bowyer, L. O. Hall, and W. P. Kegelmeyer, “SMOTE: Synthetic Minority Over-sampling Technique,” *Journal of Artificial Intelligence Research*, vol. 16, pp. 321–357, Jun. 2002. [Online]. Available: <http://arxiv.org/abs/1106.1813>
- [93] J. He, J. Rong, L. Sun, H. Wang, Y. Zhang, and J. Ma, “A framework for cardiac arrhythmia detection from IoT-based ECGs,” *World Wide Web*, vol. 23, no. 5, pp. 2835–2850, Sep. 2020. [Online]. Available: <https://doi.org/10.1007/s11280-019-00776-9>
- [94] H. M. Balaha and A. E.-S. Hassan, “Comprehensive machine and deep learning analysis of sensor-based human activity recognition,” *Neural Computing and Applications*, vol. 35, no. 17, pp. 12 793–12 831, Jun. 2023. [Online]. Available: <https://doi.org/10.1007/s00521-023-08374-7>
- [95] V. Dentamaro, V. Gattulli, D. Impedovo, and F. Manca, “Human activity recognition with smartphone-integrated sensors: A survey,” *Expert Systems with Applications*, vol. 246, p. 123143, Jul. 2024. [Online]. Available: <https://www.sciencedirect.com/science/article/pii/S0957417424000083>
- [96] M. A. A. Al-qaness, A. Dahou, M. A. Elaziz, and A. M. Helmi, “Multi-ResAtt: Multilevel Residual Network With Attention for Human Activity Recognition Using Wearable Sensors,” *IEEE Transactions on Industrial Informatics*, vol. 19, no. 1, pp. 144–152, Jan. 2023. [Online]. Available: <https://ieeexplore.ieee.org/document/9754268>
- [97] F. Demrozi, G. Pravadelli, A. Bihorac, and P. Rashidi, “Human Activity Recognition Using Inertial, Physiological and Environmental Sensors: A Comprehensive Survey,” *IEEE Access*, vol. 8, pp. 210 816–210 836, 2020. [Online]. Available: <https://ieeexplore.ieee.org/abstract/document/9257355>
- [98] W. Gomaa and M. A. Khamis, “A perspective on human activity recognition from inertial motion data,” *Neural Computing and Applications*, vol. 35, no. 28, pp. 20 463–20 568, Oct. 2023. [Online]. Available: <https://doi.org/10.1007/s00521-023-08863-9>
- [99] D. A. Jorge Reyes-Ortiz, “Human Activity Recognition Using Smartphones,” 2013. [Online]. Available: <https://archive.ics.uci.edu/dataset/240>
- [100] Y. Yin, L. Xie, Z. Jiang, F. Xiao, J. Cao, and S. Lu, “A Systematic Review of Human Activity Recognition Based on Mobile Devices: Overview, Progress and Trends,” *IEEE*

- Communications Surveys & Tutorials*, vol. 26, no. 2, pp. 890–929, 2024. [Online]. Available: <https://ieeexplore.ieee.org/document/10413312>
- [101] A. Ignatov, “Real-time human activity recognition from accelerometer data using Convolutional Neural Networks,” *Applied Soft Computing*, vol. 62, pp. 915–922, Jan. 2018. [Online]. Available: <https://www.sciencedirect.com/science/article/pii/S1568494617305665>
- [102] W. Gao, L. Zhang, W. Huang, F. Min, J. He, and A. Song, “Deep Neural Networks for Sensor-Based Human Activity Recognition Using Selective Kernel Convolution,” *IEEE Transactions on Instrumentation and Measurement*, vol. 70, pp. 1–13, 2021. [Online]. Available: <https://ieeexplore.ieee.org/document/9507456>
- [103] A. Sarkar, S. K. S. Hossain, and R. Sarkar, “Human activity recognition from sensor data using spatial attention-aided CNN with genetic algorithm,” *Neural Computing and Applications*, vol. 35, no. 7, pp. 5165–5191, Mar. 2023. [Online]. Available: <https://doi.org/10.1007/s00521-022-07911-0>
- [104] S. Mekruksavanich and A. Jitpattanakul, “LSTM Networks Using Smartphone Data for Sensor-Based Human Activity Recognition in Smart Homes,” *Sensors*, vol. 21, no. 5, p. 1636, Jan. 2021. [Online]. Available: <https://www.mdpi.com/1424-8220/21/5/1636>
- [105] B. A. Mohammed Hashim and R. Amutha, “Human activity recognition based on smartphone using fast feature dimensionality reduction technique,” *Journal of Ambient Intelligence and Humanized Computing*, vol. 12, no. 2, pp. 2365–2374, Feb. 2021. [Online]. Available: <https://doi.org/10.1007/s12652-020-02351-x>
- [106] F. Luo, S. Khan, Y. Huang, and K. Wu, “Binarized Neural Network for Edge Intelligence of Sensor-Based Human Activity Recognition,” *IEEE Transactions on Mobile Computing*, vol. 22, no. 3, pp. 1356–1368, Mar. 2023. [Online]. Available: <https://ieeexplore.ieee.org/document/9529002>
- [107] V. Ghate and S. H. C, “Hybrid deep learning approaches for smartphone sensor-based human activity recognition,” *Multimedia Tools and Applications*, vol. 80, no. 28, pp. 35 585–35 604, Nov. 2021. [Online]. Available: <https://doi.org/10.1007/s11042-020-10478-4>
- [108] A. Jain and V. Kanhangad, “Human Activity Classification in Smartphones Using Accelerometer and Gyroscope Sensors,” *IEEE Sensors Journal*, vol. 18, no. 3, pp. 1169–1177, Feb. 2018. [Online]. Available: <https://ieeexplore.ieee.org/document/8186158>
- [109] Q. Teng, K. Wang, L. Zhang, and J. He, “The Layer-Wise Training Convolutional Neural Networks Using Local Loss for Sensor-Based Human Activity Recognition,” *IEEE Sensors Journal*, vol. 20, no. 13, pp. 7265–7274, Jul. 2020. [Online]. Available: <https://ieeexplore.ieee.org/document/9026890>
- [110] W. Huang, L. Zhang, W. Gao, F. Min, and J. He, “Shallow Convolutional Neural Networks for Human Activity Recognition Using Wearable Sensors,” *IEEE*

- Transactions on Instrumentation and Measurement*, vol. 70, pp. 1–11, 2021. [Online]. Available: <https://ieeexplore.ieee.org/document/9464302>
- [111] S. Xu, Q. Tang, L. Jin, and Z. Pan, “A Cascade Ensemble Learning Model for Human Activity Recognition with Smartphones,” *Sensors*, vol. 19, no. 10, p. 2307, Jan. 2019. [Online]. Available: <https://www.mdpi.com/1424-8220/19/10/2307>
- [112] T.-H. Tan, J.-Y. Wu, S.-H. Liu, and M. Gochoo, “Human Activity Recognition Using an Ensemble Learning Algorithm with Smartphone Sensor Data,” *Electronics*, vol. 11, no. 3, p. 322, Jan. 2022. [Online]. Available: <https://www.mdpi.com/2079-9292/11/3/322>
- [113] L. Lu, C. Zhang, K. Cao, T. Deng, and Q. Yang, “A Multichannel CNN-GRU Model for Human Activity Recognition,” *IEEE Access*, vol. 10, pp. 66 797–66 810, 2022. [Online]. Available: <https://ieeexplore.ieee.org/document/9802089>
- [114] S. K. Challa, A. Kumar, and V. B. Semwal, “A multibranch CNN-BiLSTM model for human activity recognition using wearable sensor data,” *The Visual Computer*, vol. 38, no. 12, pp. 4095–4109, Dec. 2022. [Online]. Available: <https://doi.org/10.1007/s00371-021-02283-3>
- [115] N. Dua, S. N. Singh, and V. B. Semwal, “Multi-input CNN-GRU based human activity recognition using wearable sensors,” *Computing*, vol. 103, no. 7, pp. 1461–1478, Jul. 2021. [Online]. Available: <https://doi.org/10.1007/s00607-021-00928-8>
- [116] K. Xia, J. Huang, and H. Wang, “LSTM-CNN Architecture for Human Activity Recognition,” *IEEE Access*, vol. 8, pp. 56 855–56 866, 2020. [Online]. Available: <https://ieeexplore.ieee.org/document/9043535>
- [117] Z. N. Khan and J. Ahmad, “Attention induced multi-head convolutional neural network for human activity recognition,” *Applied Soft Computing*, vol. 110, p. 107671, Oct. 2021. [Online]. Available: <https://www.sciencedirect.com/science/article/pii/S1568494621005925>
- [118] M. Ronald, A. Poulouse, and D. S. Han, “iSPLInception: An Inception-ResNet Deep Learning Architecture for Human Activity Recognition,” *IEEE Access*, vol. 9, pp. 68 985–69 001, 2021. [Online]. Available: <https://ieeexplore.ieee.org/document/9425494/similar#similar>
- [119] Y. Zhao, R. Yang, G. Chevalier, X. Xu, and Z. Zhang, “Deep Residual Bidir-LSTM for Human Activity Recognition Using Wearable Sensors,” *Mathematical Problems in Engineering*, vol. 2018, no. 1, p. 7316954, 2018. [Online]. Available: <https://onlinelibrary.wiley.com/doi/abs/10.1155/2018/7316954>
- [120] E. J. Candes and M. B. Wakin, “An Introduction To Compressive Sampling,” *IEEE Signal Processing Magazine*, vol. 25, no. 2, pp. 21–30, Mar. 2008. [Online]. Available: <https://ieeexplore.ieee.org/document/4472240>
- [121] Y. Arjoun, N. Kaabouch, H. El Ghazi, and A. Tamtaoui, “Compressive sensing: Performance comparison of sparse recovery algorithms,” in *2017 IEEE 7th Annual*

- Computing and Communication Workshop and Conference (CCWC)*, Jan. 2017, pp. 1–7. [Online]. Available: <https://ieeexplore.ieee.org/document/7868430>
- [122] E. J. Candès, “The restricted isometry property and its implications for compressed sensing,” *Comptes Rendus Mathématique*, vol. 346, no. 9, pp. 589–592, May 2008. [Online]. Available: <https://www.sciencedirect.com/science/article/pii/S1631073X08000964>
- [123] A. Kundu and P. K. Roy, “Sparse Signal Recovery from Nonadaptive Linear Measurements,” *arXiv e-prints*, p. 5, Oct. 2013. [Online]. Available: <https://ui.adsabs.harvard.edu/abs/2013arXiv1310.8468K>
- [124] E. Candès and J. Romberg, “Sparsity and incoherence in compressive sampling,” *Inverse Problems*, vol. 23, no. 3, p. 969, Apr. 2007. [Online]. Available: <https://dx.doi.org/10.1088/0266-5611/23/3/008>
- [125] D. E. Bellasi, L. Bettini, C. Benkeser, T. Burger, Q. Huang, and C. Studer, “VLSI Design of a Monolithic Compressive-Sensing Wideband Analog-to-Information Converter,” *IEEE Journal on Emerging and Selected Topics in Circuits and Systems*, vol. 3, no. 4, pp. 552–565, Dec. 2013. [Online]. Available: <https://ieeexplore.ieee.org/document/6637036>
- [126] J. N. Laska, S. Kirolos, M. F. Duarte, T. S. Ragheb, R. G. Baraniuk, and Y. Massoud, “Theory and Implementation of an Analog-to-Information Converter using Random Demodulation,” in *2007 IEEE International Symposium on Circuits and Systems (ISCAS)*, May 2007, pp. 1959–1962. [Online]. Available: <https://ieeexplore.ieee.org/document/4253049>
- [127] J. Yoo, S. Becker, M. Monge, M. Loh, E. Candès, and A. Emami-Neyestanak, “Design and implementation of a fully integrated compressed-sensing signal acquisition system,” in *2012 IEEE International Conference on Acoustics, Speech and Signal Processing (ICASSP)*, Mar. 2012, pp. 5325–5328. [Online]. Available: <https://ieeexplore.ieee.org/document/6289123>
- [128] M. Mishali, Y. C. Eldar, and A. J. Elron, “Xampling: Signal Acquisition and Processing in Union of Subspaces,” *IEEE Transactions on Signal Processing*, vol. 59, no. 10, pp. 4719–4734, Oct. 2011. [Online]. Available: <https://ieeexplore.ieee.org/document/5948420>
- [129] M. A. Lexa, M. E. Davies, and J. S. Thompson, “Reconciling Compressive Sampling Systems for Spectrally Sparse Continuous-Time Signals,” *IEEE Transactions on Signal Processing*, vol. 60, no. 1, pp. 155–171, Jan. 2012. [Online]. Available: <https://ieeexplore.ieee.org/document/6026970>
- [130] S. Qaisar, R. M. Bilal, W. Iqbal, M. Naureen, and S. Lee, “Compressive sensing: From theory to applications, a survey,” *Journal of Communications and Networks*, vol. 15, no. 5, pp. 443–456, Oct. 2013. [Online]. Available: <https://ieeexplore.ieee.org/document/6674179>

- [131] E. Crespo Marques, N. Maciel, L. Naviner, H. Cai, and J. Yang, “A Review of Sparse Recovery Algorithms,” *IEEE Access*, vol. 7, pp. 1300–1322, 2019. [Online]. Available: <https://ieeexplore.ieee.org/document/8577023>
- [132] K. M. H. Badami, S. Lauwereins, W. Meert, and M. Verhelst, “A 90 nm CMOS, 6 μ W Power-Proportional Acoustic Sensing Frontend for Voice Activity Detection,” *IEEE Journal of Solid-State Circuits*, vol. 51, no. 1, pp. 291–302, Jan. 2016. [Online]. Available: <https://ieeexplore.ieee.org/document/7315025>
- [133] A. Raychowdhury, C. Tokunaga, W. Beltman, M. Deisher, J. W. Tschanz, and V. De, “A 2.3 nJ/Frame Voice Activity Detector-Based Audio Front-End for Context-Aware System-On-Chip Applications in 32-nm CMOS,” *IEEE Journal of Solid-State Circuits*, vol. 48, no. 8, pp. 1963–1969, Aug. 2013. [Online]. Available: <https://ieeexplore.ieee.org/document/6519946>
- [134] X. Liu, E. Gönültaş, and C. Studer, “Analog-to-Feature (A2F) Conversion for Audio-Event Classification,” in *2018 26th European Signal Processing Conference (EUSIPCO)*, Sep. 2018, pp. 2275–2279. [Online]. Available: <https://ieeexplore.ieee.org/document/8553060>
- [135] Y. Gargouri, H. Petit, P. Loumeau, B. Cecconi, and P. Desgreys, “Analog-to-information converter design for low-power acquisition of astrophysical signals,” in *2017 15th IEEE International New Circuits and Systems Conference (NEWCAS)*, Jun. 2017, pp. 113–116. [Online]. Available: <https://ieeexplore.ieee.org/document/8010118>
- [136] D. Gangopadhyay, E. G. Allstot, A. M. R. Dixon, K. Natarajan, S. Gupta, and D. J. Allstot, “Compressed Sensing Analog Front-End for Bio-Sensor Applications,” *IEEE Journal of Solid-State Circuits*, vol. 49, no. 2, pp. 426–438, Feb. 2014. [Online]. Available: <https://ieeexplore.ieee.org/document/6722935>
- [137] F. Pareschi, P. Albertini, G. Frattini, M. Mangia, R. Rovatti, and G. Setti, “Hardware-Algorithms Co-Design and Implementation of an Analog-to-Information Converter for Biosignals Based on Compressed Sensing,” *IEEE Transactions on Biomedical Circuits and Systems*, vol. 10, no. 1, pp. 149–162, Feb. 2016. [Online]. Available: <https://ieeexplore.ieee.org/document/7192741>
- [138] M. Verhelst and A. Bahai, “Where Analog Meets Digital: Analog to Information Conversion and Beyond,” *IEEE Solid-State Circuits Magazine*, vol. 7, no. 3, pp. 67–80, 2015. [Online]. Available: <https://ieeexplore.ieee.org/document/7258493>
- [139] A. Graps, “An introduction to wavelets,” *IEEE Computational Science and Engineering*, vol. 2, no. 2, pp. 50–61, 1995. [Online]. Available: <https://ieeexplore.ieee.org/document/388960>
- [140] T. Guo, T. Zhang, E. Lim, M. López-Benítez, F. Ma, and L. Yu, “A Review of Wavelet Analysis and Its Applications: Challenges and Opportunities,” *IEEE Access*, vol. 10, pp. 58 869–58 903, 2022. [Online]. Available: <https://ieeexplore.ieee.org/document/9785993>

- [141] S. Mallat, *Une exploration des signaux en ondelettes*. Editions Ecole Polytechnique, 2000.
- [142] A. Haar, “Zur Theorie der orthogonalen Funktionensysteme,” *Mathematische Annalen*, vol. 69, no. 3, pp. 331–371, Sep. 1910. [Online]. Available: <https://doi.org/10.1007/BF01456326>
- [143] Ü. Lepik, “Haar wavelet method for solving higher order differential equations,” *International Journal of Mathematics and Computation*, vol. 1, pp. 84–94, Jan. 2008.
- [144] D. Gabor, “Theory of communication. Part 1: The analysis of information,” *Journal of the Institution of Electrical Engineers - Part III: Radio and Communication Engineering*, vol. 93, no. 26, pp. 429–441, Nov. 1946. [Online]. Available: <https://digital-library.theiet.org/doi/10.1049/ji-3-2.1946.0074>
- [145] J. Li, K. Cheng, S. Wang, F. Morstatter, R. P. Trevino, J. Tang, and H. Liu, “Feature Selection: A Data Perspective,” *ACM Comput. Surv.*, vol. 50, no. 6, pp. 94:1–94:45, Dec. 2017. [Online]. Available: <https://dl.acm.org/doi/10.1145/3136625>
- [146] J. Tang, S. Alelyani, and H. Liu, “Feature selection for classification: A review,” in *Data Classification*. CRC Press, Jan. 2014, pp. 37–64. [Online]. Available: <http://www.scopus.com/inward/record.url?scp=85054068951&partnerID=8YFLogxK>
- [147] J. R. Quinlan, “Induction of decision trees,” *Machine Learning*, vol. 1, no. 1, pp. 81–106, Mar. 1986. [Online]. Available: <https://doi.org/10.1007/BF00116251>
- [148] F. J. Ferri, P. Pudil, M. Hatef, and J. Kittler, “Comparative study of techniques for large-scale feature selection,” in *Machine Intelligence and Pattern Recognition*, ser. Pattern Recognition in Practice IV, E. S. Gelsema and L. S. Kanal, Eds. North-Holland, Jan. 1994, vol. 16, pp. 403–413. [Online]. Available: <https://www.sciencedirect.com/science/article/pii/B9780444818928500407>
- [149] Y. Hartmann, H. Liu, and T. Schultz, “Feature Space Reduction for Human Activity Recognition based on Multi-channel Biosignals;,” in *Proceedings of the 14th International Joint Conference on Biomedical Engineering Systems and Technologies*. SCITEPRESS - Science and Technology Publications, 2021, pp. 215–222. [Online]. Available: <https://www.scitepress.org/DigitalLibrary/Link.aspx?doi=10.5220/0010260802150222>
- [150] L. Breiman, “Random Forests,” *Machine Learning*, vol. 45, no. 1, pp. 5–32, Oct. 2001. [Online]. Available: <https://doi.org/10.1023/A:1010933404324>
- [151] A. Cutler, D. R. Cutler, and J. R. Stevens, “Random Forests,” in *Ensemble Machine Learning: Methods and Applications*, C. Zhang and Y. Ma, Eds. New York, NY: Springer, 2012, pp. 157–175. [Online]. Available: https://doi.org/10.1007/978-1-4419-9326-7_5
- [152] B. Schölkopf and A. J. Smola, *Learning with Kernels: Support Vector Machines, Regularization, Optimization, and Beyond*. The MIT Press, Dec. 2001. [Online]. Available: <https://direct.mit.edu/books/monograph/1821/Learning-with-KernelsSupport-Vector-Machines>

- [153] F. Rosenblatt, “The perceptron: A probabilistic model for information storage and organization in the brain,” *Psychological Review*, vol. 65, no. 6, pp. 386–408, 1958. [Online]. Available: <https://doi.org/doi/10.1037/h0042519>
- [154] H. Bhamra, J. Lynch, M. Ward, and P. Irazoqui, “A Noise-Power-Area Optimized Biosensing Front End for Wireless Body Sensor Nodes and Medical Implantable Devices,” *IEEE Transactions on Very Large Scale Integration (VLSI) Systems*, vol. 25, no. 10, pp. 2917–2928, Oct. 2017. [Online]. Available: <https://ieeexplore.ieee.org/document/7959650>
- [155] J. Pérez-Bailón, B. Calvo, N. Medrano, and J. Ramírez-Angulo, “A 1.8 V Gm-C Highly Tunable Low Pass Filter for Sensing Applications,” in *2020 IEEE International Instrumentation and Measurement Technology Conference (I2MTC)*, May 2020, pp. 1–5. [Online]. Available: <https://ieeexplore.ieee.org/document/9128692>
- [156] F. Morshedlou, N. Ravanshad, and H. Rezaee-Dehsorkh, “An ultra-low power analog QRS-detection circuit for ambulatory ECG monitoring,” *AEU - International Journal of Electronics and Communications*, vol. 129, p. 153551, Feb. 2021. [Online]. Available: <https://www.sciencedirect.com/science/article/pii/S1434841120327552>
- [157] C. B. Güngör and H. Töreyn, “A 0.5 nW Analog ECG Processor for Real Time R-wave Detection Based on Pan-Tompkins Algorithm,” in *2019 IEEE EMBS International Conference on Biomedical & Health Informatics (BHI)*, May 2019, pp. 1–4. [Online]. Available: <https://ieeexplore.ieee.org/document/8834508>
- [158] C. B. Güngör, P. P. Mercier, and H. Töreyn, “A 1.2nW Analog Electrocardiogram Processor Achieving a 99.63% QRS Complex Detection Sensitivity,” *IEEE Transactions on Biomedical Circuits and Systems*, vol. 15, no. 3, pp. 617–628, Jun. 2021. [Online]. Available: <https://ieeexplore.ieee.org/document/9468409>
- [159] J. Muschelli, “ROC and AUC with a Binary Predictor: A Potentially Misleading Metric,” *Journal of classification*, vol. 37, no. 3, pp. 696–708, Oct. 2020. [Online]. Available: <https://www.ncbi.nlm.nih.gov/pmc/articles/PMC7695228/>
- [160] S. Qiu, H. Zhao, N. Jiang, Z. Wang, L. Liu, Y. An, H. Zhao, X. Miao, R. Liu, and G. Fortino, “Multi-sensor information fusion based on machine learning for real applications in human activity recognition: State-of-the-art and research challenges,” *Information Fusion*, vol. 80, pp. 241–265, Apr. 2022. [Online]. Available: <https://www.sciencedirect.com/science/article/pii/S1566253521002311>
- [161] C. Antonopoulos, S.-M. Dima, and S. Koubias, “Event Identification in Wireless Sensor Networks,” in *Components and Services for IoT Platforms: Paving the Way for IoT Standards*, G. Keramidas, N. Voros, and M. Hübner, Eds. Cham: Springer International Publishing, 2017, pp. 187–210. [Online]. Available: https://doi.org/10.1007/978-3-319-42304-3_10
- [162] O. Krestinskaya, K. N. Salama, and A. P. James, “Learning in Memristive Neural Network Architectures Using Analog Backpropagation Circuits,” *IEEE Transactions*

- on Circuits and Systems I: Regular Papers*, vol. 66, no. 2, pp. 719–732, Feb. 2019. [Online]. Available: <https://ieeexplore.ieee.org/document/8468181>
- [163] M. R. Azghadi, C. Lammie, J. K. Eshraghian, M. Payvand, E. Donati, B. Linares-Barranco, and G. Indiveri, “Hardware Implementation of Deep Network Accelerators Towards Healthcare and Biomedical Applications,” *IEEE Transactions on Biomedical Circuits and Systems*, vol. 14, no. 6, pp. 1138–1159, Dec. 2020. [Online]. Available: <https://ieeexplore.ieee.org/document/9250613>
- [164] O. Krestinskaya, A. P. James, and L. O. Chua, “Neuromemristive Circuits for Edge Computing: A Review,” *IEEE Transactions on Neural Networks and Learning Systems*, vol. 31, no. 1, pp. 4–23, Jan. 2020. [Online]. Available: <https://ieeexplore.ieee.org/document/8667457>
- [165] R. Yan, Q. Hong, C. Wang, J. Sun, and Y. Li, “Multilayer Memristive Neural Network Circuit Based on Online Learning for License Plate Detection,” *IEEE Transactions on Computer-Aided Design of Integrated Circuits and Systems*, vol. 41, no. 9, pp. 3000–3011, Sep. 2022. [Online]. Available: <https://ieeexplore.ieee.org/document/9582811>
- [166] H. Liu, T. Xue, and T. Schultz, “On a Real Real-Time Wearable Human Activity Recognition System:,” in *Proceedings of the 16th International Joint Conference on Biomedical Engineering Systems and Technologies*. Lisbon, Portugal: SCITEPRESS - Science and Technology Publications, 2023, pp. 711–720. [Online]. Available: <https://www.scitepress.org/DigitalLibrary/Link.aspx?doi=10.5220/0011927700003414>
- [167] H. Liu and T. Schultz, “How Long Are Various Types of Daily Activities? Statistical Analysis of a Multimodal Wearable Sensor-based Human Activity Dataset:,” in *Proceedings of the 15th International Joint Conference on Biomedical Engineering Systems and Technologies*. SCITEPRESS - Science and Technology Publications, 2022, pp. 680–688. [Online]. Available: <https://www.scitepress.org/DigitalLibrary/Link.aspx?doi=10.5220/0010896400003123>
- [168] H. Liu, Y. Hartmann, and T. Schultz, “CSL-SHARE: A Multimodal Wearable Sensor-Based Human Activity Dataset,” *Frontiers in Computer Science*, vol. 3, Oct. 2021. [Online]. Available: <https://www.frontiersin.org/journals/computer-science/articles/10.3389/fcomp.2021.759136/full>
- [169] “Accelerometers | Analog Devices.” [Online]. Available: <https://www.analog.com/en/product-category/accelerometers.html>
- [170] Y. Zeng, Z. Li, W. Chen, W. Zhou, Y. Bao, Y. Chen, and Y. Li, “A 672-nW, 670-nVrms ECG Acquisition AFE With Noise-Tolerant Heartbeat Detector,” *IEEE Open Journal of Circuits and Systems*, vol. 4, pp. 25–35, 2023. [Online]. Available: <https://ieeexplore.ieee.org/document/10020171>
- [171] M. Vafaei, A. Parhizgar, E. Abiri, and M. R. Salehi, “A low power and ultra-high input impedance analog front end based on fully differential difference inverter-based amplifier for biomedical applications,” *AEU - International Journal of*

- Electronics and Communications*, vol. 142, p. 154005, Dec. 2021. [Online]. Available: <https://www.sciencedirect.com/science/article/pii/S1434841121004027>
- [172] Y.-P. Hsu, Z. Liu, and M. M. Hella, "A 12.3- μ W 0.72-mm² Fully Integrated Front-End IC for Arterial Pulse Waveform and ExG Recording," *IEEE Journal of Solid-State Circuits*, vol. 55, no. 10, pp. 2756–2770, Oct. 2020. [Online]. Available: <https://ieeexplore.ieee.org/document/9153057>
- [173] T. Zhang, Y. Li, C. Su, X. Zhang, and Y. Yang, "A 1V 3.5 μ W Bio-AFE With Chopper-Capacitor-Chopper Integrator-Based DSL and Low Power GM-C Filter," *IEEE Transactions on Circuits and Systems II: Express Briefs*, vol. 69, no. 1, pp. 5–9, Jan. 2022. [Online]. Available: <https://ieeexplore.ieee.org/document/9446560>
- [174] F. Tang, N. Wu, T. Yang, and H. Wang, "A -110 dB THD rail-to-rail class-AB programmable gain amplifier with common-mode-detection-based transconductance linearization scheme," *Microelectronics Journal*, vol. 128, p. 105511, Oct. 2022. [Online]. Available: <https://www.sciencedirect.com/science/article/pii/S0026269222001422>
- [175] J. Pérez-Bailón, A. Márquez, B. Calvo, and N. Medrano, "A 0.18 μ m CMOS Widely Tunable Low Pass Filter with sub-Hz Cutoff Frequencies," in *2018 IEEE International Symposium on Circuits and Systems (ISCAS)*, May 2018, pp. 1–4. [Online]. Available: <https://ieeexplore.ieee.org/document/8351166>
- [176] E. Rodriguez-Villegas, A. J. Casson, and P. Corbishley, "A Subhertz Nanopower Low-Pass Filter," *IEEE Transactions on Circuits and Systems II: Express Briefs*, vol. 58, no. 6, pp. 351–355, Jun. 2011. [Online]. Available: <https://ieeexplore.ieee.org/document/5930351>
- [177] N. B. Gaikwad, V. Tiwari, A. Keskar, and N. C. Shivaprakash, "Efficient FPGA Implementation of Multilayer Perceptron for Real-Time Human Activity Classification," *IEEE Access*, vol. 7, pp. 26 696–26 706, 2019. [Online]. Available: <https://ieeexplore.ieee.org/document/8651457>
- [178] Q. Hu, X. Tang, and W. Tang, "A Smart Chair Sitting Posture Recognition System Using Flex Sensors and FPGA Implemented Artificial Neural Network," *IEEE Sensors Journal*, vol. 20, no. 14, pp. 8007–8016, Jul. 2020. [Online]. Available: <https://ieeexplore.ieee.org/document/9032200>
- [179] B. James Romaine and M. P. Martín, "High-Throughput Low Power Area Efficient 17-bit 2's Complement Multilayer Perceptron Components and Architecture for on-Chip Machine Learning in Implantable Devices," *IEEE Access*, vol. 10, pp. 92 516–92 531, 2022. [Online]. Available: <https://ieeexplore.ieee.org/document/9870814>
- [180] B. Moons, D. Bankman, L. Yang, B. Murmann, and M. Verhelst, "BinarEye: An always-on energy-accuracy-scalable binary CNN processor with all memory on chip in 28nm CMOS," in *2018 IEEE Custom Integrated Circuits Conference (CICC)*, Apr. 2018, pp. 1–4. [Online]. Available: <https://ieeexplore.ieee.org/document/8357071>

- [181] X. Wang, M. Magno, L. Cavigelli, and L. Benini, “FANN-on-MCU: An Open-Source Toolkit for Energy-Efficient Neural Network Inference at the Edge of the Internet of Things,” *IEEE Internet of Things Journal*, vol. 7, no. 5, pp. 4403–4417, May 2020. [Online]. Available: <https://ieeexplore.ieee.org/document/9016202>
- [182] A. Bahr, M. Schneider, M. A. Francis, H. M. Lehmann, I. Barg, A.-S. Buschhoff, P. Wulff, T. Strunskus, and F. Faupel, “Epileptic Seizure Detection on an Ultra-Low-Power Embedded RISC-V Processor Using a Convolutional Neural Network,” *Biosensors*, vol. 11, no. 7, p. 203, Jul. 2021. [Online]. Available: <https://www.mdpi.com/2079-6374/11/7/203>
- [183] Y. Yin, S. M. Abubakar, S. Tan, H. Jiang, Z. Wang, S.-P. U, and W. Jia, “A 17.7-pJ/Cycle ECG Processor for Arrhythmia Detection with High Immunity to Power Line Interference and Baseline Drift,” in *2020 IEEE Asian Solid-State Circuits Conference (A-SSCC)*, Nov. 2020, pp. 1–4. [Online]. Available: <https://ieeexplore.ieee.org/document/9336104>
- [184] Y. Yin, S. M. Abubakar, S. Tan, J. Shi, P. Yang, W. Yang, H. Jiang, Z. Wang, W. Jia, and S.-P. U, “A 2.63 μ W ECG Processor With Adaptive Arrhythmia Detection and Data Compression for Implantable Cardiac Monitoring Device,” *IEEE Transactions on Biomedical Circuits and Systems*, vol. 15, no. 4, pp. 777–790, Aug. 2021. [Online]. Available: <https://ieeexplore.ieee.org/document/9497713>
- [185] J. Deng, J. Ma, J. Yang, S. Liu, H. Chen, X. Wang, and X. Zhang, “An Energy-Efficient ECG Processor Based on HDWT and a Hybrid Classifier for Arrhythmia Detection,” *Applied Sciences*, vol. 14, no. 1, p. 342, Jan. 2024. [Online]. Available: <https://www.mdpi.com/2076-3417/14/1/342>
- [186] K. Basterretxea, J. Echanobe, and I. del Campo, “A wearable human activity recognition system on a chip,” in *Proceedings of the 2014 Conference on Design and Architectures for Signal and Image Processing*, Oct. 2014, pp. 1–8. [Online]. Available: <https://ieeexplore.ieee.org/document/7115600>
- [187] G. Bhat, R. Deb, V. V. Chaurasia, H. Shill, and U. Y. Ogras, “Online Human Activity Recognition using Low-Power Wearable Devices,” in *2018 IEEE/ACM International Conference on Computer-Aided Design (ICCAD)*, Nov. 2018, pp. 1–8. [Online]. Available: <https://ieeexplore.ieee.org/document/8587748>
- [188] G. Bhat, Y. Tuncel, S. An, H. G. Lee, and U. Y. Ogras, “An Ultra-Low Energy Human Activity Recognition Accelerator for Wearable Health Applications,” *ACM Trans. Embed. Comput. Syst.*, vol. 18, no. 5s, pp. 49:1–49:22, Oct. 2019. [Online]. Available: <https://dl.acm.org/doi/10.1145/3358175>

Titre : Vers des capteurs intelligents sans fil flexibles et à faible consommation : convertisseur analogique-paramètre reconfigurable pour les applications dans le domaine de la santé

Mots clés : Convertisseur analogique-paramètre, Réseaux corporels sans fil, Capteurs intelligents, Échantillonnage non-uniforme en ondelettes, Détection d'arythmie, Reconnaissance des activités humaines.

Résumé :

La croissance démographique et le vieillissement actuels augmentent le taux de maladies chroniques, principale cause mondiale de décès. Les réseaux corporels sans fil (WBANs), composés de capteurs intelligents portables ou implantables, sont la principale solution pour les systèmes de soins de santé proactifs réduisant le fardeau de ces maladies. Or, ces réseaux sont limités en termes de consommation d'énergie et de débit de données, surtout dans le cas des capteurs biopotentiels et inertiels avec une acquisition continue des signaux. La réduction de la quantité de données collectées et envoyées, améliorant l'autonomie des capteurs, est possible dans les applications de classification. Ainsi, cette thèse vise à concevoir un convertisseur analogique-paramètre (A2F) reconfigurable qui extrait uniquement les paramètres pertinents pour une tâche donnée dans le domaine analogique au sein du capteur et qui classe ensuite au niveau du capteur ou de l'agrégateur.

Basé sur l'échantillonnage non-uniforme en ondelettes (NUWS), le convertisseur s'appuie sur une architecture générique pour s'adapter à différents signaux basse fréquence et permettre des WBANs avec des capteurs multimodaux. Pour prouver l'universalité du convertisseur, nous abordons la détection d'anomalies dans les signaux d'électrocardiogramme (ECG) et la reconnaissance des activités humaines (HAR) dans les signaux inertiels. Après l'entraînement des classificateurs de réseaux neuronaux pour chaque application, nous avons défini les paramètres pertinents et les spécifications matérielles requises pour la conception complète du circuit. Grâce à la simulation circuit du convertisseur, nous pouvons montrer que la consommation énergétique estimée est divisée par 20 pour l'ECG et 5 pour HAR par rapport à l'approche de Nyquist. Cela souligne le potentiel de la conversion A2F avec NUWS dans la réalisation de systèmes de capteurs flexibles, fiables et à faible consommation pour les soins de santé et au-delà.

Title : Towards flexible and low-power wireless smart sensors: reconfigurable analog-to-feature converter for healthcare applications

Keywords : Analog-to-Feature converter, Wireless Body Area Networks, Smart sensors, Non-Uniform Wavelet Sampling, Arrhythmia detection, Human activity recognition.

Abstract :

Current human population growth and aging inevitably raise the rate of chronic diseases, the leading global cause of death. Wireless Body Area Networks (WBANs) composed of smart wearable or implantable sensors are the primary solution for proactive healthcare systems to reduce the burden of these diseases. However, such networks are severely restricted regarding energy usage and data throughput, especially in the case of biopotential and inertial sensors requiring continuous signal acquisition. Reducing the amount of collected and sent data, thus improving sensors' autonomy, is possible in classification applications. For this purpose, this thesis aims to design a reconfigurable Analog-to-Feature (A2F) converter that extracts only relevant features for a given task in the analog domain within the sensor node and classifies further at the sensor or ag-

gregator level. Based on Non-Uniform Wavelet Sampling (NUWS), our converter leverages a generic architecture to suit different low-frequency signals and enable WBANs with multimodal sensors. To prove the converter's universality, we address two applications : anomaly detection in electrocardiogram (ECG) signals and human activity recognition (HAR) in inertial signals. After training the neural network classifiers for each application, we defined the relevant features and hardware specifications required for the complete circuit design. Thanks to the circuit level simulation of the converter, we can show that the estimated energy consumption is divided by 20 for ECG and 5 for HAR compared to the Nyquist approach. This fact highlights the potential of A2F conversion with NUWS in achieving flexible, reliable, and low-power sensor systems for healthcare and beyond.